DEVELOPMENT OF NEW PYROCHLORE-TYPE ELECTROCATALYSTS FOR OXYGEN EVOLUTION REACTION IN ACID

BY

PEI-CHIEH SHIH

DISSERTATION

Submitted in partial fulfillment of the requirements
for the degree of Doctor of Philosophy in Chemical Engineering
in the Graduate College of the
University of Illinois at Urbana-Champaign, 2019

Urbana, Illinois

Doctoral Committee:

Professor Hong Yang, Chair
Professor Ying Diao
Professor David W. Flaherty
Professor Paul V. Braun

ABSTRACT

A major challenge for the commercialization of water electrolyzer using proton exchange membrane (PEM) is the development of acid-stable, active catalysts for the oxygen evolution reaction (OER). In addition to discovering new catalysts, a fundamental understanding of OER activity and stability origin is also critical.

This dissertation focuses on: (1) identifying active and acid-stable OER catalysts in comparison to the state-of-the-art RuO_2 and IrO_2 catalysts; (2) studying the intrinsic material properties that yield high OER activity and stability; and (3) developing synthetic techniques to enhance the OER activity of a catalyst. The first part of the thesis concentrates on new material synthesis and methods to analyze activity and stability. Next, both theoretical calculations and experimental analysis are used to study the material properties. The last part discusses approaches that lead to high surface area and enhanced catalytic performance.

Specifically, pyrochlore-type ruthenium (Ru) and iridium (Ir) based catalysts were synthesized and characterized for their OER performance. Introducing yttrium (Y) in these pyrochlores increased the overall activity and stability. To explain this behavior, X-ray absorption spectroscopy (XAS) and density functional theory (DFT) calculations were used to study the electronic and structural properties of these materials. Additionally, a range of iridium-based pyrochlores with lanthanide (La) series metals were studied to identify the important effects of the A-site metal atoms on the OER catalytic properties.

To synthesize high surface area, porous yttrium ruthenate pyrochlores, two techniques were utilized: polymeric entrapment synthesis and acid porogen strategy. The polymeric entrapment reduced the synthesis temperature, whereas the addition of perchloric acid generated pores during

our established sol-gel synthesis. These materials showed enhanced OER activity, attributed to higher surface area.

The results in this dissertation provide new insights towards the design and development of active and stable OER catalysts.

ACKNOWLEDGEMENTS

First, I would like to thank my research advisor, Prof. Hong Yang, for his wholehearted support and guidance during my Ph.D. study. Prof. Yang was very patient in guiding me through in these years and always gave me opportunities to learn new things and be more capable. Not only in academic aspect, Prof. Yang gave me support and warmth with his considerate attention on my physical and mental well-being and ensuring me to be successful in the future career.

I would like to thank Prof. Paul Braun, Prof. David Flaherty and Prof. Ying Diao for accepting to be part of my thesis committee and gave me feedbacks. Their advice and support have helped me go through my Ph.D. study.

I would like to thank Dr. Jaemin Kim for guidance and suggestions throughout my Ph.D. study. I also want to thank him for his contribution to Chapter 2 of this dissertation. Dr. Kim worked as a post-doctoral fellow when I first joined the group and he taught me everything generously, including lab skills, research knowledge, and the way to think of doing research. He acted like a mentor in my early years of Ph.D. study. I wouldn't be as successful without his guidance.

I would like to thank all Yang group members, including Prof. Yung-Tin Pan, Dr. Kai-Chieh Tsao, Dr. Thao Ngo, Steven Warren, Cheng Zhang, Drew Kuhn, Talha Al-Zoubi and many others, for support and friendship for all these years.

I would like to thank Shell Oil Company for the support and Dr. Ryan Stephens, Prof. Jian-Min Zuo and Prof. Qian Chen for many advice and guidance. Although the research results from the project sponsored by Shell were not presented in this thesis, it was a great opportunity and I learned many things while doing that project. I would like to thank co-workers in Prof. Zuo group,

Prof. Chen group and Prof. Braun group for discussion and help on the experiment. I would like to thank Dr. Chengjun Sun and folks in Advance Photon Source of Argonne National Laboratory. A big portion of my thesis analysis had been helped and supported by them.

Lastly, I want to thank my family and friends for their support, and a heartfelt gratitude especially to my parents. Without their support, I wouldn't have made it this far during my graduate study.

TABLE OF CONTENTS

CHAPTER 1

INTRODUCTION

1.1 Motivation

1.1.1 Challenges in hydrogen production from water splitting

The development of sustainable energy sources is a major challenge for the 21st century due to the linkage of increasing environmental concerns and carbon dioxide (CO_2) emissions from fossil fuels usage. Although many researchers strive to neutralize the relative atmospheric CO_2 concentration, carbon-neutral energy techniques are imminent to secure a sustainable future.[1] Among current renewable sources, solar energy is attractive due to its availability. Yet considering the intermittency of daylight, efficient energy storage is critical for widespread usage.[2] In water splitting, the solar energy is transformed into chemical energy in the form of molecular hydrogen (H_2), which can be subsequently stored and used in devices such as hydrogen fuel cells.[3-5] Electrochemically, water molecules break down via the oxygen evolution reaction (OER) and hydrogen evolution reaction (HER), generating molecular oxygen (O_2) and H_2. The transformation cycle does not require carbon, which makes it environmentally-friendly. The greatest challenge is the intrinsically-slow, multi-electron OER at the anode, requiring large overpotential to drive the reaction. Extensive research efforts have been spent in developing new electrocatalyst materials to facilitate the OER.

1.1.2 OER mechanism

Figure 1.1 illustrates the water splitting in alkaline and proton exchange membrane (PEM) based (acidic) electrolysis cells.[6] OER is the anode reaction in both cases with an overall formula of $4OH^- \rightarrow O_2 + 2H_2O + 4e^-$ in alkaline and $2H_2O \rightarrow O_2 + 4H^+ + 4e^-$ in acidic electrolytes, respectively. Kinetically, OER requires multiple elementary steps on the metal catalytic surfaces. Oxy-species adsorb, react, and desorb while generating electrical current. In acid, a four-electron transfer (4 e^-) pathway is generally considered[7-10]:

$$H_2O + * \rightarrow HO^* + H^+ + e^- \quad (1.1)$$

$$HO^* \rightarrow O^* + H^+ + e^- \quad (1.2)$$

$$O^* + H_2O \rightarrow HOO^* + H^+ + e^- \quad (1.3)$$

$$HOO^* \rightarrow * + O_2 + H^* + e^- \quad (1.4)$$

where * represents the active sites of the catalyst. In this mechanism, the reaction begins with a water molecule absorbs on catalyst surface and dissociates into HO^* intermediate species and a proton (eq. 1.1). Follow by the HO^* species further dissociates into O^* and release another proton (eq. 1.2). O^* then reacts with a second water molecule and forms HOO^* intermediate species (eq. 1.3). At last step, HOO^* dissociates into oxygen and leaves the catalyst surface (eq. 1.4). In base, the reaction paths are slightly different[10-13]:

$$M^{m+}OH^- + OH^- \rightarrow M^{(m+1)+}O^{2-} + H_2O + e^- \quad (1.5)$$

$$M^{(m+1)+}O^{2-} + OH^- \rightarrow M^{m+}OOH^- + e^- \quad (1.6)$$

$$M^{m+}OOH^- + OH^- \rightarrow M^{(m+1)+}OO^{2-} + H_2O + e^- \quad (1.7)$$

$$M^{(m+1)+}OO^{2-} + OH^- \rightarrow M^{m+}OH^- + O_2 + e^- \quad (1.8)$$

where *M* represents the metal catalytic sites and *m* represents the equilibrium oxidation state of the metal. Considering that the metal ion surface can absorb OH^- species in alkaline solution, the reaction begins with an OH^- ion approaches to the surface and forms O^{2-} at surface and a water molecule (eq. 1.5). The surface intermediate reacts with another OH^- and forms OOH^- intermediate (eq. 1.6). The OOH^- intermediate reacts with OH^- and forms OO^{2-} intermediate (eq. 1.7). OO^{2-} intermediate reacts with OH^- to forms oxygen and releases from the catalyst surface at the final step (eq. 1.8).

In both acid and base, despite some debates of research, OOH-related surface species reactions (eq. 1.3 in acid and eq. 1.6, 1.7 in base) are more acceptably considered as the rate determine steps (RDS). Additionally, the binding strength between the metal active center and oxy-species (such as O* and OOH*) affects the OER catalytic activity. Based on density functional theory (DFT) calculations, Rossmeisl and Nørskov *et al.* had shown that on rutile RuO_2 and other oxide surfaces, the conversion from O^* to OOH^* had the largest Gibb's free energy barrier in acid.[7,14] They observed a linear relation between adsorption energy of O* (ΔE_{O*}) and OER activity.[7,8] Experimentally, Shao-Horn Yang *et al.* concluded that a specific coordination of the metal 3d electrons was critical for high OER catalytic activity, which was explained by binding strength of metal catalytic center and oxygen.

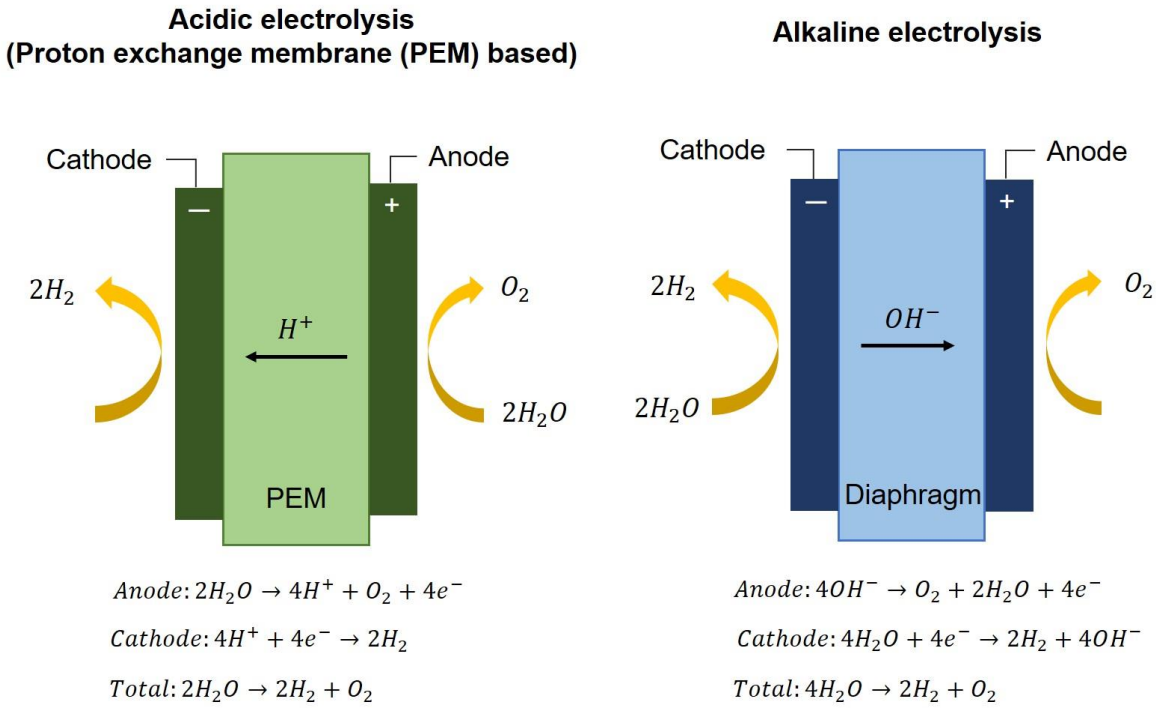

Figure 1.1 The operational principle of alkaline and PEM based water electrolysis cells.

1.1.3 OER performance characterization methods

A half-cell testing protocol is often used to decouple the performance of the cathode and anode, allowing the examination of the intrinsic OER activity. This system requires a 3-electrode setup: a working, counter, and reference electrode. The catalyst is connected at the working electrode where the anodic potential/current is applied. The counter electrode uses an inert material to minimize disturbances during data collection, e.g. platinum (Pt) electrode. The reference electrode is used to give a precise potential reading of the working electrode. Reference electrodes vary by the system: acid solutions use reference hydrogen electrode (RHE); alkaline solutions use mercury reference electrode (Hg/HgO); and, at certain pH values, silver/silver chloride (Ag/AgCl)

electrodes or saturated calomel electrode (SCE) are used. Stability, cost, and storage are other key factors in this selection.

Typical characterization techniques for evaluation of OER catalysts include cyclic voltammogram (CV), linear sweep voltammetry (LSV), chronopotentiometry (galvanostatic measurement), chronoamperometry and electrochemical impedance spectroscopy (EIS). In CV, the applied potential is scanned from 1.1 V (non-Faradaic region) to more than 1.6 V (large OER turnover). An example of a typical CV curve is shown in **Figure 1.2a**. Two curves are shown in the figure, representing the forward and backward scan of CV. Of interest is the onset potential (blue) and the overpotential (η, red). The onset potential represents the energy needed to overcome the reaction barrier for OER, thus reflects the intrinsic kinetics for the catalyst. To compare catalysts, researchers often look at the overpotentials at a given current density. The overpotential equals the potential applied minus the reaction's thermodynamic potential (1.23 V for OER in acid). Smaller overpotentials mean less energy is required for running OER at the given current density.

A Tafel plot graphs the potential versus the current density (logarithmic) as obtained from the polarization curve from CV or LSV (**Figure 1.2b**). The intrinsic OER kinetics of a catalyst follows this equation:

$$\eta = A \times \ln \frac{i}{i_0} \qquad (1.9)$$

where A is called the Tafel slope (mV dec^{-1}), i is current density (A cm^{-2}) and i_0 is the exchange current density (A cm^{-2}). Tafel slope can be express as:

$$A = \frac{kT}{e\alpha} \qquad (1.10)$$

where k is the Boltzmann's constant, T is the absolute temperature, e is the charge and α is the charge transfer coefficient. Here, the charge transfer coefficient describes the kinetic of an electrochemical reaction. Thus, the Tafel slope is often used as a description of OER kinetic.

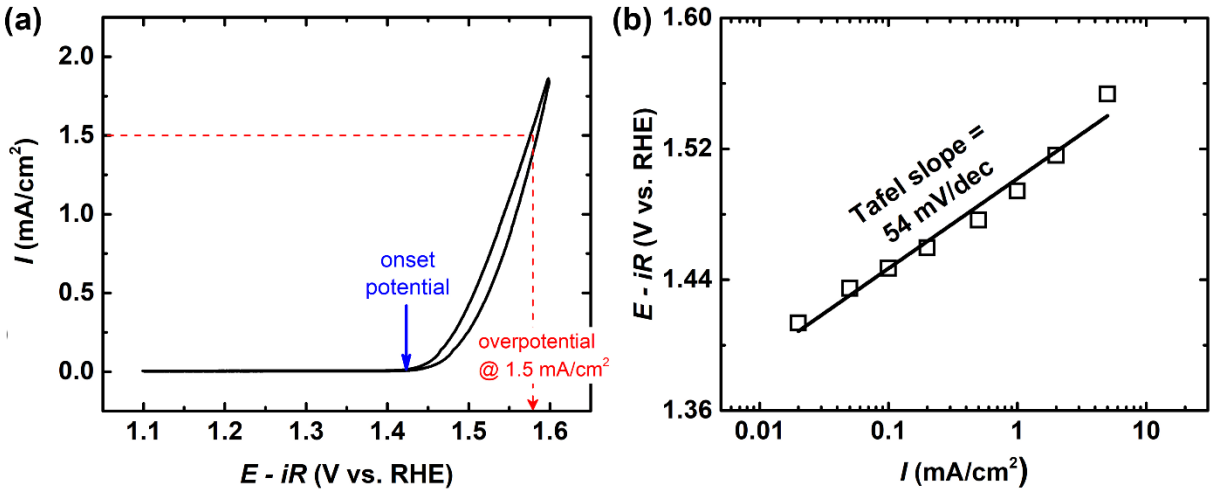

Figure 1.2 Typical graphs of OER measurement (example curves of $Y_2Ru_2O_{7-\delta}$). (a) CV curve illustration, showing onset potential position (blue) and overpotential at 1.5 mA cm^{-2} (red). (b) Tafel plot generated from polarization data from (a). Tafel slope is calculated from a linear fitting of the data.

1.1.4 Why ternary or other complex metal oxides

Ternary structured oxides (TSOs) have great potentials as active OER catalysts, owing to their flexibility in composition with tunable electronic properties and structural geometries. Since the early reports of the perovskite compounds utilized as OER catalyst,[15,16] tremendous amounts of perovskites and other TSO types have been studied and published in literature. Perovskite-type of transition metal oxides with Co, Ni, Fe, Mn as active centers are very successful in alkaline

media, some out-performing noble metal-based catalysts.[9,11,17] Pyrochlore-, spinel-, olivine-type TSOs are also studied towards OER and applications in metal-air batteries, yet the potential of these structures in water electrolysis is underrated or not studied fully.

1.2 Ternary structure metal oxides

1.2.1 Ternary structures (perovskite, pyrochlore, spinel, olivine)

The perovskite structure has a general formula of ABX_3 and can be construct by organic compounds, metal cations, halides and oxygen. In most inorganic perovskite-type compound, the A-site is an alkaline earth or rare-earth metal cation, the B-site is a transition metal cation, and X is oxygen. Because of the varying ionic radii and valence properties of the A and B metals, different phase symmetries are found in perovskite-type oxides. **Figure 1.3** shows the unit cell structures of (a) cubic (*Pm-3m*) $BaTiO_3$, (b) rhombohedral (*R-3cR*) $LaCoO_3$ and (c) orthorhombic (*Pnma*) $CaMnO_3$, respectively. In addition, the electrical and thermal conductivities, magnetic properties, charge ordering, and orbital spin states can vary amongst perovskite-type oxides.[18] Thus, these structures are intriguing and exploitable in catalysis.

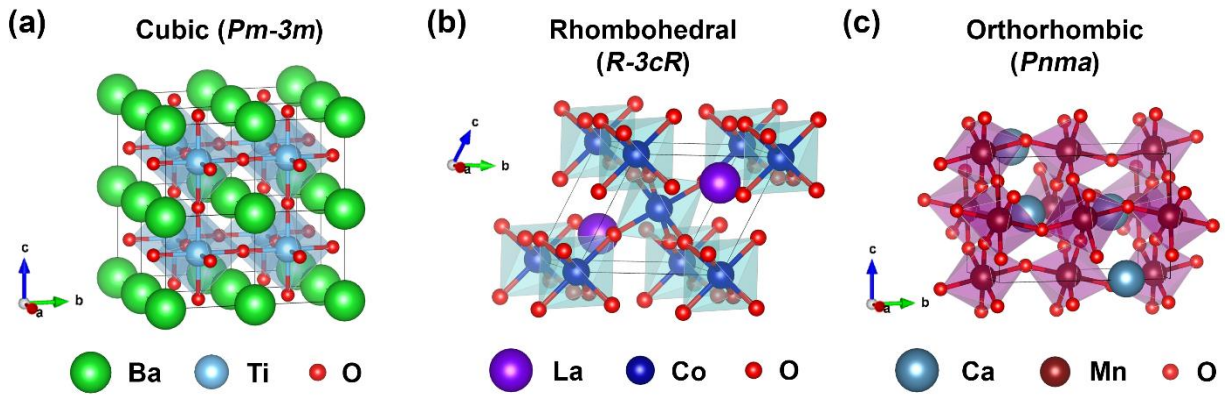

Figure 1.3 Perovskite structures with different elements and symmetries. (a) $BaTiO_3$ (cubic, *Pm-3m*). (b) $LaCoO_3$ (rhombohedral, *R-3cR*). (c) $CaMnO_3$ (orthorhombic, *Pnma*).

Pyrochlore structures have a general formula of $A_2B_2O_7$ or $A_2B_2O_6O'$. Like the perovskite-type, A- and B-sites are occupied by metal cations. However, two types of oxygen connection exist: one anion (O) links building blocks to form networks between A- and B-site cations; and the other anion (O') connects two A-site metal cations (A-O'-A). This design leads to an interpenetrating network of B_2O_6 and A_2O' sublattices as shown in **Figure 1.4a**.[18,19] The B-site metal cations occupy the octahedral site, coordinated by six oxygen atoms and forming a corner-shared BO_6 unit network (**Figure 1.4b**). A-site metal cations and O' anions fill the interstitial sites. Although cubic (*Fd-3m*) phase is the only observed symmetry of pyrochlore structures, they are more flexible than perovskites. Replacement or defects in A-, B- or O' sites are commonly observed in the structures, which lead to a wide-ranging electrical and magnetic properties. For example, lead cations (Pb^{2+}) of pyrochlore $Pb_2Ir_2O_{7-\delta}$ force a δ~0.9 with O' vacant sites.[20] In a related structure, in a pyrochlore $Pb_2Ir_{2-x}Pb_xO_{7-\delta}$, the Pb^{4+} cations can migrate and incorporate into the B-site, which leads to an iridium deficiency.[20] Research has shown that these oxygen defects or deficiency of the pyrochlore structures contribute to high activity for OER.

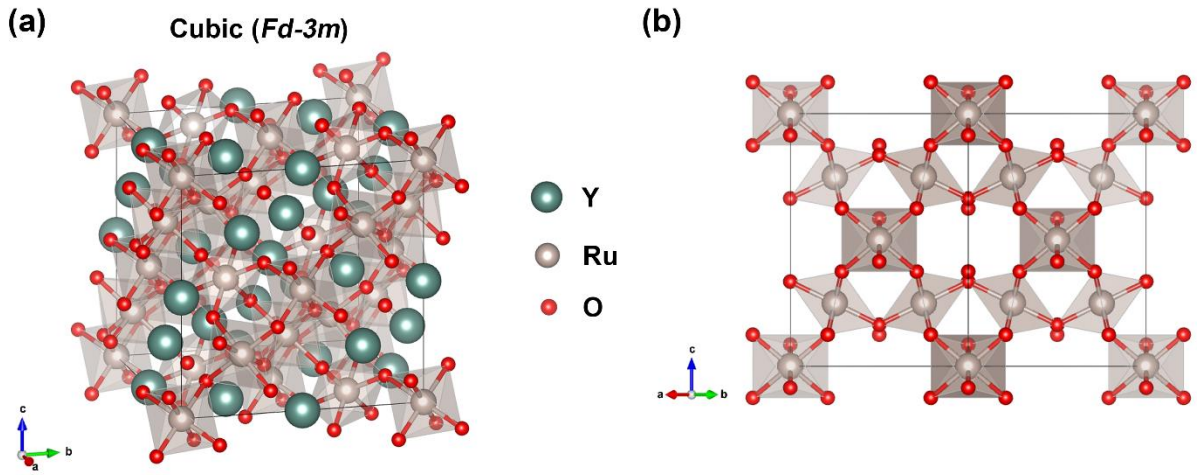

Figure 1.4 Pyrochlore structure view from different planes. (a) $Y_2Ru_2O_7$ unit cell (cubic, *Fd-3m*). (b) Corner-shared BO_6 octahedrons.

Spinel-type oxides have a general formula of AB_2O_4 in which the A and B metal cations occupy different coordinated positions in a cubic (*Fd-3m*) unit cell. A-sites coordinate with four oxygen atoms in a tetrahedron, whereas B-sites coordinate with six oxygen atoms in an octahedron (**Figure 1.5a**). In most cases, A and B are different metal cations, e.g. $NiCo_2O_4$ and $CoMn_2O_4$, but spinel structures can exist with the same element, e.g. Co_3O_4.[21-23] Because of the coexistence of tetrahedral and octahedral sites, metal cations with various valence states and ionic radii can accommodate into the flexible spinel-type structure and make it possible to apply in different areas, such as electrocatalysts and electrode materials of batteries.[21]

Olivine-type structures have non-metals in the B-site, such as phosphorous (P) or silicon (Si). The crystal structure is an orthorhombic (*Pbnm*) with the non-metal coordinating with four oxygen atoms in the tetrahedral site and a metal cation occupying the octahedral sites (**Figure 1.5b**), e.g. Li(Ni, Fe)PO_4 and Mn_2SiO_4.[24,25]

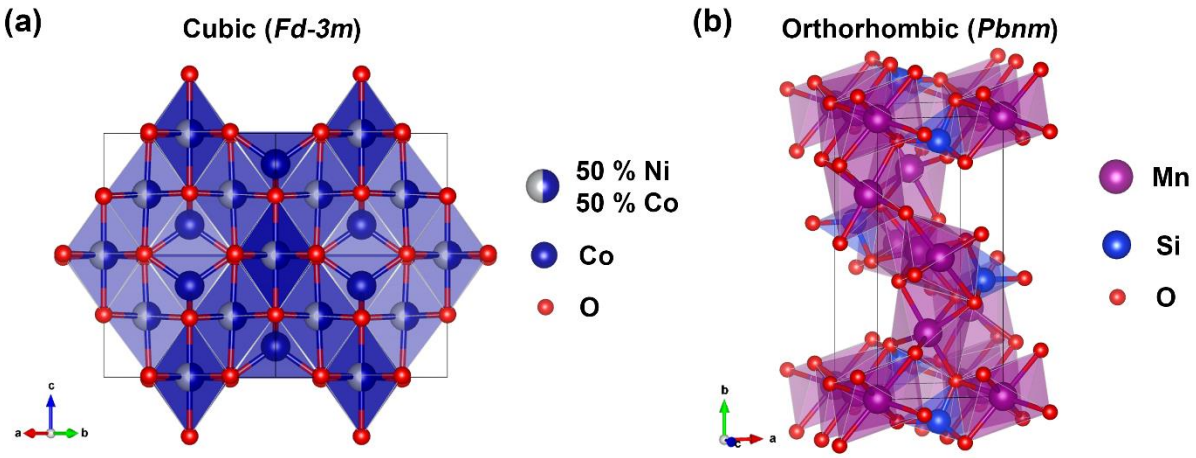

Figure 1.5 Spinel and olivine unit cell structure. (a) $NiCo_2O_4$ unit cell (cubic, *Fd-3m*). (b) Mn_2SiO_4 unit cell (orthorhombic, *Pbnm*).

1.2.2 Oxygen deficient structure

Many perovskites and pyrochlore structures are known to have their oxygen deficient structures exist, the chemical formula become $ABO_{3-\delta}$ and $A_2B_2O_{7-\delta}$. In an oxygen deficient perovskite $CaMnO_{2.5}$, one of the oxygen atoms is completely vacant along the directions normal to *ab* plane (**Figure 1.6a**). Thus, the original MnO_6 unit (octahedron) becomes MnO_5 (square pyramid). This structural change affects the electronic and catalytic properties of the material compare to the original $CaMnO_3$ perovskite. In our previous study, the oxygen vacancies in the $CaMnO_{2.5}$ structure lead to (1) increased structural distortion because of the Jahn-Teller effect; (2) more favorable Mn^{3+} ($t_{2g}^3\ e_g^1$) configuration; and (3) oxygen defect sites, which gives a molecular level porosity. These factors contributed to a favorable OH^- binding and high OER activity.[26] Mefford *et al.* also demonstrated the importance of oxygen vacancy defects on metal oxide surfaces to OER catalytic activity.[27] In their study, different substitution level of strontium cations

(Sr^{2+}) into a $La_{1-x}Sr_xCoO_{3-\delta}$ structure could mitigate the covalency of the Co-O bond and create oxygen defects. Through a proposed vacancy-mediated OER mechanism, where the Fermi energy and the partial density of states (PDOS) of transition metal 3d and oxygen 2p play important roles, they suggested that the oxygen vacancy defects should be a critical factor in OER catalyst design.

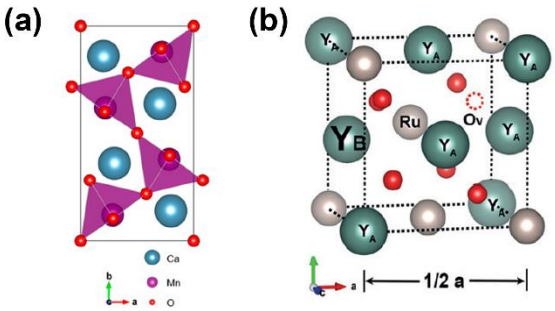

Figure 1.6 Crystal structure of an oxygen-deficient perovskite and B-site substituted pyrochlore. (a) Unit cell structure of $CaMnO_{2.5}$ (orthorhombic, *Pbam*). (b) 1/8 of the unit cell of $Y_2[Ru_{1.6}Y_{0.4}]O_{7-\delta}$ pyrochlore, showing B-site substitution of Ru with Y and oxygen vacant sites.

1.2.3 Mixed metal cation sites

Mixing of the A- and B-site metal cations are known for perovskite, pyrochlore and spinel structures, contributing to intriguing catalytic properties. In a pyrochlore structure, the A metal can migrate to occupy the B-site, leaving a $A_2[B_{2-x}A_x]O_{7-\delta}$ structure. This phenomenon causes a distortion of the unit cell and alters the electronic and catalytic properties of the material. In our recent study, $Y_2[Ru_{1.6}Y_{0.4}]O_{7-\delta}$ structure possess partial replacement of Ru^{4+} with Y^{3+}. This partial replacement contributes to a mixed valence of $Ru^{4+/5+}$, oxygen vacancies and a lattice expansion because of the low valence state of Y^{3+} and large ionic radius. The oxygen defects are located at the bridge site of Y-□-Y, which is a result from charge balancing of the Ru^{4+}/Y^{3+} substitution

(**Figure 1.6b**).[28] $Y_2[Ru_{1.6}Y_{0.4}]O_{7-\delta}$ pyrochlore has shown outstanding activity as OER catalyst and it is suggested that high OER activity is related to the mixing of B-sites.

1.3 Recent development

1.3.1 OER catalysts in base

A large amount of effort has been placed on development of active and stable OER catalysts. Perovskite and spinel structures based on earth-abundant transition-metal oxides (Mn, Fe, Co, Ni) had been studied for possible highly active OER catalysts, which are cost-effective alternatives for traditional noble-metal based catalysts (e.g. IrO_2). $NiCo_2O_4$,[23,29-31] Co_3O_4,[32,33] $CoMn_2O_4$,[22] $LaNiO_3$,[15,34] $LaMnO_3$,[34-36] $LaCoO_3$,[11] and their families (e.g. substitution or doping of the A- and B-site elements) had been reported extensively.[12,13,17,24,26,27,35,37-58] Researchers tried to explore the most active composition in alkaline media. **Table 1.1** shows a comparison of OER activities for those catalysts. Pyrochlore-type compounds based on Ir and Ru are explored for alkaline OER, such as $Pb_2Ir_2O_{7-y}$ and $Pb_2Ru_2O_{6.5}$,[20,59] but are outshined by non-noble metal catalysts and underrated because of their possible application in acidic OER.

Co-based perovskite structures are studied most widely because of its outstanding OER activity. Suntivich *et al.* had reported the $La_{1-x}Ca_xCoO_3$ and $Ba_{0.5}Sr_{0.5}Co_{0.8}Fe_{0.2}O_{3-\delta}$ (BSCF) in 0.1 M KOH solution.[11] Both materials showed good OER catalytic activities. In addition, BSCF showed an exceptional intrinsic OER activity (judging by OER specific activity mA cm^{-2}_{ox}) that surpassed IrO_2 nanoparticles (NPs) for an order of magnitude. The high OER activity of BSCF was suggested to result from a desirable Co oxidation state of ~2.8 and *d*-orbital configuration. The mass activity was improved by ball-milling to sub-micrometer size. It was recommended that nanostructures of BSCF may lead to improvements.

Table 1.1 Summary of ternary metal oxide OER catalysts in base. * data are normalized to oxide surface area. (NF = nickel foam; oLCFO = peroxidation $LaCo_{0.8}Fe_{0.2}O_3$)

Material	Electrolyte	Catalyst loading (mg cm^{-2})	η @ 10 mA cm^{-2} (mV)	j @ η = 0.4 V (mA cm^{-2})	Ref.
RuO_2 NP	0.1 M KOH	0.05	> 470	3.5	[69]
IrO_2 NP	0.1 M KOH	0.05	> 470	4.5	[69]
$LaNiO_3$	0.1 M KOH	0.25	-	~3.5	[11]
$La_{1-x}Ca_xCoO_3$	0.1 M KOH	0.25	-	~0.5-3	[11]
$La_{1-x}CaFeO_3$	0.1 M KOH	0.25	-	~0.2-4	[11]
$La_{1-x}Ca_xMnO_3$	0.1 M KOH	0.25	-	~0.03-0.4	[11]
BSCF	0.1 M KOH	0.25	-	~100	[11]
$CaMnO_3$	0.1 M KOH	0.05	-	~0.2	[26]
$CaMnO_{2.5}$	0.1 M KOH	0.05	-	~1	[26]
$La_{1-x}Sr_xCoO_{3-\delta}$	0.1 M KOH	0.0153	~355*	28*	[27]
NF/oLCFO	0.1 M KOH	1.10	350	~40	[52]
$NiFeO_x$	1 M KOH	~1.6	280	-	[51]
IrO_x	1 M NaOH	N/A	~325	-	[58]

Table 1.1 (Con't)

$NiFeO_x$	1 M NaOH	N/A	~355	-	[58]
$CoFeO_x$	1 M NaOH	N/A	~368	-	[58]
$NiCoO_x$	1 M NaOH	N/A	~375	-	[58]
$NiLaO_x$	1 M NaOH	N/A	~410	-	[58]
$NiCuO_x$	1 M NaOH	N/A	~415	-	[58]
$NiCeO_x$	1 M NaOH	N/A	~425	-	[58]
$NiCo_2O_4$	1 M NaOH	N/A	~320	~100	[23]
Co_3O_4	1 M KOH	N/A	~370	~20	[32]

1.3.2 OER catalysts in acid

Development of OER catalysts in acidic media is particularly challenging due to the intrinsic instability of metal and metal oxide catalysts in acid under high oxidative potentials. For the past decades, RuO_2 and IrO_2 are considered the only practical OER catalysts that possess reasonable activity and durability in acidic solutions. Recently, many pyrochlore-type, complex perovskite-type and multi-phases perovskite-based catalysts have been discovered and shown tremendous improvement of OER activity while maintaining reasonable durability. $Pb_2[Ir_{2-x}Pb_x]O_{7-y}$,[20] $Bi_2Ir_2O_7$,[60,61] $Pb_2Ir_2O_{6.5}$,[61] $(Na_{0.33}Ce_{0.67})_2(Ir_{1-x}Ru_x)_2O_7$,[62] Ba_2MIrO_6,[63] La_2LiIrO_6,[64] $Y_2Ru_2O_{7-y}$,[19] $Y_2Ir_2O_7$,[65] $Y_2[Ru_{1.6}Y_{0.4}]O_{7-\delta}$,[28] $IrO_x/SrIrO_3$,[66] $IrO_x/Y_2Ir_2O_7$,[67] and 6H-$SrIrO_3$,[68] all show superior or comparable OER activity in acid. Their activities and testing conditions are summarized in **Table 1.2** with RuO_2 and IrO_2 as comparison. The overpotential (η) required for achieving 10 mA cm^{-2}_{geo} current density is usually considered as a benchmark to compare between different materials.[69]

Ir-based double perovskite structures are developed and shown improved OER activity than IrO_2. Diaz-Morales *et al.* reported the Ba_2MIrO_6 double perovskite (DP) structures, where M = Y, La, Ce, Pr, Nd, Tb.[63] Ba_2MIrO_6 DP showed more than threefold current densities towards OER compared to benchmarking IrO_2 NPs while reduced the Ir content by 32 wt%. The Ba_2PrIrO_6 and Ba_2YIrO_6 DPs also showed comparable stability to IrO_2 for 1 h at 10 mA cm^{-2} current density. The increased OER activity of Ir DPs catalysts were suggested to attribute to mitigation of oxygen binding strength on the DPs catalysts. The corner-shared octahedra network and introduction of lattice strain could weaken the oxygen adsorption energy on the catalysts, which was necessary for high OER activity because IrO_2 binds the O* too strongly compared to an ideal OER catalyst. Grimaud *et al.* reported another DP-type La_2LiIrO_6 catalyst towards OER. Their study had

suggested that an activation of surface oxygen through oxidation of the catalyst surface could lead to the modification of Ir coordination and highly active OER catalysts.[64]

More recent studies had demonstrated outstanding OER activity by multi-phases Ir-based perovskite-type and pyrochlore-type catalysts that possess highly active IrO_x surface layers generated during OER conditions. Seitz *et al.* reported a $IrO_x/SrIrO_3$ catalyst, in which the IrO_x active surface layer was formed during OER testing by A-site Sr leaching.[66] Surface analysis had shown the decrease intensity of Sr after 30 min of OER testing and OER activity had increased during the first 2 h of OER testing. Density functional theory (DFT) suggested that the surface IrO_x layer may be IrO_3, anatase IrO_2 or similar structures. The $IrO_x/SrIrO_3$ catalyst out performed most of the existing OER catalyst in acidic electrolyte with 0.27 V overpotential at 10 mA cm^{-2} and showed extremely high OER durability for more than 30 h. Similar phenomenon was shown in pyrochlore-type structure $IrO_x/Y_2Ir_2O_7$.[67] Lebedev *et al.* showed that the pyrochlore-type $Y_2Ir_2O_7$ catalyst had the similar behavior like the $SrIrO_3$. The A-site Y leached out during the OER testing conditions leaving an active surface IrO_x layer and contributing high OER activity. The OER stability for $IrO_x/Y_2Ir_2O_7$ was tested with stepping potential cycles and the catalyst maintained high current density within 500 cycles.

Table 1.2 Summary of ternary structure metal oxide OER catalysts in acid. (PLD = pulsed laser deposition)

Material	Electrolyte	Catalyst loading (mg cm^{-2})	η @ 10 mA cm^{-2} (mV)	Stability	Ref.
RuO_2 NP	0.1 M $HClO_4$	0.05	450	-	[69]
IrO_2 NP	0.1 M $HClO_4$	0.05	440	-	[69]
$IrO_x/SrIrO_3$	0.5 M H_2SO_4	PLD Film	270	10 mA cm^{-2} for 30 h	[65]
$IrO_x/Y_2Ir_2O_7$	0.1 M $HClO_4$	0.102	~ >370	Stepped 1.6 V for 500 cycles	[66]
6H-$SrIrO_3$	0.5 M H_2SO_4	0.90	248	10 mA cm^{-2} for 30 h	[67]
Ba_2YIrO_6	0.1 M $HClO_4$	0.015	340	10 mA cm^{-2} for 1 h	[62]
La_2LiIrO_6	0.1 M H_2SO_4	0.250	~350	20 A g^{-1} for 50 cycles	[63]
$(Na_{0.33}Ce_{0.67})_2(Ir_{1-x}Ru_x)_2O_7$	0.5 M H_2SO_4	N/A	~250	N/A	[61]
$Bi_2Ir_2O_7$	1 M H_2SO_4	0.402	~360	0.02 – 1.5 V 1,000 cycles	[59]
$Pb_2Ir_2O_{6.5}$	0.1 M $HClO_4$	0.2	~390	N/A	[60]

As mentioned previously, one of the major challenges for developing catalysts in acid electrolyte is the stability of catalysts. Even for noble metal catalysts, RuO_2 is not ideal for long-term application.[10,70,71] Ir-based perovskite materials showed good OER activities, however, their OER stabilities and application on continuous water electrolyzers are questionable. Ba_2PrIrO_6 and Ba_2YIrO_6 DPs showed decay in activity after 1 h continuous testing.[40] La_2LiIrO_6 was not possible for a long-term stability test.[64] $SrIrO_3$, on the other hand, had Sr leached out during the OER testing. A structure that stabilizes the active metal centers, such as Ru and Ir, is desirable to enable PEM based water electrolyzers.[69,71] Recently, Gerbrand Ceder *et al.* reported that during the charging state of lithium garnets (LLZO, $Li_7La_3Zr_2O_{12}$), $La_2Zr_2O_7$ pyrochlore was one of the interphases that most likely will form by DFT calculation.[72] **Figure 1.7** showed the phase diagram of LLZO | $LiCoO_2$ (LCO) system at 3 V vs. Li. The LLZO decomposed and formed different interphases with varying reaction energies. It was found that La_2O_3, $La_2Zr_2O_7$ and Li_2CoO_3, with one of them being the pyrochlore structure, had the lowest reaction energy, meaning it had the highest driving force for reaction. Their results give us a hint that pyrochlore structure may be thermodynamically stable when multiple metal ions and oxygen are presented.

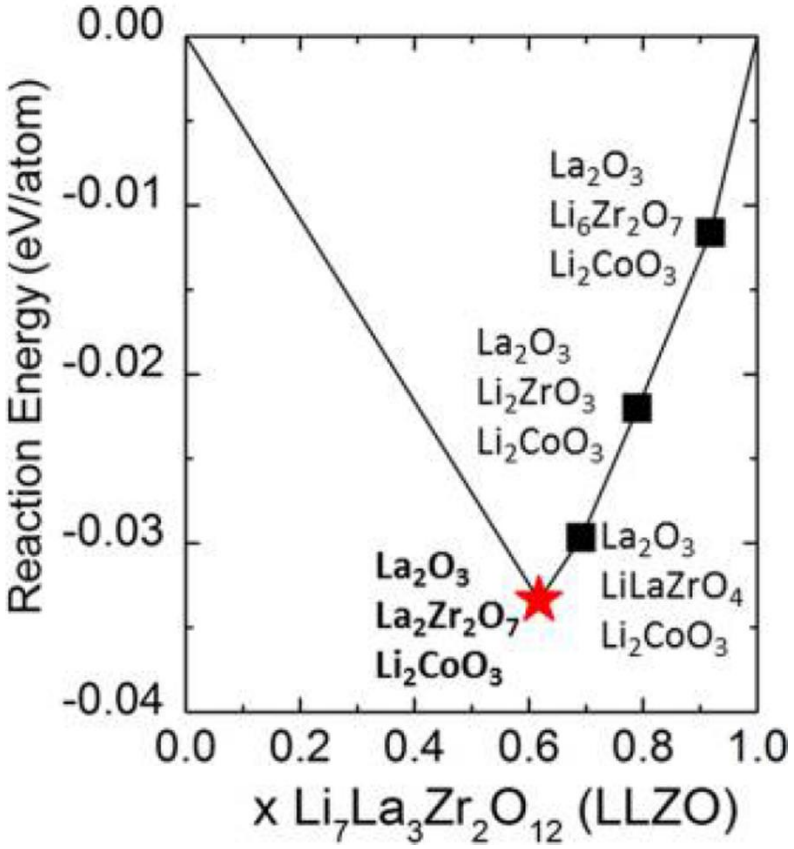

Figure 1.7 LLZO | LCO phase diagram. The most likely reaction is marked with a red star.[72]

1.4 Recent development on the mechanistic study of OER

To accelerate and facilitate the design of active OER catalysts, an understanding of the origins of OER activity descriptors are essential. Due to the complex, multi-step, solution-phase reaction mechanism, researchers have proposed numerous theories related to OER in recent years, both experimental and theoretical.[9,11,17,27,36,40,64,73-77] Theoretical calculation techniques, such as DFT, expanded the field dramatically by calculating more complex structures and screening new catalysts with high-throughput. A short summary of some of these breakthroughs are discussed here.

Shao-Horn Yang *et al.* studied first-row transition metal perovskite oxides and proposed that OER activity was related to an "e_g-filling principle," based on both experimental data and theoretical analysis.[11,17] This approach begins with the assumption that the binding between the catalyst surface with oxy-species (OOH^* and OO^*) are highly relevant to OER activity, as mentioned above. The *d*-orbital configuration of B-site metal cation in a perovskite plays a key role in this interaction. As the occupancy of electrons in the e_g-orbital increases, the binding to oxygen decreases, making the formation of OOH* the RDS (eq. 1.6). On the other hand, when e_g occupancy is low, the RDS shifts to the formation of OO* at metal surface (eq. 1.7) because the binding between the metal cation and oxygen is too strong. These two situations can be explained by the electronic geometry of the B-site metal: at the catalyst surface, BO_5 (square pyramid) coordination is formed with a vacant oxygen-site normal to the surface (**Figure 1.8a**). This vacant site can bind with surface intermediates such as oxygen. Adsorbed oxygen converts BO_5 to a pseudo-BO_6, hybridizing the O 2p-orbital and forming σ, π orbitals. The normal BO_5 orbitals in the perovskite (e_g and t_{2g}) split and become antibonding orbitals (σ^* and π^*). Notably, e_g is higher in energy and splits further away from t_{2g} when the symmetry breaks to pseudo-BO_6 (**Figure 1.8a** and **b**).[17] Yang *et al.* concluded that a moderate e_g occupancy is critical for an ideal catalyst, as displayed in their experimental observations (**Figure 1.8c**).[11] For example, the B-metal cation in $LaCrO_3$ is Cr^{3+} which has zero e_g electrons, resulting in a strong binding of Cr-O and limiting the overall OER activity (1.76 V at 50 μA cm^{-2}_{ox}). In contrast, $LaCoO_3$ uses Co^{3+} (one e_g electron) and has a potential of 1.58 V at the same current density.

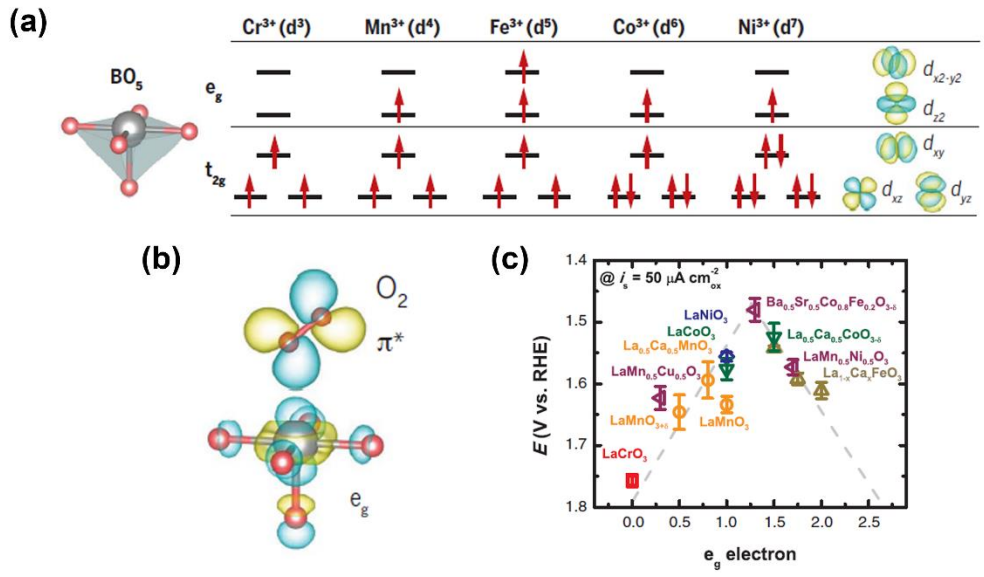

Figure 1.8 E_g orbital filling theory for perovskite oxides in OER. (a) BO_5 surface configuration and electron filling for common first-row transition metals in perovskites.[17] (b) Illustration of the binding of O_2 π^* orbital to an empty e_g orbital.[17] (c) Relation between OER activity (E, overpotential at 50 μA cm_{ox}^{-2}) and e_g electron filling for many perovskite oxides.[11]

Keith P. Johnston and Thomas J. Schmidt *et al.* proposed a lattice-oxygen mediated mechanism (LOM) model,[27,78] suggesting that oxygen defects was key to high OER activity. Oxygen vacancies change the oxidation state of metal cations and create a ligand hole in the band structure. This ligand hole causes fast oxygen diffusion rate and facilitates OER. In addition, the covalency between B-site metal cation and oxygen increases as the band energy decreases which is beneficial for catalyzing OER, according to LOM model. They used a $La_{1-x}Sr_xCoO_{3-\delta}$ perovskite catalyst to demonstrate the concept. With strontium cation (Sr^{2+}) substitution, the oxidation state of cobalt increased to balance the charge, increasing the covalency of Co-O bond and lowering the Fermi level into the Co 3d-orbital and O 2p-antibonding orbital. This electronic response creates

ligand holes. During OER, anodic potential oxidizes the ligand hole and enables interactions between the lattice oxygen and absorbed intermediates. The resulting mechanism for LOM is shown in **Figure 1.9.** Initially lattice species are shown in red, whereas adsorbates are blue. OO* intermediates are generated by one oxygen atom from the lattice and the other from an adsorbed species (step 1). The partial density of states (PDOS) diagram (bottom, **Figure 1.9**) shows how valence electrons near the Fermi Level are impacted during LOM. First, the ligand hole is generated (step 1E) due to the anodic potential, then an O atom is released from the lattice to the surface intermediate and pin the Fermi level at top of the Co 3d and O 2p π^* band (step 1C). Based on this mechanism, the surface lattice oxygen reactivity and the presence of oxygen vacancy defects are critical to the OER activity. Similar theory had been reported by other works. Grimaud *et al.* had demonstrated that in their La_2LiIrO_6 catalyst, the activation of surface oxygen sites and surface restructuring were critical factors towards active OER catalysis.[64]

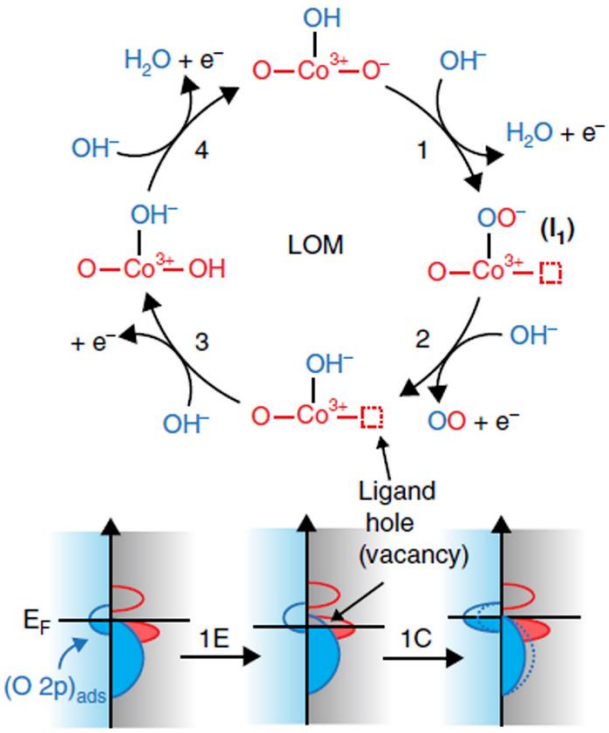

Figure 1.9 Elemental steps and PDOS diagram of LOM on $La_{1-x}Sr_xCoO_{3-\delta}$ for OER. Electrolyte species are indicated in blue and the lattice species are indicated red. Electrolyte species are shown to the left of energy axis and lattice species are shown to the right in the PDOS diagram.[27]

Density functional theory (DFT) calculation is a powerful tool for unraveling intrinsic properties of electrocatalysts. Although the accuracy of energies associated with oxide-based materials often deviate from experimental results, it is useful for screening materials and predicting thermodynamic properties.[9,66] Since Rossmeisl and Nørskov *et al.* proposed the DFT calculation of OER on oxide surfaces,[7,14] expanding researches have been reported with DFT results to illustrate the OER kinetics. Nørskov *et al.* suggested that there was a linear relation between O^* binding energy and other oxygen species on oxide surfaces, which made it possible to predict a trend of OER activity by a single factor, namely, O^* binding energy to the catalyst surface (ΔG_O).

Using the scaling relation between binding energies of OOH* (ΔG_{OOH}) and OH* (ΔG_{OH}), it is possible to calculate and predict the active OER surfaces with the lowest overpotential. Seitz *et al.* calculated ΔG_{OOH} and ΔG_{OH} on different IrO_x surfaces and found a linear relation of $\Delta G_{OOH} = \Delta G_{OH} + 3.00$, similar to other scaling relations for metal oxides (**Figure 1.10a**).[66] Using $\Delta G_O - \Delta G_{OH}$ as a descriptor, they showed that a IrO_3 and anatase-IrO_2 surfaces result in high OER activity with a 0.3 V overpotential (**Figure 1.10b**).[66] The activity of surface IrO_x, formed by strontium-leaching during acid-based OER from a $SrIrO_3$ electrode, validated their results. Although characterization of the formed IrO_x structures within the $IrO_x/SrIrO_3$ surface was insufficient, the DFT result gave insights for screening OER catalysts.

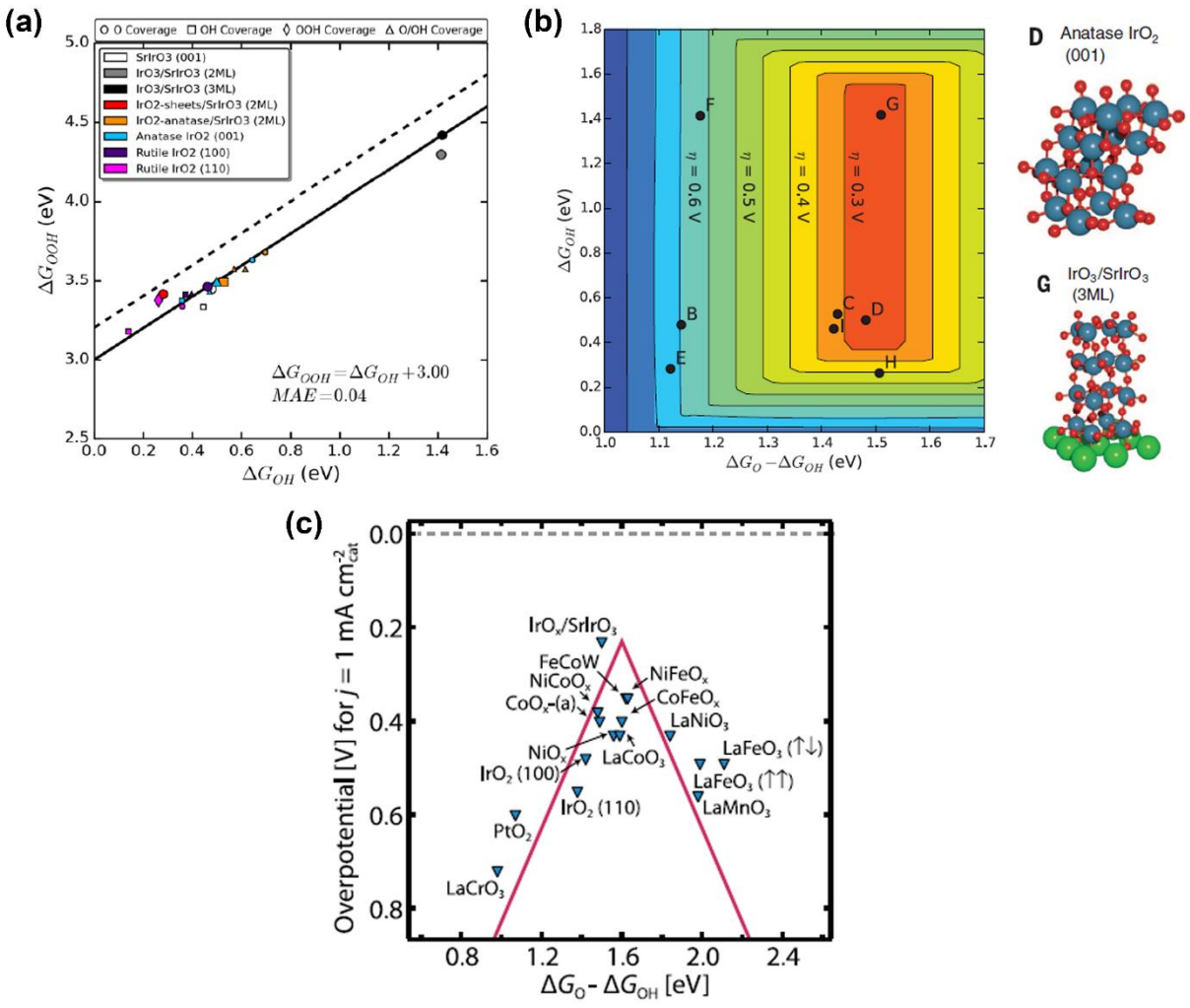

Figure 1.10 DFT calculation of the oxygen binding energy on oxide surfaces as OER activity descriptor. (a) The scaling relation of ΔG_{OOH} and ΔG_{OH} on different IrO_x surfaces.[66] (b) Theoretical OER overpotentials (η) using ΔG_O and ΔG_{OH} as descriptors. D and G represent the most active surfaces which are calculated to have a low η of 0.3 V.[66] (c) Volcano plot of experimental OER activities versus theoretical descriptor $\Delta G_O - \Delta G_{OH}$.[9]

1.5 Strategies to enhance OER activity

In addition to the optimization of chemical composition, many techniques have been employed to enhance the OER activity of catalysts. Usage of expensive, noble metals like iridium and ruthenium are potentially unavoidable due to their high OER activity and stability,[28,66,79] thus one strategy is to increase the number of active sites per unit volume by designing nanostructures and porous materials. As mentioned previously, perovskite-type and pyrochlore-type structures offer many benefits to OER activity. However, high temperature annealing is often required to synthesize these ternary metal oxides. Unavoidable sintering commonly happens, destroying most nanostructures. In our work, we developed a sol-gel synthesis for a calcium- and manganese-based perovskite ($CaMnO_3$ and $CaMnO_{2.5}$).[26] **Figure 1.11a** shows the scanning electron microscopy (SEM) image of the as-made $CaMnO_{2.5}$, which are submicron-sized particles. The sol-gel synthesis effectively reduced the required temperature to form this material as compared to traditional solid-state reaction techniques. We also developed a hydrothermal synthesis method to produce a $LaCoO_3$ perovskite in the form of highly-porous, hollow nanospheres.[13] Uniform size and shape can be achieved with precise control of the synthesis conditions.[18,80,81] **Figure 1.11b** shows the schematic of the hydrothermal synthesis. Multiple heating steps are required to achieve the hollow nanosphere. **Figure 1.11c** shows the SEM image of nanosphere and the nanostructures can be seen clearly in a transmission electron microscopy (TEM) image (**Figure 1.11d**). Others have also reported porous pyrochlore-type materials.[56,82,83] Oh *et al.* used a surfactant-templating method to synthesize mesoporous $A_2Ru_2O_{7-\delta}$ (A = Pb, Bi) pyrochlore materials (**Figure 1.11e**).[56] The $Pb_2[Ru_{1.7}Pb_{0.3}]O_{6.5}$ material had mesopores of ~3.8 nm with a surface area of 155 $m^2\ g^{-1}$. Owing to its porosity, the catalyst showed great performance in Li-air batteries.

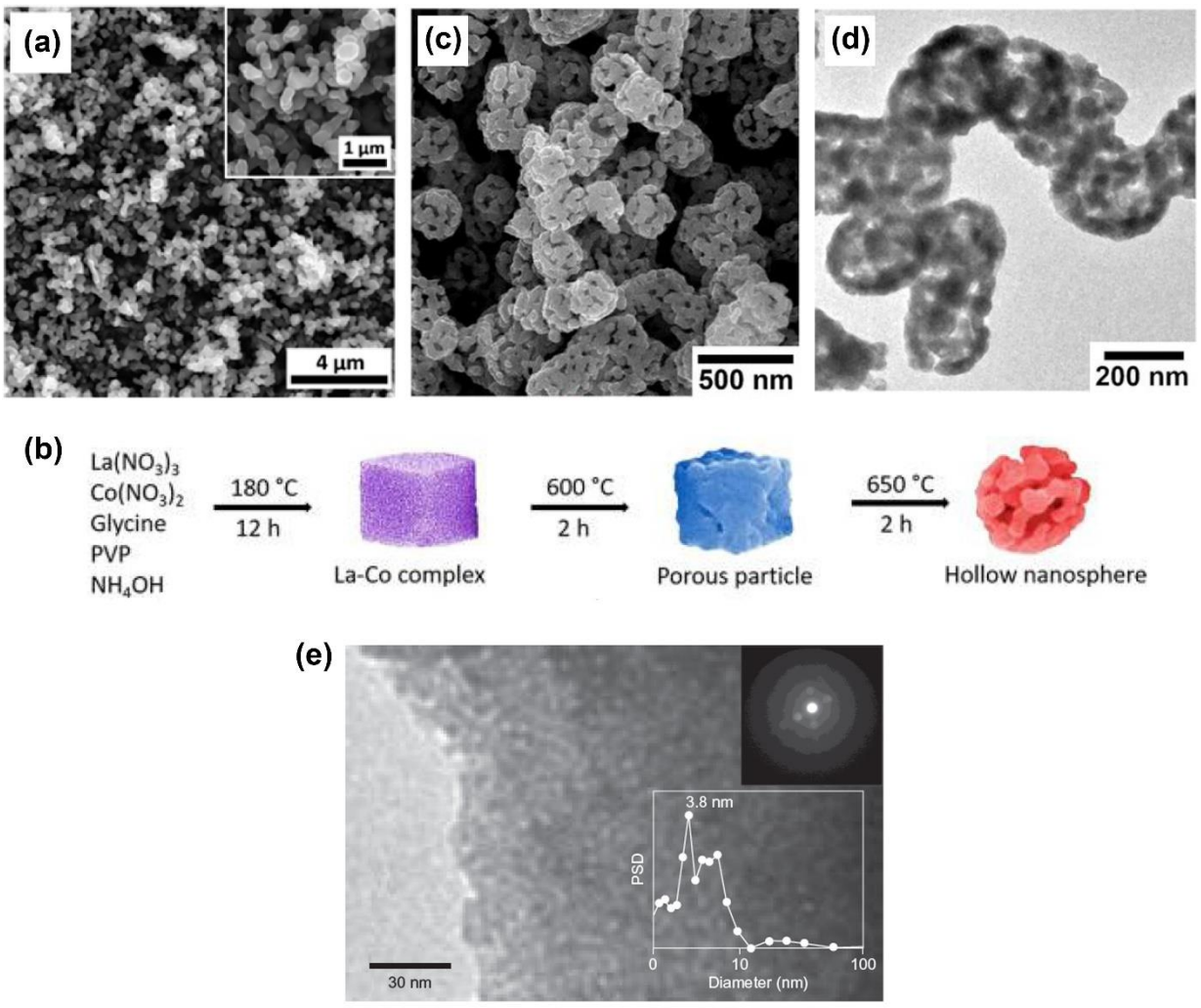

Figure 1.11 Synthetic results of perovskite oxide materials. (a) SEM image of $CaMnO_{2.5}$ perovskite with submicron-sized particles. Inset shows a magnified image.[26] (b) Schematic of the hydrothermal synthetic procedures of porous $LaCoO_3$ perovskite.[13] (c) and (d) SEM and TEM images of $LaCoO_3$ with hollow sphere nanostructures.[13] (e) TEM image of the mesoporous $Pb_2Ru_2O_{6.5}$ pyrochlore. Insets show the selected area electron diffraction (SAED) and pore size distribution (PSD) of the material.[56]

Many perovskite-type and pyrochlore-type oxides exhibit low conductivity compared to other metallic oxides and metal catalysts.[84] Because OER requires multiple electron transfers, enhancing the conductivity of these materials is another strategy to improve OER activity. In some cases, the interface of the carbon support and the material can serve as the active site, but is often insufficient.[35] In our previous work, we reported a mixed perovskite oxide of $CaMn_{0.97}W_{0.03}O_3$ which had high valence state of tungsten (W^{6+}) substituted at 3% of the manganese B-sites.[53] Known as the double-exchange mechanism, small amounts of doped W^{6+} induced manganese to mixed valence states (Mn^{4+} and Mn^{2+}) for charge balancing. Because the electrons from Mn^{2+} could hop to adjacent Mn^{4+} through oxygen *2p* orbitals,[85] the electrical conductivity of the perovskite increased without sacrificing the catalytic sites of manganese.[86] This phenomenon increased the overall activity as compared to $CaMnO_3$.

Other methods to enhance OER activity of catalysts had been reported. Mefford *et al.* reported a $La_{1-x}Sr_xCoO_{3-\delta}$ perovskite.[27] By modifying the of La^{3+} and Sr^{2+} amounts in the structure, Co-O covalence changes, and oxygen defects form at the catalyst surface, making the surface more reactive for OER. Song *et al.* reported a CoMn layered double hydroxide (LDH) that was highly active towards OER due to an amorphous catalyst surface which was generated by anodic conditioning.[55]

1.6 Scopes of research and thesis arrangement

This thesis focuses on developing new catalyst materials work towards OER in an acidic electrolyte system. These materials must be (1) OER active in acid; (2) acid durable during OER testing; and (3) cost effective with minimal usage of expensive elements. The ultimate goal is to enable hydrogen production through PEM-based water electrolysis. Ru- and Ir-based pyrochlore

structures are selected, which is inspired by the success of ternary metal oxides in alkaline OER and the possibility of stable structure during a lithium garnet charging and decomposing process. The project has three main focuses:

1. Identifying the best pyrochlore composition to enhance OER activity and stability
2. Understanding the relationship between material properties and OER activity to propose and predict the catalyst behavior of new materials.
3. Designing the syntheses of stable and porous pyrochlore nanostructures.

In a broader view, the material design for OER catalysts is related to other technologies such as metal-air batteries, fuel cells, photoelectrochemical water splitting, CO_2 reduction and nitrogen reduction etc. because of their similarity in chemistry. The development and understanding of OER catalysts can be applied and extended to those reactions. Finally, advance the technology and mitigate the rising energy and environment issues.

In the following sections, Chapter 2 presents the pyrochlore-type yttrium ruthenate OER catalyst in acid. The design of compositions ($Y_2Ru_2O_{7-\delta}$ and $Y_2[Ru_{1.6}Y_{0.4}]O_{7-\delta}$), DFT calculation, electrochemical impedance spectroscopy (EIS) and synthetic approach of porous $Y_2[Ru_{1.6}Y_{0.4}]O_{7-\delta}$ are contributed by Dr. Jaemin Kim. Chapter 3 presents the high surface area $Y_2Ru_2O_{7-\delta}$ produced by a low temperature polymeric entrapment synthesis. Chapter 4 presents the pyrochlore-type yttrium iridate OER catalyst in acid. Chapter 5 presents a systematic study of OER descriptors using a series of lanthanide iridate pyrochlores. Chapter 6 presents the concluding remarks of this dissertation.

CHAPTER 2

YTTRIUM- AND RUTHENIUM-BASED PYROCHLORE OXIDES ($Y_xRu_yO_{z-\delta}$) AS OXYGEN EVOLUTION REACTION CATALYSTS[1,2]

2.1 Introduction

As mentioned in the previous chapter, OER plays a critical role in hydrogen production via water electrolysis. OER catalysts suffer from slow reaction kinetics and/or poor stability in acid. The inefficiency mainly results from the sluggish proton-coupled electron transfer to the oxygen intermediate species over the catalyst surface.[9,15,26,50,56,87-97] While an acidic condition is preferable for OER because of high ionic (proton) conductivity and fewer side reactions,[62] feasible electrocatalysts used in low pH solutions are limited, because most of the known active compounds are unstable under the harsh acidic operating conditions.[69,98] To date, RuO_2 and IrO_2 are the best traditional OER catalysts in acidic media. Between the two, IrO_2 tends to have higher stability while RuO_2 typically has higher activity.[10,70,71] Many ruthenium-based electrocatalysts have been reported to be active toward OER in alkaline and nonaqueous media but lack of high stability in acids.[56,59,99]

In this chapter, I will present a cost-effective (i.e., Ir-free), phase-pure pyrochlore $Y_2Ru_2O_{7-\delta}$ electrocatalyst with high activity and stability toward OER in strong acidic media. $Y_2Ru_2O_{7-\delta}$ electrocatalyst shows an ultralow onset overpotential of less than 200 mV in 0.1 M perchloric acid solution and stable chronopotentiometric performance under constant current

[1] Modified with permission, from Kim, J. †; Shih, P.-C. †; Tsao, K.-C.; Pan, Y.-T.; Yin, X.; Sun, C.-J.; Yang, H. *J. Am. Chem. Soc.* **2017**, *139*, 12076-12083.
[2] Modified with permission, from Kim, J.; Shih, P.-C.; Qin, Y.; Al-Bardan, Z.; Sun, C.-J.; Yang, H. *Angew. Chem. Int. Ed.* **2018**, *57*, 13877-13881.

density. Structural origins for the enhanced OER activity and stability performance of $Y_2Ru_2O_{7-\delta}$ electrocatalyst over the reference catalyst (RuO_2) were examined using X-ray absorption near-edge structure (XANES), extended X-ray absorption fine structure (EXAFS), and X-ray photoelectron spectroscopy (XPS), in conjunction with first-principle calculations. Powder X-ray diffractometer (PXRD), trans- mission electron microscopy (TEM), and inductively coupled plasma-mass spectroscopy (ICP-MS) provided further structural details of these electrocatalysts before and after the OER tests.

I will also show a new synthetic strategy to prepare the porous pyrochlore oxide as high-performance OER electrocatalyst. By applying a heating condition for rapid thermal decomposition of perchloric acid, a new porous pyrochlore oxide was prepared. Phase pure porous $Y_2[Ru_{1.6}Y_{0.4}]O_{7-\delta}$ pyrochlore oxide was synthesized, where substantial increase in OER activity (low overpotential and fast kinetic rate) was observed in comparison with those of $Y_2Ru_2O_{7-\delta}$ that made by sol-gel synthesis, RuO_2, and IrO_2 in perchloric acid solution. PXRD, XANES spectra, EXFAS spectra, and energy-dispersive X-ray spectroscopy (EDS) study show that this new porous electrocatalyst possess an intriguing, mixed B-site pyrochlore structure of $Y_2[Ru_{1.6}Y_{0.4}]O_{7-\delta}$, which results in the defects of lattice oxygen. This change is the result of mixed valencies of $Ru^{4+/5+}$ because of partial replacement of B-site Ru^{4+} with Y^{3+}, and likely further contribute to the observed outstanding OER performance.

2.2 Experimental procedures

2.2.1 Material synthesis

$Y_2Ru_2O_{7-\delta}$ was synthesized using a sol-gel synthetic method. The stoichiometric amounts of $Y(NO_3)_3 \cdot 6H_2O$ (99.9%, Alfa Aesar, 0.1915 g) and $Ru(NO)(NO_3)_x(OH)_y$ (Sigma-Aldrich, 3.087 mL) were mixed in 10 mL of water (18.2 MΩ-cm resistivity, Millipore) while stirring, followed by addition of citric acid (99%, Fisher Chemical, 0.4203 g). The mixture solution was transferred to an oil bath and heated up to 80 °C and kept at this temperature for 5 h. The water was evaporated overnight under 80 °C and further removed in a vacuum oven (~10 mmHg, VWR symphony) at 120 °C for additional 6 h. The obtained solid was then heated up to 600 °C at a rate of 5 °C/min and maintained at this temperature for 6 h. After cooling down to room temperature, the solid was then transferred to a tube furnace and heated to 1000 °C at a rate of 5 °C/min and maintained at this temperature for 12 h. Reference RuO_2 (99.9%, Sigma-Aldrich) powder was used without further purification.

Porous $Y_2[Ru_{1.6}Y_{0.4}]O_{7-\delta}$ pyrochlore was made with a modified sol-gel synthesis and perchloric acid as the pore generation reagent. 0.09579 g (or 0.25 mmol) of $Y(NO_3)_3 \cdot 6H_2O$ (Sigma-Aldrich, 99.9%), 1545 µL (or 0.25 mmol) of $Ru(NO)(NO_3)_x(OH)_y$ (Sigma-Aldrich), 0.2101 g (or 1 mmol) of citric acid (Fisher Chemical, 99%), and 85 µL of perchloric acid (Veritas® double distilled, 70%) were dissolved in 5 mL of water in a 20 mL vial. The vial was then transferred to an oil bath, heated to 80 °C, and maintained at this temperature for about 12 h until water evaporated and gel-like solid formed. The solid was transferred to a quartz boat and subjected to a sequential heat treatment at 600 °C for 6 h and 960 °C for 6 h at a heating rate of 5 °C/min (GSL-1500X, MTI Corporation). **Caution:** The heat treatment of the precursor mixture

must be performed in a well-ventilated fume-hood because of the rapid thermal decompostion of perchloric acid at 120 ℃.

2.2.2 Material characterization

The crystal structures were analyzed by XRD (Bruker D8 Venture) equipped with Photon 100 detector and Cu X-ray source. The measurement was performed in transmission mode, typically between 5° and 100° 2θ. TEM and HRTEM (JEOL 2100 Cryo) were carried out at an acceleration voltage of 200 kV. TEM specimen was prepared by dispersing a suspension in ethanol on a carbon-coated copper grid. SEM (Hitachi S4700) images were obtained at an acceleration voltage of 15 kV. SEM specimen was prepared by directly depositing electrocatalyst powders on carbon tape on a SEM stub.

ICP-MS analysis was performed on a Perkin-Elmer SCIEX ELAN DRCe ICP-MS system to study the stability of $Y_2Ru_2O_{7-\delta}$ electrocatalyst. The loading amounts of carbon-supported $Y_2Ru_2O_{7-\delta}$ catalysts varied from 25 µg to 50 µg. After 10,000 CV cycles at a scan rate of 100 mV/s between 1.35 V to 1.60 V in 300 mL of 0.1 M perchloric acid ($HClO_4$) solution, the electrolyte was concentrated to a final volume of ~10 mL for ICP-MS analysis.

Brunauer-Emmett-Teller (BET, Micrometrics Gemini VII 2390) analysis was performed for the surface area calculation of the catalysts with 6-point measurement under an N_2 adsorption environment. The measured catalyst surface areas were 7.2 ± 0.02 $m^2\ g^{-1}$ for $Y_2Ru_2O_{7-\delta}$ and 11.2 ± 0.02 $m^2\ g^{-1}$ for RuO_2. The surface area for Vulcan carbon XC-72 was 254 $m^2\ g^{-1}$.[100]

Ru K-edge X-ray absorption spectroscopy (XAS) spectra were collected in transmission mode using beamline 20-BM-B at the Advanced Photon Source (APS), Argonne National

Laboratory, USA. The pressed pellet specimens were made of mixtures of either $Y_2Ru_2O_{7-\delta}$ or RuO_2 powder with boron nitride. The obtained XAS data were analyzed using the Athena software. The extracted EXAFS signal, χ(k), was weighted by k^2 in *k*-range from 3.8 $Å^{-1}$ to 15.6 $Å^{-1}$ to obtain the magnitude plots of the EXAFS spectra in radial space (Å).[101]

XPS analysis was performed with Al Kα x-ray source. For as-made $Y_2Ru_2O_{7-\delta}$ catalyst, powder sample was directly measured on copper tape. For the end of life sample, the $Y_2Ru_2O_{7-\delta}$ catalysts were loaded onto fluorine-doped tin oxide (FTO) glass for cycle tests and then measured by XPS. The data processing and peak fitting were performed using the CasaXPS software. The measured Ru 3d peak was fit by using two sets of doublets with an additional component for C 1s. Each of the doublets were set to have a binding energy difference of 4.17 eV and areas at a ratio of 3:2. The Y 3d peaks were fit using the similar method by using two sets of doublet with binding energy of 2.05 eV and areas at a ratio of 3:2 as well.[102] The full width half maximum (FWHM) is summarized in **Table 2.6**.

2.2.3 Electrochemical measurement

Vulcan carbon XC-72 was used as the support for these catalysts. In a typical procedure, 1 mL of Nafion 117 aqueous solution (5%, Sigma-Aldrich) was mixed with 0.1 M NaOH solution to adjust the pH value to between 8 and 9. A mixture of 2 mg of carbon black and 2 mg of metal oxide were added in 2 mL of tetrahydrofuran (THF) with 3 µL of the pre-processed Nafion. The final mixture was sonicated for 30 min to obtain a homogeneous suspension. 5 µL of this catalyst ink was drop-cast on a rotating disk electrode (RDE) and dried slowly to form a thin film working electrode. After the ink dried, 10 µL of the pre-processed Nafion in tetrahydrofuran (THF, 3 µL of Nafion in 2 mL THF) was drop-cast on the working electrode and dried in air to form a uniform

thin film electrode. A three-electrode cell was used to measure the performance. The cell is composed of a glassy carbon working electrode (surface area: 0.196 cm^2), a counter electrode made of platinum wire (diameter: 0.5 mm) connected with platinum foil (area: 1 cm^2), and a hydrogen reference electrode (HydroFlex, Gaskatel). The reference electrode was calibrated in H_2 (S. J. Smith, 99.999%) saturated 0.1 M $HClO_4$ (Veritas, 70 %) solution before testing. All measurements were performed after purging with O_2 (S. J. Smith, 99.999 %) in this $HClO_4$ solution for at least 30 min. Carbon corrosion or oxidation was negligible under the tested potential ranges, thus rotating ring disk electrode (RRDE) OER experiment was not necessary. Cyclic voltammagrams (CVs) were collected at a scan rate of 10 mV/s typically between 1.1 V and 1.6 V for the 1st and 10,000th potential cycles. The RDE rotating speed was set at 1600 rpm. For stability study, the scan rate was set at 100 mV/s with the potential range between 1.35 V and 1.6 V for 9998 cycles. Chronopotentiometric measurements for both $Y_2Ru_2O_{7-\delta}$ and RuO_2 were obtained using RDE, by applying constant current up to 8 h. For XPS study, 10,000 CVs were performed with the $Y_2Ru_2O_{7-\delta}$ electrocatalyst on an FTO substrate without Nafion and carbon support to minimize the interference of Ru 3d signals by carbon (C 1s). Resistance of the test cell was measured to be ~24 Ω after the *iR* compensation, and in the same $HClO_4$ solution after the CV tests with RDE. The capacitance was corrected by taking the average of anodic and cathodic scans. Electrochemical impedance spectroscopy (EIS) measurements were performed at three different potential values using the electrodes made of $Y_2Ru_2O_{7-\delta}$ and RuO_2, respectively, with the frequency range from 1×10^4 Hz to 0.1 Hz. For each test, 60 μL of ink was deposited onto the disk and a 0.1 M $HClO_4$ solution was used as the electrolyte. The impedance spectra were presented in the form of Nyquist plot and fitted using ZView software. All potential values are versus reversible hydrogen electrode (RHE), unless stated otherwise.

2.2.4 Density functional theory (DFT) calculation

The projected density of states (DOS) for O 2p and Ru 4d orbitals were obtained by DFT calculation using the plane-wave basis code CASTEP with ultrasoft pseudopotentials. The generalized gradient approximation (GGA) with the PW91 function was used to calculate the electronic exchange and correlation. An optimal U_{eff} of 4.0 eV was applied to Ru d electrons for both $Y_2Ru_2O_7$ and RuO_2. The cut-off energy for plane-wave basis set was set to 340 eV. A unit cell of 127 atoms was used for the calculation of pyrochlore-type $Y_2Ru_2O_7$, in which Monkhorst-Pack scheme k-point grid was set to 4×4×4. A 2×1×1 supercell was used for the calculation of RuO_2 with k-point grid of 2×3×5. The convergence thresholds were set as 1×10^{-5} eV/atom for the energy, 3×10^{-2} eV/Å for the force, and 1×10^{-3} Å for the displacement. The p or d band center $E_{p(d)}$ was calculated based on the following equation: $E_{p(d)} = \int \rho E dE / \int \rho dE$, where ρ is the projected electron DOS at the energy level of E. The calculated overlapped Ru 4d and O 2p band centers were -4.78 eV for $Y_2Ru_2O_7$ and -4.45 eV for RuO_2.

2.2.5 Turnover frequency (TOF) calculation

The TOF was estimated using the following formula, assuming 100% Faradaic efficiency:

$$TOF = \frac{R_{O_2}}{N_{Ru}} \qquad (2.1)$$

where TOF is the turnover frequency, R_{O_2} is the rate of O_2 formation and N_{Ru} is the number of surface Ru atoms. The rate of O_2 formation is obtained from the measured current density, j and surface area of the metal oxide, A, according to the following equations:

$$R_{O_2} = j_{oxide}\, A_{oxide}\, F^{-1}\, n_e^{-1}\, N_A \qquad (2.2)$$

where j_{oxide} is the specific current, A_{oxide} is the surface area of oxide, F is the Faraday constant, n_e is the number of electrons transferred per mole of O_2 produced, which is 4 in here, and N_A is Avogadro's number. The number of Ru sites is calculated using the formula:

$$N_{Ru} = n_{Ru}\, m_{oxide}\, N_A\, Mw_{oxide} \qquad (2.3)$$

where n_{Ru} is the number of Ru atoms in the oxide formula, m_{oxide} is the mass of oxide used and Mw_{oxide} is the molecular weight of oxide.

2.3 Results and discussion

2.3.1 Structure analysis of $Y_2Ru_2O_{7-\delta}$ catalysts

Phase-pure $Y_2Ru_2O_{7-\delta}$ was synthesized by the sol-gel method. This technique is capable to produce submicron-sized particles, unlike the direct solid-state synthesis method.[103] **Figure 2.1a** shows the PXRD pattern of the as-prepared $Y_2Ru_2O_{7-\delta}$ catalysts. All diffraction peaks matched well with those of cubic phase (*Fd-3m*) pyrochlore-type $Y_2Ru_2O_7$ (JCPDS No. 01-081-2340, **Table 2.1**), indicating a phase pure product. Using the Rietveld refinement, the unit length was calculated to be 10.2 Å (**Table 2.1**). Scanning electron microscopy (SEM) images show $Y_2Ru_2O_{7-\delta}$ powders were made of granular, submicron-sized particles (**Figure 2.1b**). In this pyrochlore structure, there exist two types of oxygen ($A_2B_2O_6O'$); the O anion that links two building blocks to form network between A- and B-site cations, and the O′ anion that connects to only the A-site cations in the form of A-O′-A. Thus, two interpenetrating networks of B_2O_6 and A_2O' sub-lattices exist in this pyrochlore structure as shown in **Figure 2.1c**.[18,104] The structure of $A_2B_2O_6O'$ is flexible and its A-site cation can be replaced with another ion while keeping the same crystal structure.[18]

Table 2.1 Refined parameters for $Y_2Ru_2O_{7-\delta}$

$Y_2Ru_2O_{7-\delta}$	x	y	z
Y	0.62500	0.62500	0.62500
Ru	0.12500	0.12500	0.12500
O1	0.20800	0.00000	0.00000
O2	0.50000	0.50000	0.50000
a = b = c = 10.19085 ± 0.00323 Å, α = β = γ = 90 °, space group Fd-3m, R_{wp} = 9.19 %, R_p = 6.54 %			

$$R_p = \frac{\sum y_i(obs) - y_i(calc)}{\sum y_i(obs)},\ R_{wp} = \left(\frac{\sum w_i(y_i(obs) - y_i(calc))^2}{\sum w_i(y_i(obs))^2}\right)^{1/2},$$

where $w_i = 1/y_i$, $y_i(obs)$ = observed intensity at step i, $y_i(calc)$ = calculated intensity at step i. The Rietveld fitting was carried out using the Reflex module in Materials Studio 6.1 (Accelrys Inc.).

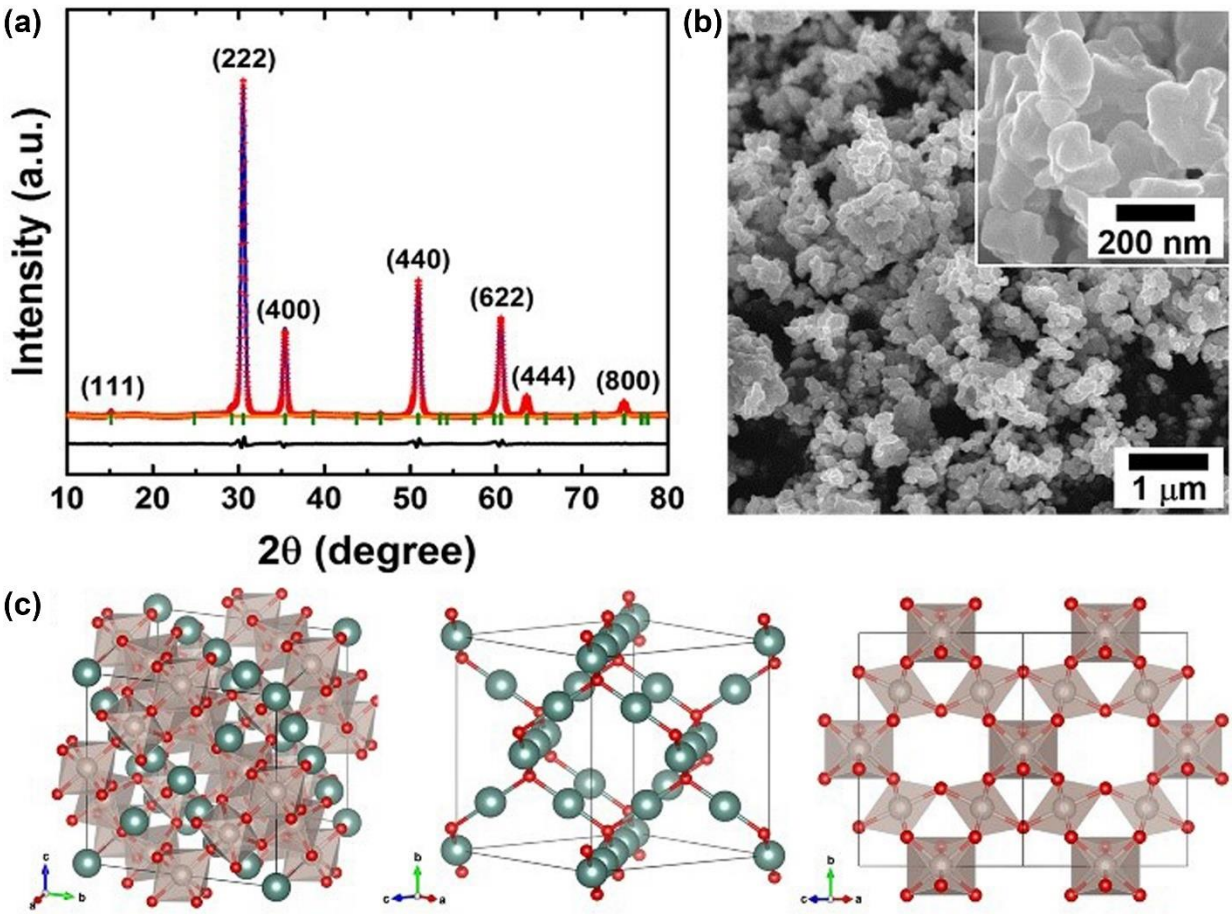

Figure 2.1 Structure of pyrochlore-type $Y_2Ru_2O_{7-\delta}$ electrocatalyst. (a) Rietveld refinement of $Y_2Ru_2O_{7-\delta}$ (cubic, *Fd-3m*): experimental data (red), simulated diffraction (blue), background (orange), position of observed diffractions (green), and the residual plot (black). (b) Representative SEM images. The inset is a magnified image showing the submicron-sized catalyst particles. (c) Unit cell structure of $Y_2Ru_2O_7$ (left) showing the Y_2O' chains (middle) and corner shared octahedral BO_6 structures (right). Color code: Y (teal), Ru (grey) and O (red).

2.3.2 OER catalytic performance of $Y_2Ru_2O_{7-\delta}$ in strong acid

The performance of $Y_2Ru_2O_{7-\delta}$ electrocatalyst towards the oxygen evolution was evaluated using RDE technique in O_2-saturated, 0.1 M perchloric acid solution. The thin catalyst layer was made by depositing a catalyst ink made of inert-carbon supported $Y_2Ru_2O_{7-\delta}$ particles on glassy carbon disk using the neutralized Nafion. **Figure 2.2a** shows the cyclic voltammetry (CV) curves for OER performance of $Y_2Ru_2O_{7-\delta}$ and RuO_2 electrocatalysts for both 1st and 10,000th cycles. Oxidation of this inert-carbon was found to be negligible, judging by the current density measurement for the specimen made from the ink of a mixture of this carbon support and Nafion, despite other types of carbon severely degrade under acid conditions.[76,105] RuO_2 powder was used as the reference electrocatalyst and tested under the same preparation and acidic conditions (**Figure 2.2**). The onset potential of $Y_2Ru_2O_{7-\delta}$ catalyst was measured to be ~1.42 V, which represents an overpotential, η, of ~0.19 V, and is lower than that of RuO_2 catalyst (~1.47 V, η = ~0.24 V).[70] The current contribution from the carbon support and Nafion was negligible during 10,000 cycles under the applied potential range (**Figure 2.2a**). The OER current density of the $Y_2Ru_2O_{7-\delta}$ was determined to be 2.23 mA/cm^2 at 1.50 V based on catalyst surface area. This value is more than six times higher than that of RuO_2 reference catalyst (0.34 mA/cm^2). The superior OER activity of $Y_2Ru_2O_{7-\delta}$ electrocatalyst remained largely unchanged even after 10,000 cycles, decreasing by only 0.17 mA/cm^2. In contrast, RuO_2 catalyst lost most of its activity and its current density became 0.025 mA/cm^2 after 10,000 cycles, showing 1/82 OER activity of that for the $Y_2Ru_2O_{7-\delta}$ catalyst (inset in **Figure 2.2a**). **Figure 2.2b** shows the Tafel plots for both $Y_2Ru_2O_{7-\delta}$ and RuO_2 electrocatalysts with different numbers of CV cycles up to 10,000. The Tafel slope for $Y_2Ru_2O_{7-\delta}$ electrocatalyst changed from the initial value of 55 mV/dec to 46 mV/dec after 10,000 cycles, while the change in overpotential was less than 10 mV. In contrast, the Tafel slope of RuO_2

catalyst increased from the initial value of 61 mV/dec to 72 mV/dec with a significant overpotential increase of more than 70 mV after the cycle test. The onset potential and activity for the freshly-made RuO_2 electrocatalyst were in good agreement with those values previously reported.[7,70]

The difference in catalytic performance was further examined by chronopotentiometry under constant current density. Among the commonly-used evaluation methods,[66,69] current density based on the surface area of catalyst, which represents closely the intrinsic activity, was used in this study. **Figure 2.2c** shows the potential change at the current density of 1.0 mA/cm^2-catalyst,[9] for both $Y_2Ru_2O_{7-\delta}$ and RuO_2 samples. The $Y_2Ru_2O_{7-\delta}$ electrocatalyst started with a potential of 1.50 V (or an overpotential of 270 mV) and remained stable for the entire time of the test. Unlike $Y_2Ru_2O_{7-\delta}$, the potential for reference RuO_2 catalyst changed from 1.55 V to 1.83 V in 45 min and finally to 2.19 V, losing essentially all activity. In short, $Y_2Ru_2O_{7-\delta}$ pyrochlore showed both higher activity and stability than RuO_2 and IrO_2 nanoparticle catalysts reported (**Figure 2.3**).[70]

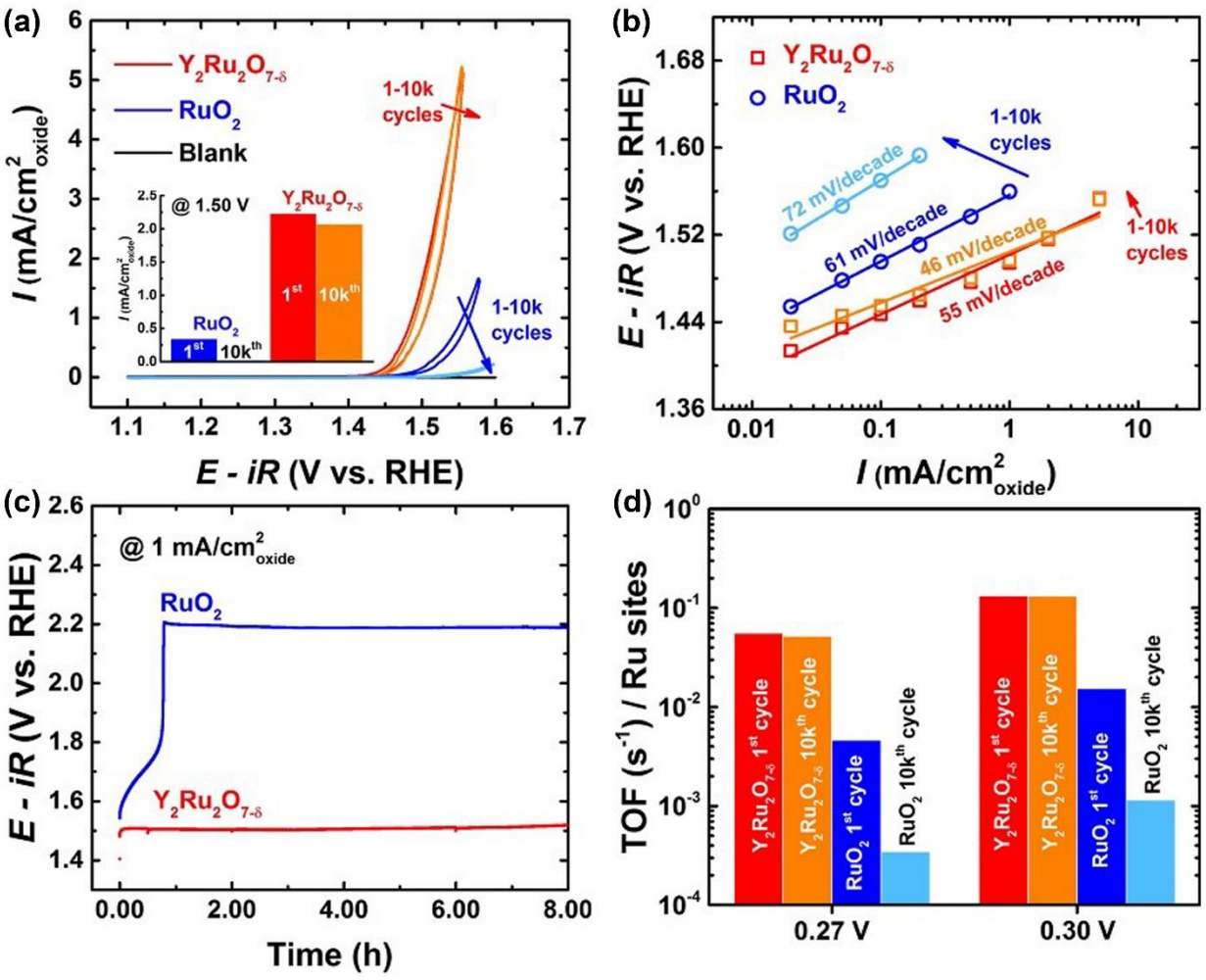

Figure 2.2 OER performance of pyrochlore $Y_2Ru_2O_{7-\delta}$ and reference RuO_2 electrocatalysts. (a) CVs for the 1st and 10,000th cycles. Inset shows the comparison of current densities for $Y_2Ru_2O_{7-\delta}$ and RuO_2 at 1.50 V versus RHE. (b) Tafel plots. The $Y_2Ru_2O_{7-\delta}$ catalyst shows enhanced activity from 55 mV/dec for the 1st cycle to 46 mV/dec for the 10,000th cycle while RuO_2 catalyst is clearly degraded from 61 mV/dec for the 1st cycle to 72 mV/dec for the 10,000th cycle. (c) Chronopotentiometry performance under constant current density of 1 mA/cm^2_{oxide} up to 8 h. (d) TOF plots showing both much higher activity and stability of $Y_2Ru_2O_{7-\delta}$ electrocatalyst than RuO_2 at different potentials under the same electrochemical test conditions.

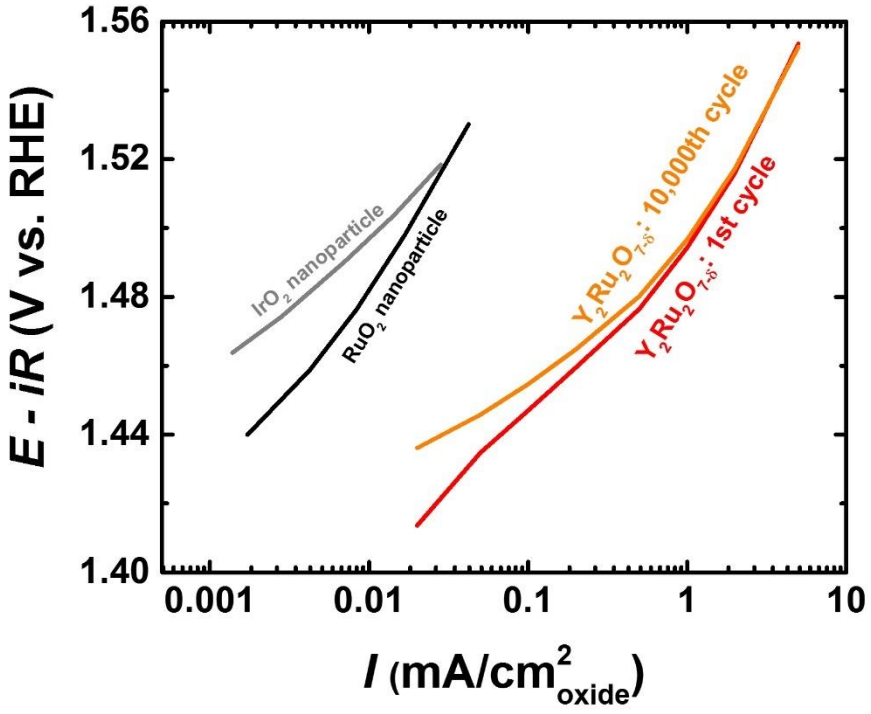

Figure 2.3 Tafel plot of $Y_2Ru_2O_{7-\delta}$, IrO_2 and RuO_2 OER catalysts. The current density of $Y_2Ru_2O_{7-\delta}$ was largely unchanged after consecutive 10,000 CV cycles tested in 0.1 M $HClO_4$ solution. The OER activity of $Y_2Ru_2O_{7-\delta}$ electrocatalyst was also significantly higher than the reported IrO_2 and RuO_2 catalysts in 0.1 M $HClO_4$ solutions.[70]

The TOF of these OER catalysts was calculated by dividing the number of oxygen molecules generated by the number of ruthenium ions under 100 % Faradaic efficiency (**Figure 2.2d**).[106] The $Y_2Ru_2O_{7-\delta}$ catalyst had the TOF value of 5.5×10^{-2} s^{-1} at the overpotential of 270 mV and remained unchanged after 10,000 cycles. The TOF of RuO_2, on the other hand, changed from $4.6\text{x}10^{-3}$ s^{-1} for the initial run to 3.4×10^{-4} s^{-1} for the 10,000th cycle, showing an order of magnitude decrease in activity. The same performance trend was observed at the overpotential of 300 mV, in

which case the TOF value remained to be 1.3×10^{-1} s^{-1} for $Y_2Ru_2O_{7-\delta}$ throughout but dropped from 1.5×10^{-2} s^{-1} for the initial cycle to 1.2×10^{-3} s^{-1} for the 10,000th cycle for RuO_2. It is noteworthy that the true TOF values were underestimated in this calculation, because all Ru atoms including a substantial portion in the bulk were treated as surface sites.[106] Thus, the difference in real TOF values should be even larger between the $Y_2Ru_2O_{7-\delta}$ and RuO_2 catalysts than those mentioned above, because $Y_2Ru_2O_{7-\delta}$ catalyst had a smaller surface area than that of RuO_2 based on the Brunauer-Emmett-Teller (BET) measurement (**Figure 2.4** and **Table 2.2**).

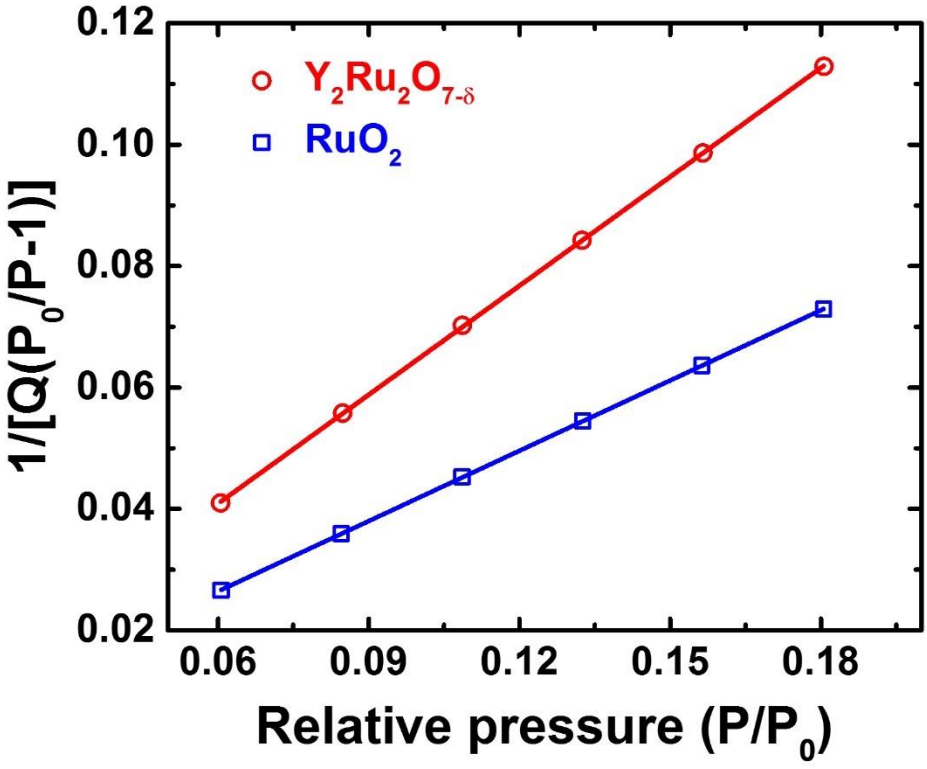

Figure 2.4 BET isotherms of $Y_2Ru_2O_{7-\delta}$ and RuO_2 catalysts. Surface areas were determined based on the relative pressure P/P_0 in the range between 0.05 and 0.18.

Table 2.2 BET isotherm analysis for $Y_2Ru_2O_{7-\delta}$ and RuO_2 catalysts

	BET surface area (m^2/g)	slope (g/cm^3)	y-intercept (g/cm^3)	BET constant	correlation coefficient
RuO_2	11.18 ± 0.02	0.3860 ± 0.0008	0.003264 ± 0.000098	119.23	0.9999920
$Y_2Ru_2O_{7-\delta}$	7.22 ± 0.02	0.5983 ± 0.0019	0.004961 ± 0.000240	121.61	0.9999802

EIS measurement was performed to understand the catalytic property during the OER. **Figure 2.5** shows the Nyquist plots at three different potential values: 0 V (no applied potential), onset potential (1.42 V for $Y_2Ru_2O_{7-\delta}$ and 1.47 V for RuO_2), and 1.50V. The corresponding equivalent electrical circuit is consisted of three components, that is, the solution resistance (R_{sol}), the charge transfer resistance (R_{ct}), and the double layer capacitance (C_{dl}), respectively. The double layer capacitance was used to reflect the catalyst surface roughness and treated as the constant phase element (CPE), which was comprised of two components of CPE-P (n, the semi-circle in the Nyquist plot) and CPE-T (Q, pseudo capacitance) (**Table 2.3**).[107] The obtained resistance was ~24-26 Ω for the solution for all the applied potential range, whereas the charge transfer resistance and the capacitance were affected greatly by the applied potentials. The obtained resistances were 7651 Ω for $Y_2Ru_2O_{7-\delta}$ and 1549 Ω for RuO_2 when no potential was applied (**Figure 2.5**). These obtained values of resistance were reversed for the catalysts. The charge transfer resistances reflect the intrinsic conductivity of these catalysts,[108,109] indicating showing $Y_2Ru_2O_{7-\delta}$ is electrically more resistive than RuO_2. When measured at their corresponding onset potentials (1.42V for $Y_2Ru_2O_{7-\delta}$ and 1.47 V for RuO_2), the resistance was greatly decreased to 114.4 Ω for $Y_2Ru_2O_{7-\delta}$ and 114.7 Ω for RuO_2 respectively (**Figure 2.5b**), showing the similarity in value between the two under the initial OER operating conditions. Slightly depressed semicircles were obtained for these

catalysts, presumably due to the charge transfer during the OER process.[107] A dramatic change in charge transfer resistance was observed at a high overpotential of 1.50 V (**Figure 2.5c**). The resistance became 10.4 Ω for the $Y_2Ru_2O_{7-\delta}$ electrocatalyst, which was much lower than that of RuO_2 (24.4 Ω). This result clearly indicates $Y_2Ru_2O_{7-\delta}$ has a faster OER kinetic rate than the RuO_2 reference catalyst.[107] The decreased CPE-P (n) values were obtained at this applied potential, likely resulting from the increased surface roughness through reacting with O_2 gas generated during the OER (**Table 2.3**).[107]

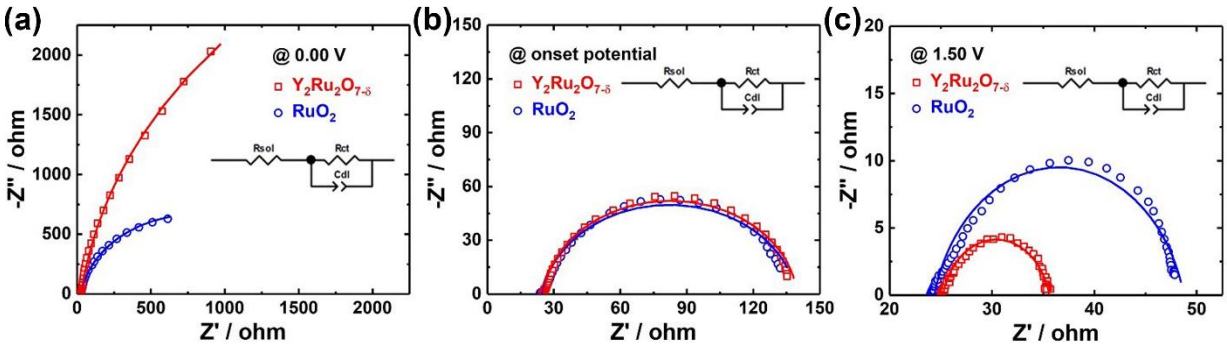

Figure 2.5 Nyquist plots of pyrochlore-type $Y_2Ru_2O_{7-\delta}$ and reference RuO_2 electrocatalysts at three different conditions: (a) no applied potential, (b) the onset potential (1.42 V for $Y_2Ru_2O_{7-\delta}$ and 1.47 V for RuO_2), and (c) 1.50 V. The obtained impedance data were fitted by using the equivalent electrical circuit model shown (solid curves).

Table 2.3 EIS analysis for $Y_2Ru_2O_{7-\delta}$ and RuO_2 catalysts

Catalysts	Potential (V versus RHE)	R_{sol} (ohm)	R_{ct} (ohm)	CPE-P, n	CPE-T, Q	Capacitance (F)
RuO_2	0.00 V	24.9	1549	9.04E-01	1.28E-03	8.85E-04
	1.47 V	24.8	114.7	9.10E-01	1.85E-03	1.36E-03
	1.50 V	24.4	24.4	8.44E-01	2.60E-03	1.56E-03
$Y_2Ru_2O_{7-\delta}$	0.00 V	26.1	7651	9.22E-01	6.15E-04	4.34E-04
	1.42 V	25.4	114.4	9.40E-01	1.09E-03	8.70E-04
	1.50 V	25.2	10.4	8.56E-01	1.46E-03	8.40E-04

*: CPE-P is the Constant Phase Element-P (n), which is related to the semicircle in the Nyquist plot, and CPE-T is the Constant Phase Element-T (Q), which is the pseudo capacitance. The capacipance is obained using the following equation:

$$Capacitance = R_{electrode}^{\left(\frac{1-n}{n}\right)} \times Q^{\frac{1}{n}} \qquad (2.4)$$

2.3.3 Structural analysis for enhanced activity

The structure of $Y_2Ru_2O_{7-\delta}$ catalyst was characterized by XAS to elucidate the atomic structures.[18] **Figure 2.6a** shows the XANES of Ru K-edge region of the pyrochlore-type $Y_2Ru_2O_{7-\delta}$. Ru metal foil and RuO_2 powder were used as the references and measured in the same way. The absorption threshold at 22120 eV for Ru foil corresponds to the heteroatomic interactions between the metal central of Ru atom on 5p orbital and the neighboring atoms on the 4d/5p orbitals.[110] The observed values of absorption threshold for RuO_2 and $Y_2Ru_2O_{7-\delta}$ were larger than that for Ru foil, indicating the increased transition energy from 1s to the outermost shell orbitals of Ru atoms. The higher energy state was associated with the empty 5d orbitals due to the formation of Ru-O bonds with strong hybridization. The two near-edge peaks were associated with the multiple back

scattering from 1s to 5p transition and the single back scattering interferences between Ru and neighboring atoms, respectively.[110] In order to evaluate the oxidation state of Ru cation in $Y_2Ru_2O_{7-\delta}$, we analyzed the absorption energy (E_0), which was obtained from the first maximum in the first-order derivative as the electron vacancy.[62,111] **Figure 2.6b** shows the absorption energy as a function of the oxidation state of the three Ru materials, where the valence state increases linearly by ~1.9 eV per oxidation state from the absorption energy of Ru foil.[111] Thus, the average Ru oxidation state of $Y_2Ru_2O_{7-\delta}$ is determined as +3.3 (**Table 2.4**). The Ru-O and Ru-Ru bonds were examined by EXAFS. **Figure 2.6c** shows the schematic illustration of electronic back scatterings between Ru and neighbor atoms of $Y_2Ru_2O_{7-\delta}$. The corresponding Fourier transformed (FT) radial structure based on the k^2-weighted EXAFS data is presented in **Figure 2.6d**. The peaks at 1.55 Å are associated with the electronic back scatterings between Ru and neighboring O in the first shell layer. The position of this peak is 1.56 Å for $Y_2Ru_2O_{7-\delta}$, in good agreement with the Ru oxidation analysis shown in **Figure 2.6b**.[76] The peaks at 2.75 Å and 3.25 Å for the RuO_2 catalyst arise from the back scatterings of Ru-Ru, and the peak at 3.25 Å of $Y_2Ru_2O_{7-\delta}$ catalyst is attributed to both Ru-Ru and Ru-Y.[101] The results indicate the Ru-O bond distance should be similar between these two catalysts.

Table 2.4 XANES spectra analysis of $Y_2Ru_2O_{7-\delta}$ and Ru references

	absorption edge (eV)	electronic structure	d vacancy (holes)	Ru oxidation state
Ru foil	22124.31	$4d^7 5s^1$ (Ru)	3	0
RuO_2	22131.42	$4d^4$ (Ru^{4+})	6	+4.0
$Y_2Ru_2O_{7-\delta}$	22130.13	$4d^{4.7}$ ($Ru^{3.3+}$)	5.3	+3.3

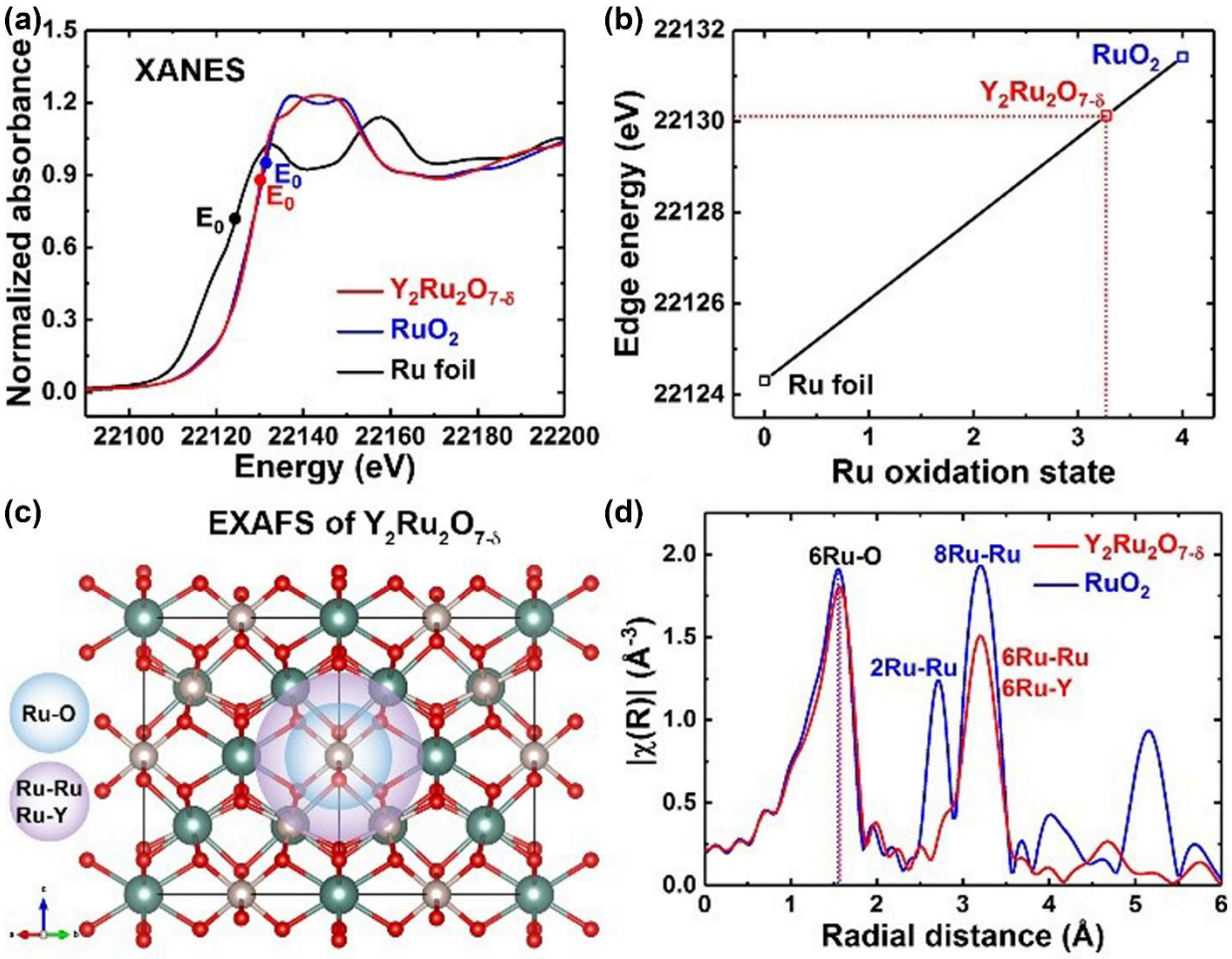

Figure 2.6 X-ray absorption spectroscopy (XAS) analysis of $Y_2Ru_2O_{7-\delta}$ electrocatalyst. (a) Normalized XANES spectra of Ru K-edge with different absorption energy (E_0) for $Y_2Ru_2O_{7-\delta}$, RuO_2 and Ru foil, respectively. (b) Relationship between Ru K-edge energy and oxidation state for $Y_2Ru_2O_{7-\delta}$ and the two reference materials. (c) Illustration of electronic back scatterings between Ru and neighbor atoms of $Y_2Ru_2O_{7-\delta}$ and (d) Fourier transformed EXAFS spectra of Ru edge for $Y_2Ru_2O_{7-\delta}$ and RuO_2 powders.

These XAS data help to understand the enhance activity performance of this pyrochlore type OER catalysts. In general, formation of Ru-O bond is directly related to OER activity, which is an important consideration in the limiting reaction involving OH species according to the four-step OER mechanism as follows[14]:

$$Ru^{4+} + 2H_2O \rightarrow Ru^{5+} - OH^* + H_2O + H^+ + e^- \quad (2.5)$$

$$Ru^{5+} - OH^* + H_2O + H^+ + e^- \rightarrow Ru^{6+} - O^* + H_2O + 2H^+ + 2e^- \quad (2.6)$$

$$Ru^{6+} - O^* + H_2O + 2H^+ + 2e^- \rightarrow Ru^{5+} - HOO^* + 3H^+ + 3e^- \quad (2.7)$$

$$Ru^{5+} - HOO^* + 3H^+ + 3e^- \rightarrow Ru^{4+} + O_2 + 4H^+ + 4e^- \quad (2.8)$$

where the * represents an active site of the $Y_2Ru_2O_7$ catalyst. In this mechanism, the chemically adsorbed water molecules dissociate into OH* and H^+ on the active Ru^{4+} site, while Ru^{4+} is simultaneously oxidized into Ru^{5+} (eq. 2.5). The OH* then dissociates into O* and H^+ while Ru^{5+} is oxidized further into Ru^{6+}. The rate determining step (RDS, eq. 2.7) involves the combination of O* with water molecule to form HOO* and Ru^{6+} is reduced to Ru^{5+}. Finally, O_2 forms from the peroxide species, while Ru^{5+} is reduced to Ru^{4+}. In the RDS, binding of HOO* species to the active site is most critical, because it has the highest Gibbs energy. The low oxidation state of Ru cations could lead to high activity similar to Ir cations.[76] The pyrochlore-type $Y_2Ru_2O_{7-\delta}$ compound has a lower valence state of Ru (+3.3) than RuO_2, which is beneficial to the enhanced activity. Since the limiting step involved more than one kind of Ru active sites with absorbed oxygen and water (Ru-O* and Ru-H_2O*),[12] the Ru-Ru bond length and strength should be direct relevant to the catalytic activity. Our EXAFS data indeed show a large difference in Ru-Ru bond between $Y_2Ru_2O_{7-\delta}$ pyrochlore and RuO_2, which is another structural factor for the difference in performance.

2.3.4 Experimental and first principle studies of OER stability

High resolution transmission electron microscopy (HRTEM) and PXRD were carried out to examine the structures of $Y_2Ru_2O_{7-\delta}$ and RuO_2 catalysts before and after the OER tests (**Figure 2.7**). After the potential cycles, PXRD patterns showed no detectable changes in peak position or width for the $Y_2Ru_2O_{7-\delta}$ electrocatalyst (**Figure 2.7a**). HRTEM and the corresponding fast Fourier transformation (FFT) images confirm that the surface structure of $Y_2Ru_2O_{7-\delta}$ catalyst was maintained throughout the particle (**Figure 2.7b**, **Figure 2.8**). For the RuO_2 reference catalyst, while the PXRD pattern showed no obvious changes (**Figure 2.7c**), HRTEM study shows that an amorphous top layer of less than 2 nm appeared after the tests, while the core still possessed the lattices that can be assigned to the *P42/mnm* tetragonal phase (**Figure 2.7d**). The results show that the surface of RuO_2 catalyst turned into amorphous structures. The crystalline structure of $Y_2Ru_2O_{7-\delta}$, on the other hand, ensured a stable surface, thus the catalytic stability.[76,112] Experimentally, ICP-MS was carried out to examine quantitatively the stability of $Y_2Ru_2O_{7-\delta}$ electrocatalyst under acid conditions. The ICP-MS results show the amount of Ru dissolved was below 4% in the acidic electrolyte solution after 10,000 potential cycles (**Table 2.5**).

Table 2.5 ICP-MS analysis of dissolved Ru ion after 10,000 CV cycles in $HClO_4$ solution

Sample amount of $Y_2Ru_2O_{7-\delta}$ (μg)	25	25	50
Concentration for Ru ion (ppb)	0.96	1.18	2.55
Loss of mass (%)	2.79	3.45	3.75
Average mass loss with standard deviation (%)		3.33 (± 0.49) %	

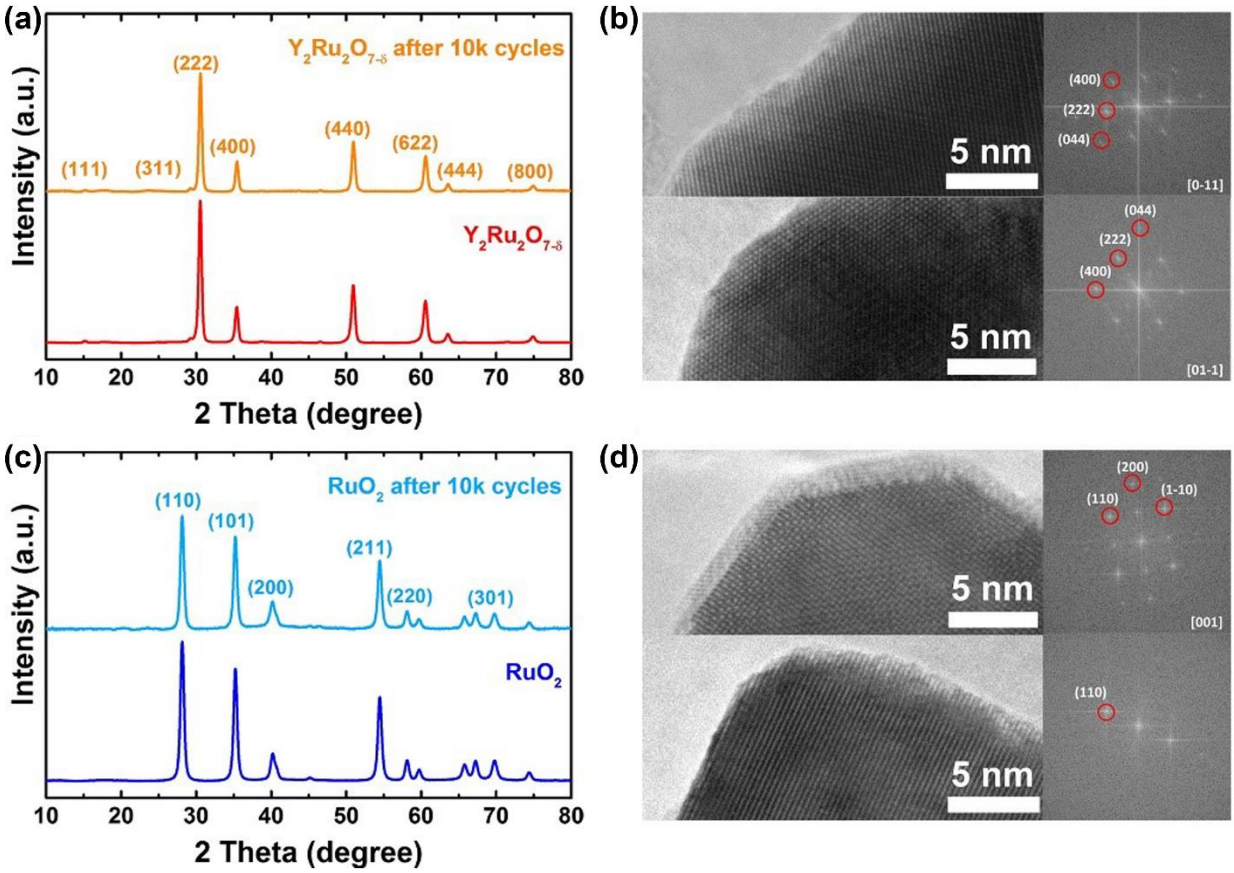

Figure 2.7 Structure analysis of bulk and near-surface regions of (a-b) $Y_2Ru_2O_{7-\delta}$ and (c-d) RuO_2 electrocatalysts before and after the OER tests. (a, c) PXRD patterns for both electrocatalysts, showing no obvious changes. (b, d) HRTEM micrographs (left) and FFT images of near-surface region (right), showing the crystalline surface structure of $Y_2Ru_2O_{7-\delta}$ while amorphous surface layer formed on RuO_2 catalysts after the cycle tests. The as-made catalysts were presented at the bottom and the catalysts after test were at the top.

XPS was performed to assess the surface composition of $Y_2Ru_2O_{7-\delta}$ electrocatalyst before and after the potential cycle tests (**Figure 2.8**). **Figure 2.8a** shows the XPS spectra of Y 3d and Ru 3d of the as-made $Y_2Ru_2O_{7-\delta}$ catalyst. The Y 3d peaks can be fit with two sets of doublets, with the primary peaks centered at 158.5 and 156.4 eV that resemble those of Y $3d_{3/2}$ and $3d_{5/2}$ of Y_2O_3, respectively.[113] A secondary doublet peak centered at 159.9 eV and 157.8 eV was observed. For Ru 3d spectra, two sets of doublet peaks were observed between 280 eV and 290 eV,[113-115] which correspond to well-screened and unscreened Ru^{4+} components.[115,116] The primary peaks at 286.0 and 281.8 eV are from Ru $3d_{3/2}$ and $3d_{5/2}$, respectively, and the satellite peaks are at 287.9 and 283.7 eV. **Figure 2.8b** shows the XPS spectra of the $Y_2Ru_2O_{7-\delta}$ electrocatalyst after potential cycle measurements. Two sets of doublets for Y 3d peaks remained unchanged in both position and shape. No change was observed for signals from the Ru species either, though the signals from carbon support changed, resulting in the difference of overall curve shape. Additional XPS spectra for survey scan and O 1s regions are shown in **Figure 2.9**. The XPS data, together with the XAS and PXRD results, further indicate the structural stability of $Y_2Ru_2O_{7-\delta}$ under acidic operation conditions.

Table 2.6 XPS data analysis of $Y_2Ru_2O_{7-\delta}$ catalysts before and after the stability tests.

	peak position(eV)	FWHM (eV)	peak position(eV)	FWHM (eV)
	$Y_2Ru_2O_{7-\delta}$ before CV		$Y_2Ru_2O_{7-\delta}$ after 10,000 CV	
Ru $3d_{5/2}$ primary	281.8	2.1	281.5	2
Ru $3d_{5/2}$ satellite	283.7	2.8	283.6	2.8
Y $3d_{5/2}$ primary	156.4	1.5	156.3	1.5
Y $3d_{5/2}$ secondary	157.8	2	158.0	1.6
C 1s	284.6	1.1	284.6	1.7

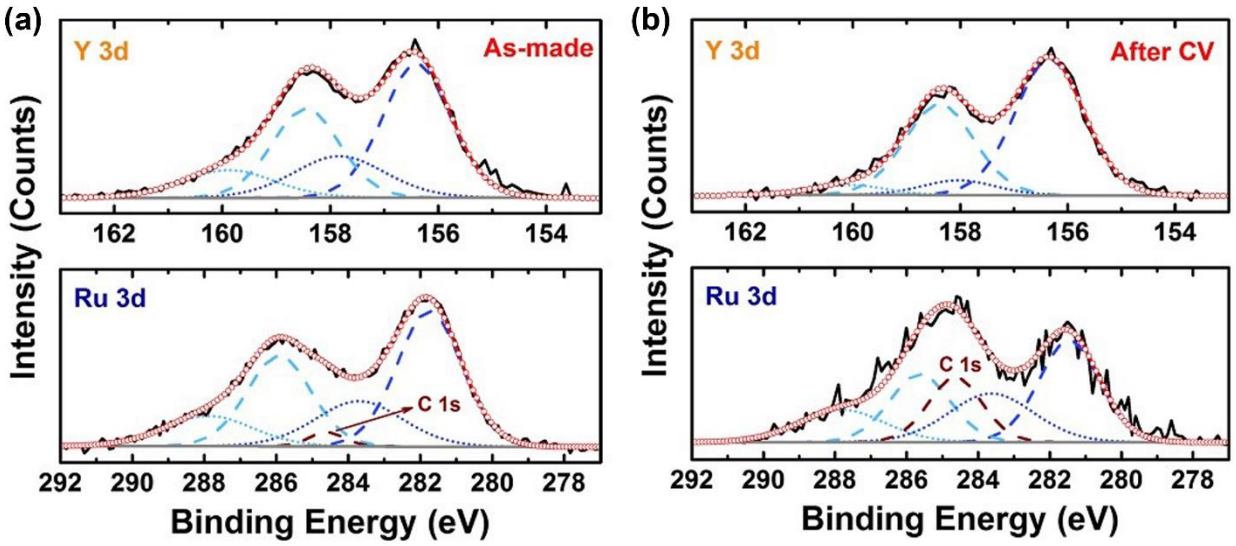

Figure 2.8 XPS of $Y_2Ru_2O_{7-\delta}$ for Y 3d (top) and Ru 3d (bottom) regions (a) before and (b) after the cycle tests. Black lines are the measured XPS spectra and the red circle lines are the fitting results from the accumulated peaks. Two sets of doublets are indicated by line style, dashed line for the primary peaks and dotted line for secondary peaks. Color codes are used for indication of different spin-orbit components, blue for 5/2 spin states and sky blue for 3/2 spin states (Blue dashed lines are the primary Ru $3d_{5/2}$ and Y $3d_{5/2}$ peaks, sky blue dashed lines are the primary Ru $3d_{3/2}$ and Y $3d_{3/2}$ peaks, blue dotted lines are the secondary Ru $3d_{5/2}$ and Y $3d_{5/2}$ peaks, and sky blue dotted lines are the secondary Ru $3d_{3/2}$ and Y $3d_{3/2}$ peaks.). Brown dashed lines are C 1s peaks.

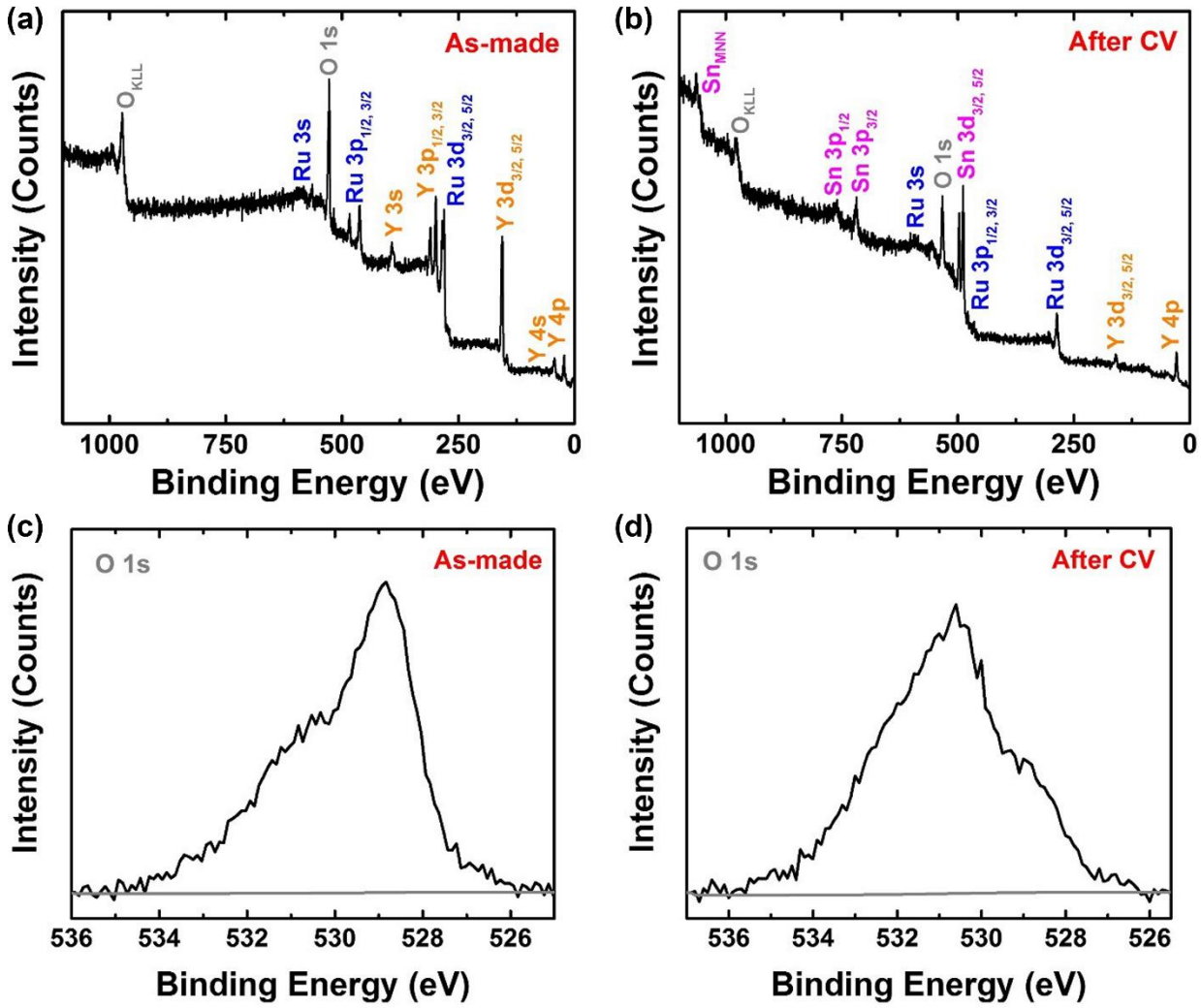

Figure 2.9 XPS spectra of pyrochlore-type $Y_2Ru_2O_{7-\delta}$. (a-b) Survey and (c-d) O 1s region scans recorded (a, c) before and (b, d) after 10,000 CV tests. For O 1s in (d), the peak at 530.5 eV was from the SnO_2 substrate.[117]

Yttrium cation appears to have a positive effect on the stability of pyrochlore-type $Y_2Ru_2O_{7-\delta}$ electrocatalyst. **Figure 2.10** shows the local structures and band center energy analysis of the pyrochlore-type $Y_2Ru_2O_{7-\delta}$ and reference RuO_2 catalysts. While the bond length of Ru-O in these two catalysts is similar, the Ru 4d-orbitial energy levels of $Y_2Ru_2O_{7-\delta}$, however, are quite

different from those of RuO_2 due to the different Ru local structures between the two (**Figure 2.10a, b**). According to the ligand field theory, the RuO_6 subunit of $A_2Ru_2O_7$ pyrochlore structure has a trigonal antiprism (D_{3d} symmetry) with split t_{2g} orbitals in the octahedral symmetry,[109] while RuO_2 has D_{2h} symmetry with split d-orbitals due to John-Teller effect.[118]

DFT was used to examine the effect of electronic band structures of Ru-O on OER performance by calculating the partial electron density of states (PDOS) for Ru and O atoms.[119] **Figure 2.10c-d** show the PDOS of $Y_2Ru_2O_6O'$ and RuO_2 for Ru 4d orbital and O 2p orbital in the RuO_6 unit, and the overlapped orbital band center between O 2p orbital and Ru 4d orbital, respectively. The electronic band structures are quite different in these two catalysts because of the crystal structure. The calculated value on band center energy for the overlapped orbitals between O 2p and Ru 4d bands, could be related to the changes in overpotential observed experimentally before and after the cycle tests. Structurally, the band center energy between O 2p and Ru 4d orbitals of $Y_2Ru_2O_6O'$ is further away from the Fermi level, which could contribute to the increased catalytic stability similar to O 2p band center,[40] suggesting that yttrium cation (Y^{3+}) should stabilize ruthenium oxide in the form of a ternary oxide because of the favored energy level in the pyrochlore structure.[72]

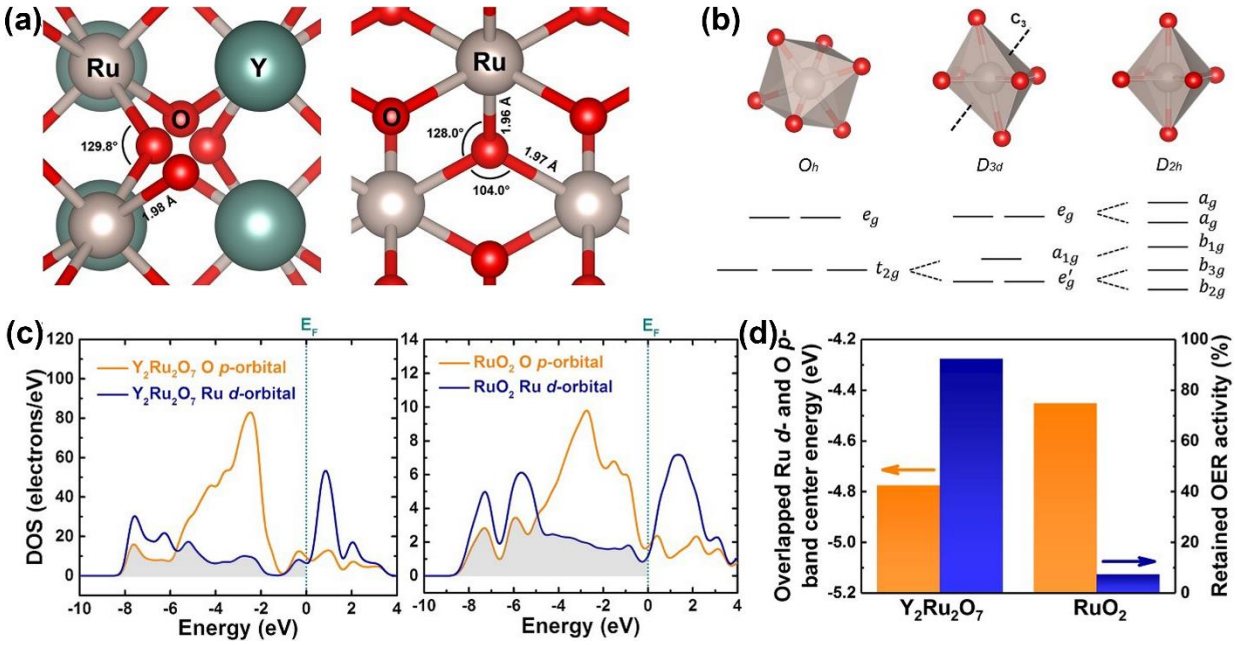

Figure 2.10 DFT calculation of energy states of $Y_2Ru_2O_7$ and RuO_2. (a) Local structures showing the Ru-O bond lengths of $Y_2Ru_2O_7$ and RuO_2, respectively. (b) Illustrations of distorted RuO_6 structures, and 4d orbital splits in octahedral (O_h), trigonal antiprism (D_{3d}), and compressed octahedral (D_{2h}) ligand fields. (c) Calculated PDOS plots of Ru 4d and O 2p orbitals for $Y_2Ru_2O_7$ and RuO_2. Shaded area shows the overlapped bands between Ru 4d and O 2p orbitals. The Fermi level is set to zero. (d) Comparison of overlapped band center energy of Ru 4d and O 2p orbital, and activity loss of current density at 1.50 V for $Y_2Ru_2O_7$ and RuO_2, respectively.

2.3.5 Porous $Y_2[Ru_{1.6}Y_{0.4}]O_{7-\delta}$ pyrochlore oxide

Porous $Y_2[Ru_{1.6}Y_{0.4}]O_{7-\delta}$ pyrochlore oxide was prepared by a two-step procedure. We used a sol-gel synthetic method, which described in detail before, with citric acid as the chelating agent to cross-link Y and Ru cations homogeneously. A perchloric acid solution (70 %) was added to the above precursor solution and used as the porogen. This mixture was cured at 80 °C until water evaporated. The dried powder was placed in a quartz boat and transferred to a tube furnace. Upon

heating, perchloric acid decomposed rapidly at *ca*. 120 °C, resulting in the formation of porous framework of the compound through linking the granular nanoparticles when the reaction temperature ramped up to 600 °C. The final product of porous $Y_2[Ru_{1.6}Y_{0.4}]O_{7-\delta}$ pyrochlore oxide was made at 960 °C.

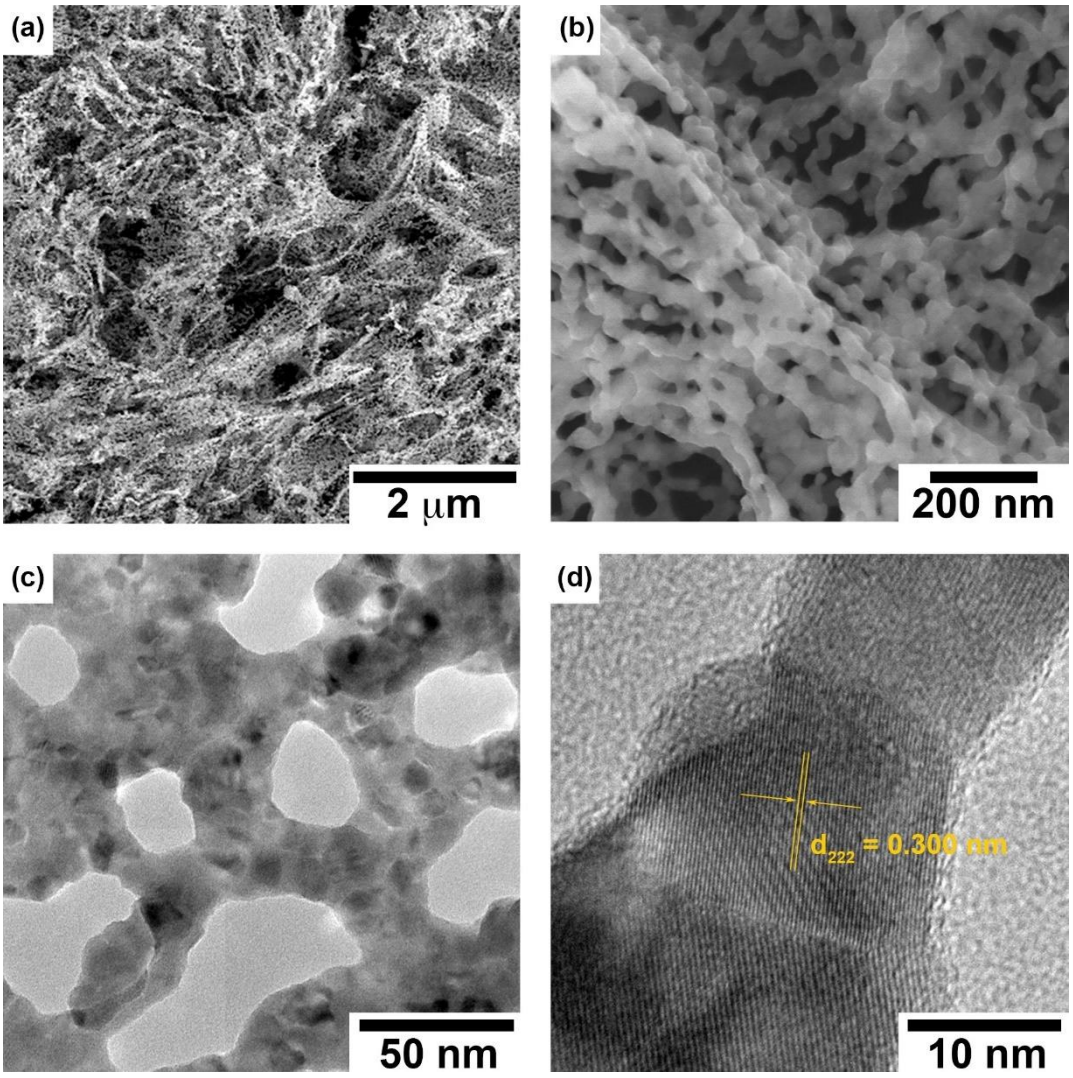

Figure 2.11 (a, b) SEM images and (c, d) TEM micrographs of porous $Y_2[Ru_{1.6}Y_{0.4}]O_{7-\delta}$ pyrochlores, showing (a) the porous structures, (b, c) meso- and macro-porous network, and (d) high crystalline of the porous wall.

SEM and TEM were used to examine the morphology of $Y_2[Ru_{1.6}Y_{0.4}]O_{7-\delta}$ pyrochlore oxide (**Figure 2.11**). SEM images and TEM micrographs show the obtained $Y_2[Ru_{1.6}Y_{0.4}]O_{7-\delta}$ pyrochlore powders had primary particles in the size range of 10 nm. These primary nanoparticles sintered and interconnected with each other to form a framework with both mesopores (2-50 nm) and macropores (> 50 nm). The average pore size was determined to be around 40 nm based on the SEM study. The surface area of this porous pyrochlore was measured to be 33.3 m^2g^{-1} for this porous pyrochlore determined by using the nitrogen isotherm technique based on BET method.

While $Y_2Ru_2O_{7-\delta}$ electrocatalysts shows an enhanced OER performance compared to RuO_2, the significant improvement was found for the porous, B-site mixed $Y_2[Ru_{1.6}Y_{0.4}]O_{7-\delta}$ pyrochlore. We calculated the turnover frequencies (TOFs) of these catalysts to investigate the formation rate of oxygen molecules on the catalytic sites (inset in **Figure 2.12a**). The porous $Y_2[Ru_{1.6}Y_{0.4}]O_{7-\delta}$ pyrochlore has the highest TOF of 560 s^{-1} at 1.5 V, whereas the TOF is 67.7 s^{-1} for $Y_2Ru_2O_{7-\delta}$, and 5.41 s^{-1} for RuO_2. The porous $Y_2[Ru_{1.6}Y_{0.4}]O_{7-\delta}$ pyrochlore not only has the highest TOF, but also is two orders of magnitude in activity of RuO_2, one of the best-known binary oxide OER catalyst in acid. The associated OER kinetics of these electrocatalysts were further studied using the Tafel plots of mass activity (**Figure 2.12b**). The Tafel slope of porous $Y_2[Ru_{1.6}Y_{0.4}]O_{7-\delta}$ pyrochlore was measured to be 37 mV/dec, showing the lowest value among the catalysts. In comparison, the Tafel slope was measured to be 46 mV/dec for $Y_2Ru_2O_{7-\delta}$ and 60 mV/dec for RuO_2. These results suggest that superior OER activity of the porous $Y_2[Ru_{1.6}Y_{0.4}]O_{7-\delta}$ electrocatalysts comes from not only the high surface area, but also the favored energy band structure because of the oxygen-deficient pyrochlore structure.[27] To be specific, with Y^{3+} substitution, the multivalent states of Ru cations (Ru^{4+} and Ru^{5+}) lower the band energy. This reduction in band energy strengthens the covalent bond between Ru 4d-band and the new O 2p-band due to the lattice oxygen defects. The change

in covalency can substantially affect the OER performance, as shown in the cases of $La_{1-x}Sr_xCo^{3+}{}_{1-y}Co^{4+}{}_yO_{3-\delta}$ and $LaCoO_{3-\delta}$ catalysts.[27,120] The lattice-oxygen mediated mechanism (LOM) model explains qualitatively the performance trend of the porous $Y_2[Ru_{1.6}Y_{0.4}]O_{7-\delta}$ pyrochlore catalysts.[27]

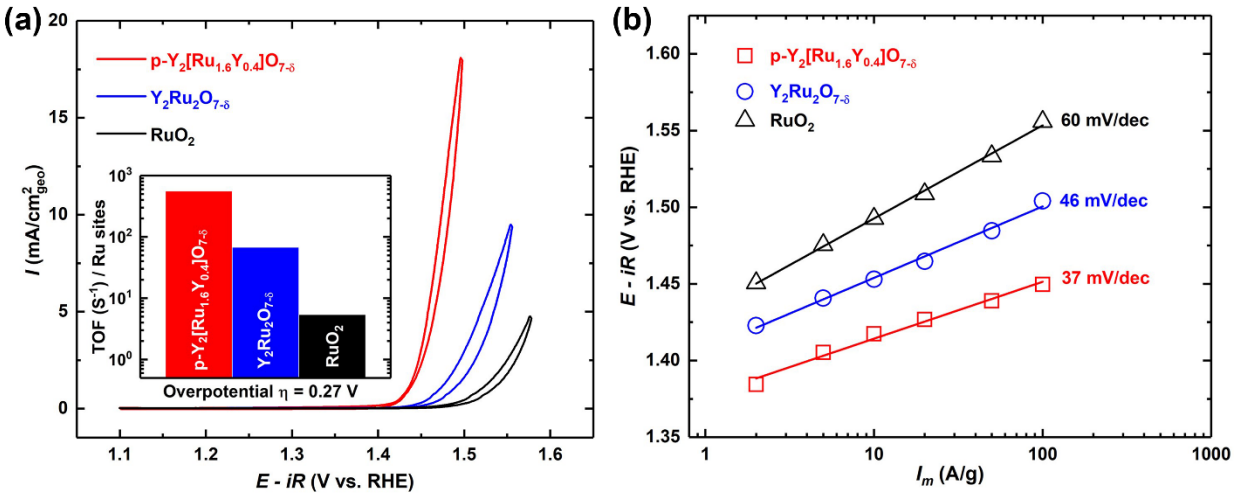

Figure 2.12 OER performance comparison of porous $Y_2[Ru_{1.6}Y_{0.4}]O_{7-\delta}$, $Y_2Ru_2O_{7-\delta}$, and RuO_2 electrocatalysts. (a) CVs and the corresponding TOFs (inset), and (b) Tafel plots of mass activity. All the measurements were carried out three times independently.

2.4 Conclusions

We have developed a pyrochlore-type $Y_2Ru_2O_{7-\delta}$ electrocatalyst that possesses excellent OER activity and stability in acid media. Our experimental data and DFT computational analysis indicate that the long-term activity of Ru-based oxide catalysts is related to the surface structure and valency of Ru in $Y_2Ru_2O_{7-\delta}$ pyrochlore lattice,[112] and the lowered overlapped energy band center between O 2p and Ru 4d orbitals. An altered synthetic strategy with perchloric acid as the porogen enabled successful synthesis of a porous, phase-pure $Y_2[Ru_{1.6}Y_{0.4}]O_{7-\delta}$ pyrochlore oxide.

This porous $Y_2[Ru_{1.6}Y_{0.4}]O_{7-\delta}$ electrocatalyst further enhanced the OER activity compare to $Y_2Ru_2O_{7-\delta}$. The superior activity results from both high surface area of the porous structures and the optimized energy band structure due to the oxygen lattice defects, which arise from the mixed oxidation state of $Ru^{4+/5+}$ due to the partial substitution by Y^{3+} on the B-site. These findings point to a new way to design highly active and acid-stable, Ir-free, OER catalysts that can potentially be readily scalable in production.

CHAPTER 3

FINE PYROCHLORE $Y_2Ru_2O_{7-\delta}$ NANOPARTICLES MADE BY LOW TEMPERATURE POLYMERIC ENTRAPMENT FOR OXYGEN EVOLUTION REACTION

3.1 Introduction

Due to the highly oxidative operative condition of acidic OER, Ru and Ir, are inevitable in a catalyst design. As a result, maximizing the utilization of these active materials is crucial for an efficient catalyst. Synthesis and design of nanostructures are often used as a strategy to optimize the catalysts in this regard. Applying this theory to pyrochlore-type catalysts remains challenging because the synthesis of pyrochlore phases usually require high temperature heating processes (> 900 °C), resulting in extensive particle sintering and reducing the active surface area.

Receiving inspiration from new ceramic materials, polymeric entrapment has received attention for the synthesis of ternary metal oxide nanoparticles, e.g. $LiMnO_2$ and $LiFePO_4$ prepared this way can be used as cathode materials for Li ion batteries.[121,122] In this technique, long-chain polymers separate metal ions into a homogeneous network and inhibit segregation within the precursor solution. This design reduces the diffusion of metal ions and decreases the formation energy of specific complex oxide structures. Therefore, polymeric entrapment can yield a low temperature synthesis of pyrochlore type materials.

In this chapter, I will present a new synthetic strategy of making high surface area pyrochlore $Y_2Ru_2O_{7-\delta}$ using polymeric entrapment method (PEM). Surprisingly, the formation of phase-pure pyrochlore ceramic/ternary oxide nanoparticle could be realized at a low temperature of 550 °C. The as-made $Y_2Ru_2O_{7-\delta}$ (noted as pem-550 °C) by polymeric entrapment method is characterized and compared with previously presented (Chapter 2) $Y_2Ru_2O_{7-\delta}$ made from sol-gel

precursors at a high temperature of 1000 °C (sol gel-1000 °C). X-ray diffractometer (XRD), energy-dispersive X-ray spectroscopy (EDS), X-ray absorption near-edge structure (XANES) spectra and extended X-ray absorption fine structure (EXAFS) spectra analysis show that polymeric entrapment synthesis can effectively synthesize phase pure $Y_2Ru_2O_{7-\delta}$ pyrochlore phase material. Scanning electron microscopy (SEM) and transmission electron microscopy (TEM) analysis show the pem-550 °C has high surface area with highly crystallized nanoparticles. The OER activity study shows the pem-550 °C has superior OER activity due to high surface area while remain stable for 24 h OER durability test.

3.2 Experimental procedures

3.2.1 Material synthesis

Polymeric entrapment method (PEM) was used in the preparation of $Y_2Ru_2O_{7-\delta}$ with small particle size. 20 wt% of polyvinyl alcohol (PVA, Mw = 9,000 ~ 10,000, Sigma-Aldrich) was prepared by dissolving 0.01196 g PVA in 10 mL de-ionized water (DIW, 18.2 MΩ-cm resistivity) and stirred for 3 h. Stoichiometric amounts of 0.1915 g yttrium nitrate ($Y(NO_3)_3{\cdot}6H_2O$, 99.9%, Alfa Aesar) and 3.087 mL ruthenium nitrosyl nitrate ($Ru(NO)(NO_3)_x(OH)_y$, Sigma-Aldrich) were dissolved in 10 mL of DIW and stirred for 5 min. Follow by addition of the previously prepared PVA solution, 1 mL of nitric acid (70 %) and continuous stirring for another 1 h. The solution is transferred to an oil bath at 70 ºC and cured for 5 h. After that, the solution was allowed for natural evaporation overnight and vacuumed for 6 h to remove all moisture completely. After drying, the gel was placed on a hot plate at 300 ºC for 2 h, where the gel color changed from brownish to dark gray. The powder was collected and placed in combustion boat, flash pyrolyzed at 550 ºC for 6 h (in a pre-heated tube furnace) to form the final pyrochlore phase. For study of different PVA to

metal ions ratio, the Y and Ru precursors amount were fixed. Coherent amount of PVA was calculated and prepared at 20 wt% in first step for the synthesis. Different synthetic temperature studies were carried with all same procedures until the final annealing step. If not flash pyrolysis, 5 ºC/min ramping rate was used without pre-heating furnace. For flash pyrolysis, the furnace was pre-heat to the desired temperature in a 50 ºC/min rate. Once the temperature was stabilized, the combustion boat was placed inside the furnace with quartz tube immediately to reduce temperature fluctuation. All synthesis was cooled down to room temperature naturally.

3.2.2 Material characterization

The crystal phases were analyzed by XRD (Rigaku Miniflex 600) with Cu X-ray source. The measurement was performed in the scan range between 10° and 80° 2θ. HRTEM images were taken with JEOL 2100 Cryo TEM at an acceleration voltage of 200 kV. TEM specimen was prepared by dispersing a suspension in ethanol on a carbon-coated copper grid. SEM images were obtained with a Hitachi S4700 SEM at an acceleration voltage of 10 kV. EDS was collected with same the SEM at a voltage of 20 kV. SEM specimen was prepared by directly depositing material powders on carbon tape and a SEM stub.

Nitrogen isotherm and Brunnauer-Emmett-Teller (BET) analysis was performed using Micromeritics Gemini VII 2390 and 3Flex Physisorption system. The BET surface area of the materials was obtained with 6-point measurement in the P/P_0 range between 0.05 and 0.30 under an N_2 adsorption environment.

X-ray absorption spectroscopy (XAS) was performed in transmission mode at Beamline 20-BM-B at the Advanced Photon Source (APS), Argonne National Laboratory, USA. The obtained XAS spectra was analyzed by Artemis and Athena software.

3.2.3 Electrochemical study

A catalyst ink was prepared for electrode preparation. 0.5 mL of 0.1 M NaOH solution was added to 0.5 mL of Nafion 117 aqueous solution (5%, Sigma-Aldrich) to make a neutralized Nafion solution, of which the pH value was about 8. Two milligrams of pyrochlore oxide catalyst, 2 mg of carbon black (Vulcan XC-72), and 3 µL of neutralized Nafion solution were added in 2 mL of tetrahydrofuran (THF) in 15 mL vial, followed by sonication for 30 min in an ice bath. A rotating glassy-carbon disk electrode (RDE) was polished with 0.05 µm alumina slurry until a mirror surface was obtained. 5 µL of the prepared ink solution was drop-casted on the RDE. After the ink dried, 10 µL of Nafion-THF solution (3 µL of neuralized Nafion solution in 2 mL of THF) was drop-casted on top of the disk surface to form a thin film electrode.

Experiments were performed using a three-electrode system with a CHI 760D potentiostat (CH Instruments, Inc.). A platinum wire (diameter: 0.5 mm) connected with platinum foil (area: 1 cm^2) was used as the counter electrode, and a hydrogen electrode (HydroFlex, Gaskatel) was used as the reference electrode. The reference electrode was calibrated in H_2-saturated (Airgas, Inc., 99.999%) 0.1 M $HClO_4$ (Veritas double distilled, 70%) electrolyte solution, where cyclic voltammetry (CV) scans were carried out at a scan rate of 100 mV s^{-1} for 100 s and the average value of the two potentials at which the H_2 oxidation/evolution curves crossed at I = 0 A was treated as the thermodynamic potential for the hydrogen reference electrode (RHE). Oxygen evolution reaction (OER) measurements were performed three times after purging with O_2 (Airgas,

Inc., 99.999%) for at least 30 min. CV curves were collected at a scan rate of 10 mV s^{-1} in a potential range between 1.1 and 1.6 V versus RHE. The RDE rotating speed was fixed at 1,600 rpm. The resistance of the system was measured to be 24-29 Ω, and these values were used for correcting the ohmic resistance. The capacitance was corrected by taking the average value of anodic and cathodic scans to evaluate the electrochemical performance.

3.3 Results and discussion

3.3.1 Synthesis of by $Y_2Ru_2O_{7-\delta}$ polymeric entrapment

Phase pure $Y_2Ru_2O_{7-\delta}$ nanocrystalline was prepared by polymeric entrapment method synthesis with PVA (Mw = 9,000 ~ 10,000) as the steric entrapment polymer (**Figure 3.1**). To ensure well mixing of PVA and metal precursors in water, a 20 wt% PVA in DIW solution was prepared prior to the synthesis. The amount of PVA solution added was calculated based on the total (+) valence of the cations and (–) valence of the functional groups in PVA. A ratio of 1:12 (+) to (–) was used to synthesize phase pure $Y_2Ru_2O_{7-\delta}$. After drying, the material was heated with two separate steps. First heated at 200 ºC (on a hot plate set temperature of 300 ºC) to form an ionic network. The dark grey colored material was collected and follow for a second step flash pyrolysis treatment at 550 ºC to form the $Y_2Ru_2O_{7-\delta}$ pyrochlore nanocrystalline.

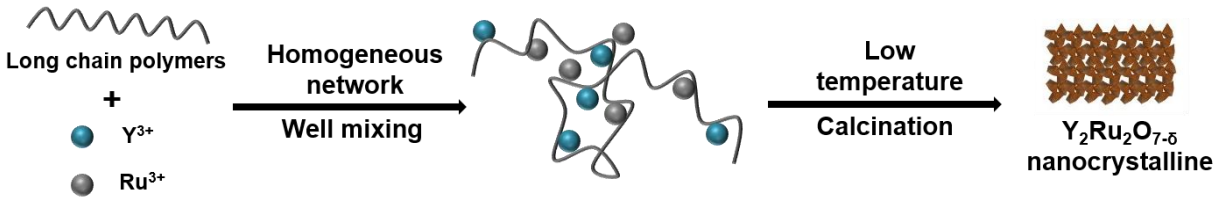

Figure 3.1 The polymeric entrapment synthetic procedures of making $Y_2Ru_2O_{7-\delta}$ nanocrystalline.

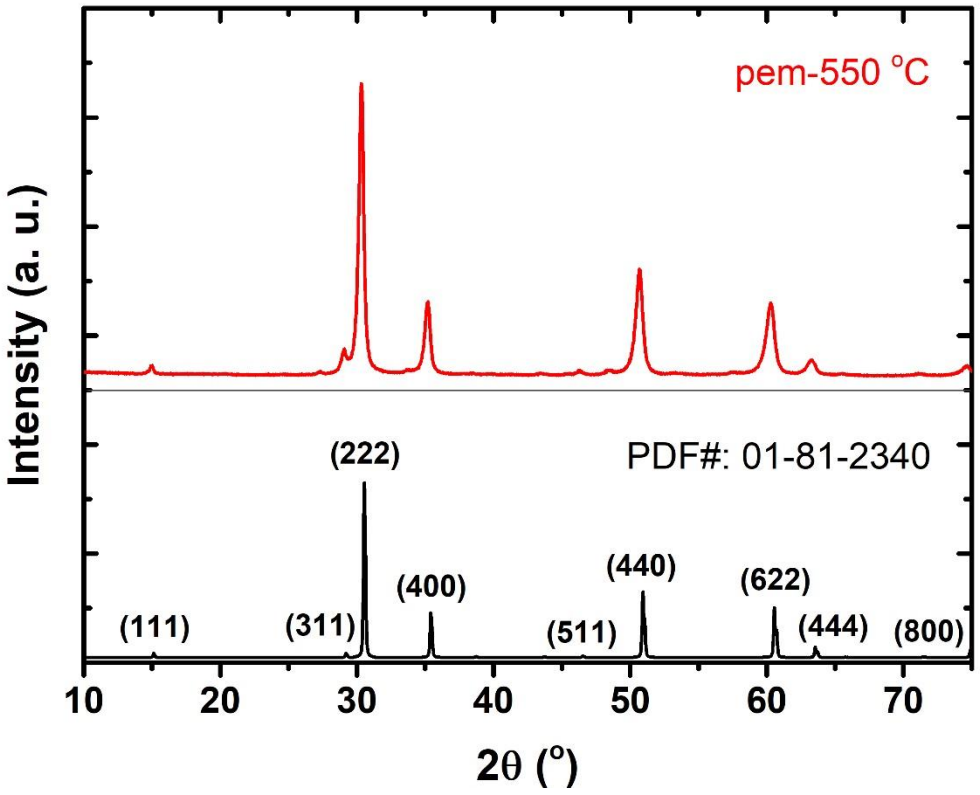

Figure 3.2 XRD patterns of polymeric entrapment method synthesized $Y_2Ru_2O_{7-\delta}$ (pem-YRO) at 550 °C. All peaks can be assigned to cubic phase (Fd-3m) $Y_2Ru_2O_7$, indicating phase pure material that had been synthesized.

Figure 3.2 shows the XRD patterns of $Y_2Ru_2O_{7-\delta}$ (YRO) synthesized by PEM at 550 ºC (pem-550 ºC). All peaks can be assigned to cubic phase pyrochlore oxide with Fd-3m symmetry (JCPDS 01-81-2340) and no impurity peaks are identified. The composition of $Y_2Ru_2O_{7-\delta}$ is further confirmed by EDS analysis of metal ion ratios (**Figure 3.3**) which shows a roughly 1:1 Y to Ru ratio. Neither replacement nor mixture of A-, B-site ions in the pyrochlore structure ($A_2B_2O_{7-\delta}$), which is the case in porous $Y_2[Ru_{1.6}Y_{0.4}]O_{7-\delta}$ pyrochlore shown in Chapter 2, is observed.

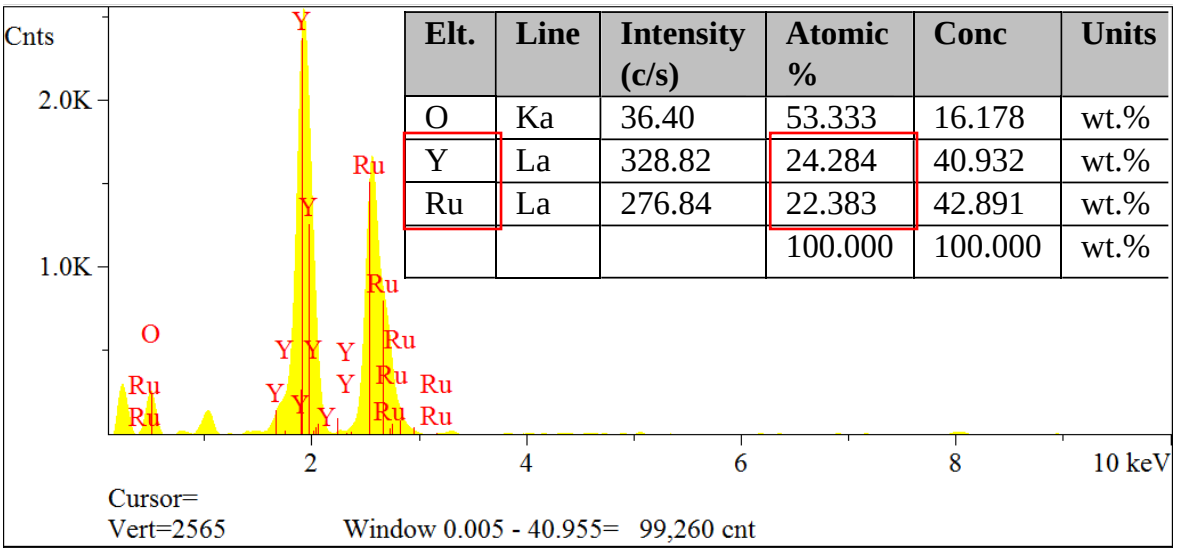

Elt.	Line	Intensity (c/s)	Atomic %	Conc	Units
O	Ka	36.40	53.333	16.178	wt.%
Y	La	328.82	24.284	40.932	wt.%
Ru	La	276.84	22.383	42.891	wt.%
			100.000	100.000	wt.%

Figure 3.3 EDX analysis of pem-YRO at 550 °C. Y to Ru ratio is roughly 1 to 1, showing no B-site migration happened with the synthesis process.

Figure 3.4a shows the scanning electron microscope (SEM) images of pem-550 °C material. The inset shows a magnified SEM image. The granular particle size is around 10 ~ 50 nm with limited sintering across the sample. The high-resolution transmission electron microscopy (TEM) image (**Figure 3.4b**) shows each individual grain are highly crystallized particles throughout. The d-spacing of the lattice is 2.99 Å which is calculated from 20 fringes. The lattice spacing is corresponding to (222) plane from XRD pattern (2.94 Å). **Figure 3.5** shows Brunauer-Emmett-Teller (BET) nitrogen isotherm for pem-550 °C sample. The surface area is determined to be 14.8 m^2/g which is more than double of the $Y_2Ru_2O_{7-\delta}$ synthesized by sol-gel method (7.2 m^2/g). The result aligns well with the material particle sizes observed in the SEM images, as the SEM image of sol-gel synthesized $Y_2Ru_2O_{7-\delta}$ (shown in Chapter 2) shows the particle size is roughly > 100 nm.

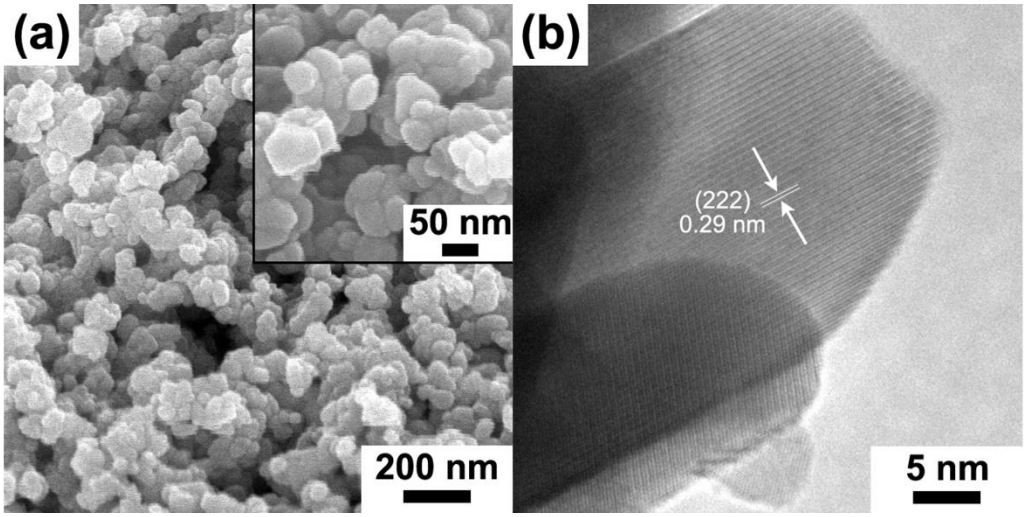

Figure 3.4 Microscopic images of $Y_2Ru_2O_{7-\delta}$ synthesized at 550 °C. (a) SEM image of pem-550 °C. Inset shows a magnified image and the grain size of particles. (b) TEM image of pem-550 °C shows highly crystallized nanoparticles.

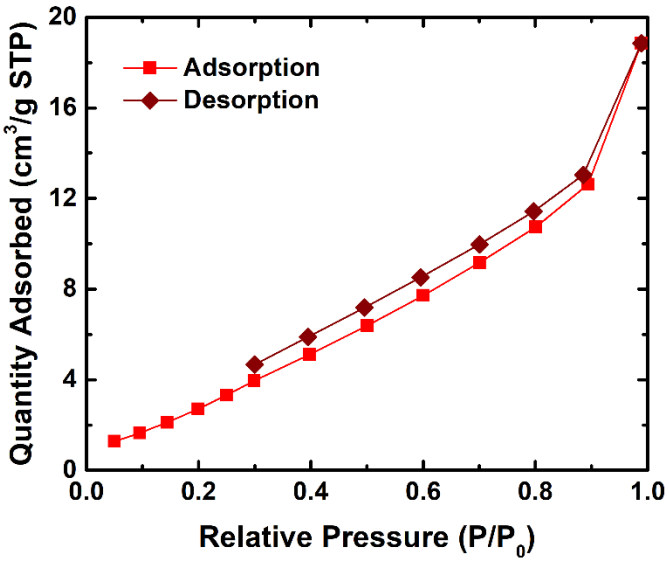

Figure 3.5 BET N_2-isotherm of pem-550 °C. BET surface area was calculated from adsorption when $P/P_0 < 0.4$.

3.3.2 Effect of the metal ions to polymer ratio and temperature

Other synthetic conditions of the PEM synthesis had been tested. **Figure 3.6a** shows the XRD patterns of samples with different metal-ions to PVA ratios and pyrolyzed at 500 ºC for 6 h. In both cases, the samples compose of RuO_2 tetragonal phase (PDF#: 00-40-1290) covered by amorphous complex, indicating 6:1 or 1:6 do not have enough polymers to effectively trap metal ions in the precursors and large quantity of samples remain amorphous at 500 ºC. **Figure 3.6b** and **3.6c** show the SEM images of 6:1 and 1:6 metal-ions to PVA ratio samples, respectively. The samples are composed of both big chunks and small particles. **Figure 3.6d** shows the XRD patterns of samples with 1:12 metal-ions to PVA ratio at different temperatures. At 200 ºC, the sample remains amorphous without crystalline phase can be identified. When the temperature increases to 500 ºC, clear RuO_2 tetragonal phase is formed, accompany with amorphous feature. The result indicates that 1:12 ratio sample has enough polymers to trap metal ions in the precursors and RuO_2 is formed at 500 ºC. The temperature, however, is not enough to form pyrochlore $Y_2Ru_2O_7$ phase. **Figure 3.6e** and **3.6f** show the SEM images of 1:12 ratio samples at 200 and 500 ºC, respectively. Sample at 200 ºC is composed of chunks of amorphous matrix while sample at 500 ºC crystalline particles are formed.

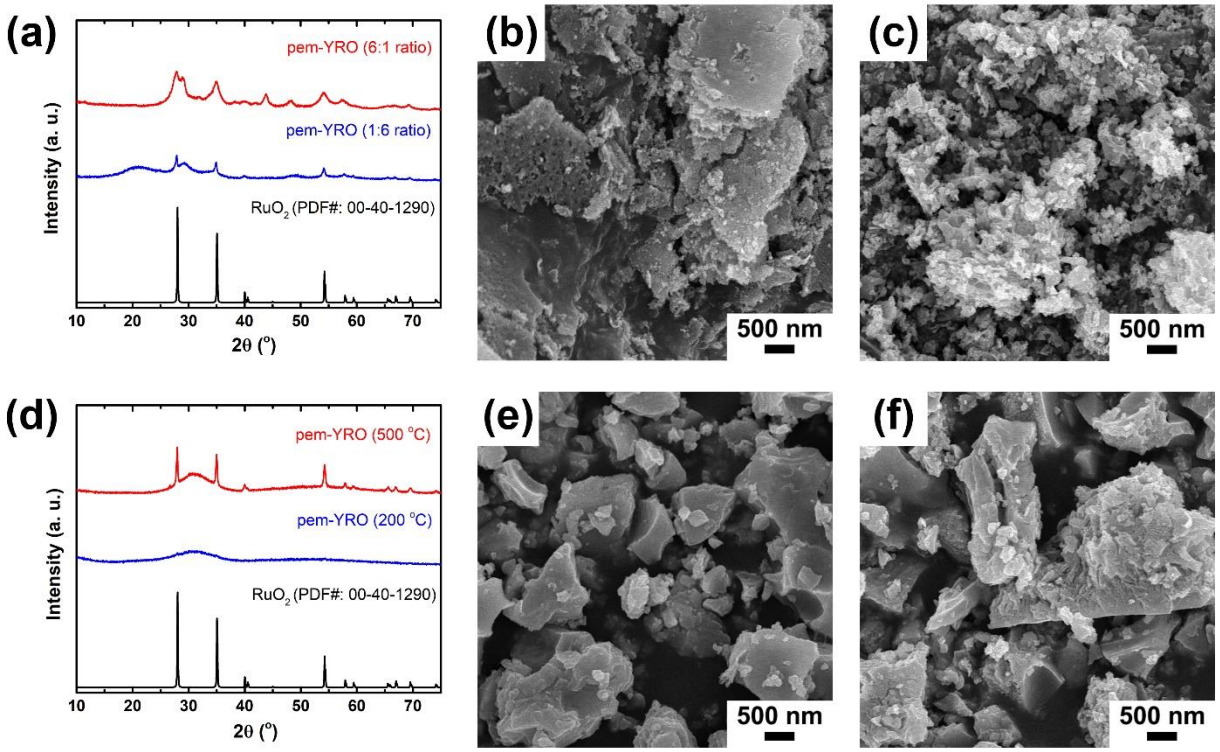

Figure 3.6 XRD patterns and SEM images of $Y_2Ru_2O_7$ synthesized by polymeric entrapment synthesis at different conditions. (a) XRD of pem-YRO with different metal ions to polymers ratios; SEM images of (b) 6:1 and (c) 1:6 ratios, respectively. (d) XRD of pem-YRO at different temperatures; SEM images of (e) 200 °C and (f) 500 ºC, respectively.

Different final annealing temperatures are also tested to study the effect of polymer entrapment synthesis. We further annealed the pem-550 ºC to 1000 ºC (to match the synthetic temperature of solgel process). **Figure 3.7a** shows the XRD pattern of $Y_2Ru_2O_7$ made by PEM synthesis at 1000 ºC (pem-1000 ºC) and $Y_2Ru_2O_7$ made by sol-gel synthesis (at 1000 ºC) as comparison. Both samples are phase pure $Y_2Ru_2O_7$ cubic structure while pem-1000 ºC shows broader peaks, indicating smaller grains of material nature. **Figure 3.7b** shows the SEM image of

pem-1000 ºC sample. When we compare pem-1000 ºC to pem-550 ºC, sintering of the particles can be observed, resulting 100 ~ 200 nm primary particle size in diameter. The result indicates that PEM synthesis is beneficial for forming small sized grains of high temperature phases ($Y_2Ru_2O_7$ pyrochlore in this case). Although sintering happens due to high temperature, pem-1000 ºC is agglomeration of small grains (indicated in XRD pattern) rather than bulk particles in case of sol-gel-1000 ºC.

The ramping rate was found to be critical in preparing phase pure $Y_2Ru_2O_7$ at low temperature. **Figure 3.7c** shows the XRD pattern of $Y_2Ru_2O_7$ made by PEM synthesis at 550 ºC with a slow ramping rate (5 ºC/min). Pyrochlore $Y_2Ru_2O_7$ phase is formed with impurities of RuO_2 and Y_2O_3. It is hypothesized that some RuO_2 and Y_2O_3 are formed during the heating process as those phases have a lower formation temperature than pyrochlore phase. Thus, minimizing time at lower temperature (flash pyrolysis) is critical for making phase pure $Y_2Ru_2O_7$. **Figure 3.7d** shows the SEM image of pem-550 ºC (5 ºC/min). The sample has a primary particle size of 10 ~ 50 nm, which is comparable to pem-550 ºC (flash pyrolysis). This also gives us an insight that ramping rate has minimum effect on the particle size. The particle size is mainly determined by sintering, in which final temperature is the major factor.

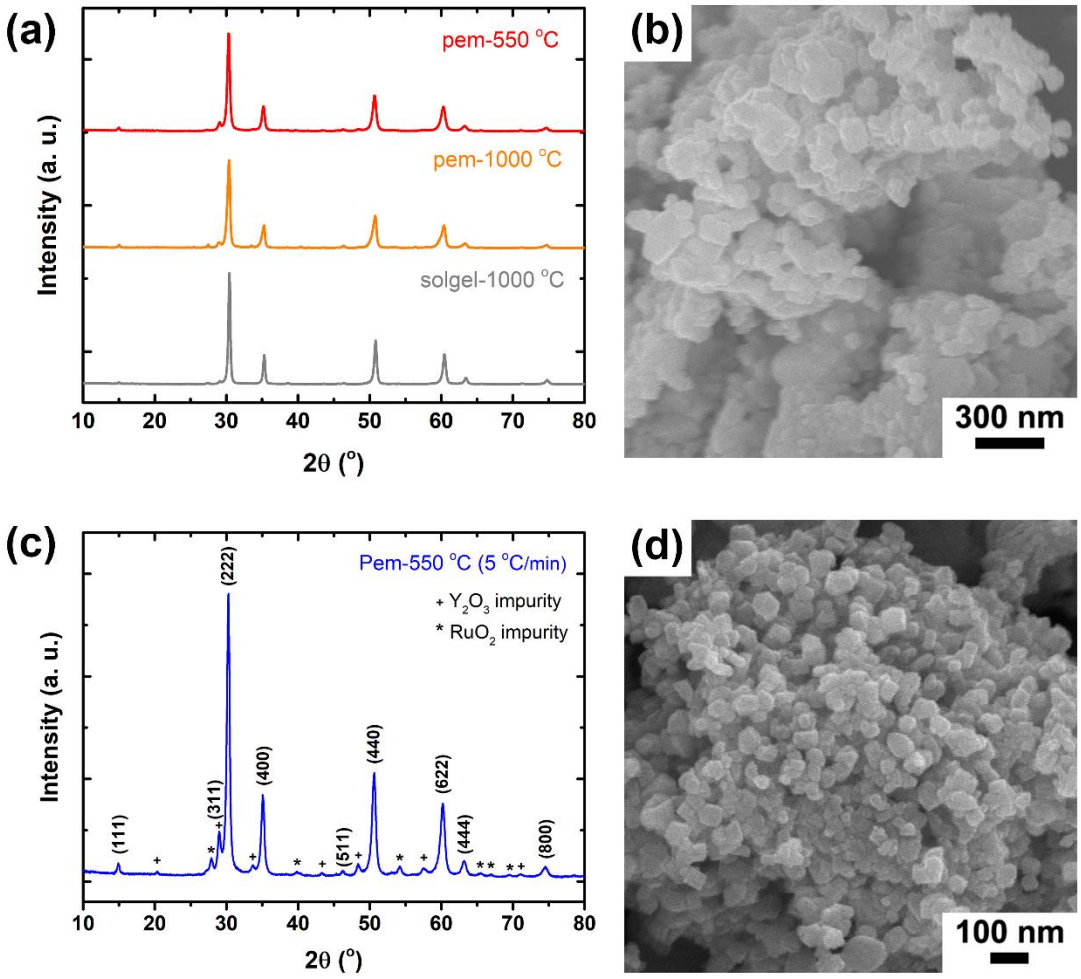

Figure 3.7 (a) XRD patterns of $Y_2Ru_2O_7$ samples made with PEM synthesis at 550 °C, 1000 °C, and sol-gel synthesis at 1000 °C, respectively. (b) SEM image of pem-1000 ºC. (c) XRD patterns of PEM synthesis $Y_2Ru_2O_7$ at 550 °C with slow ramping rate (5 °C/min). Symbols of "+" and "*" indicate impurity peaks of Y_2O_3 and RuO_2, respectively. (d) SEM image of pem-550 ºC (5 ºC/min).

3.3.3 OER activity and stability of pem-550 ºC

Cyclic voltammogram (CV) was performed for pem-550 ºC and solgel-1000 ºC as comparison to examine the OER activity. A rotating disk electrode (RDE), platinum wire and reference hydrogen electrode (RHE) were used as working, counter and reference electrode, respectively. All measurements were performed in O_2-saturated 0.1 M perchloric acid solution and corrected with resistance measured by *iR* compensation test. **Figure 3.8a** shows the CVs or those two samples. The onset potential of pem-550 ºC was measured to be 1.42 V versus RHE and the current density was 6.19 mA/cm^2 at 1.50 V. The solgel-1000 ºC sample showed an onset potential of 1.42 V, which is comparable to that of pem-550 ºC, but 3.61 mA/cm^2 current density at 1.50 V. **Figure 3.8b** shows the Tafel plots of mass activity to further study the OER kinetics of those two catalysts. The Tafel slope of pem-550 ºC was measured to be 37.25 mV/dec while Tafel slope of solgel-1000 ºC was measured to be 40.57 mV/dec. The results suggest that the associated OER kinetics of pem-550 ºC material is similar to that of solgel-1000 ºC, because the onset potentials of those two are close. However, pem-550 ºC possesses a superior OER activity over solgel-1000 ºC due to smaller particle size and high surface area nature. The current density branches larger especially at high overpotential (η) and pem-550 ºC is expected perform better at potential > 1.6 V.

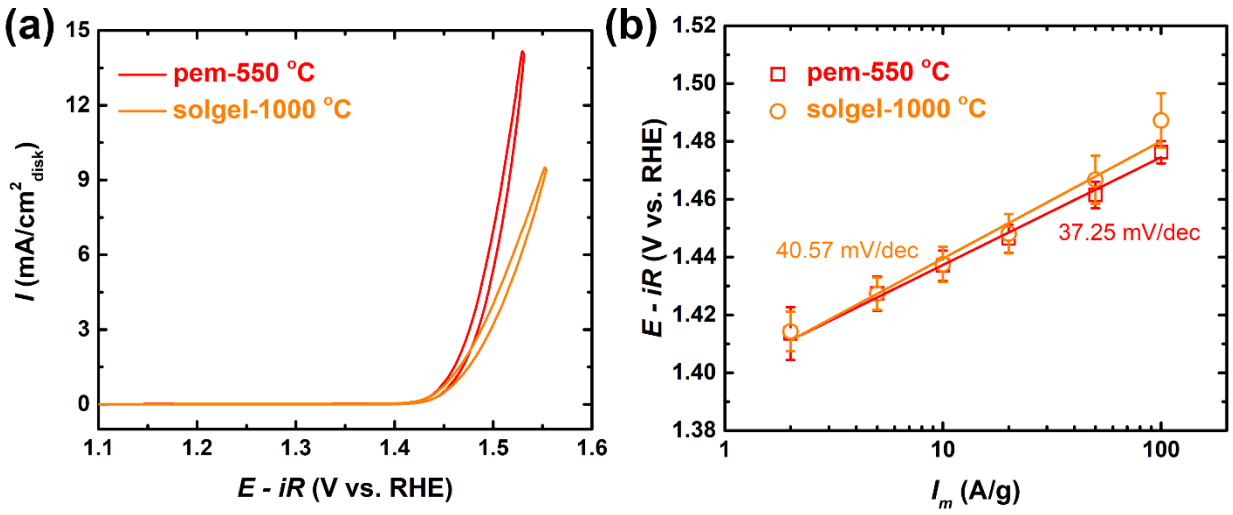

Figure 3.8 OER activity analysis of pem-YRO 550 °C compare to solgel-YRO 1000 °C. (a) shows the CV curves and (b) shows the Tafel plot.

Chronopotentiometry test of pem-550 ºC was performed to examine OER durability (**Figure 3.9a**). 0.75 mg of pem-YRO was loaded on a carbon paper with 1 cm^2 working area. 10 mA/cm^2 constant current was applied for more than 24 h to demonstrate the catalyst stability. Oxidation of carbon is negligible as the CV of a blank carbon paper showed no significant current with applied potential. The overpotential required for the pem-550 ºC electrode to generate 10 mA/cm^2 was about 0.27 V and remained constant during 24 h durability test, showing good stability of the catalyst. **Figure 3.9b** shows the TEM image of pem-550 ºC sample after OER durability test. The showed highly crystallized surface and bulk structure without amorphous surface layer formation. The lattice fringes were calculated from an average of 20 fringes. Clear 0.29 nm fringes which reflect the (222) plane of a cubic $Y_2Ru_2O_7$ can be seen. It further demonstrated the good OER activity and durability of pem-550 ºC catalyst.

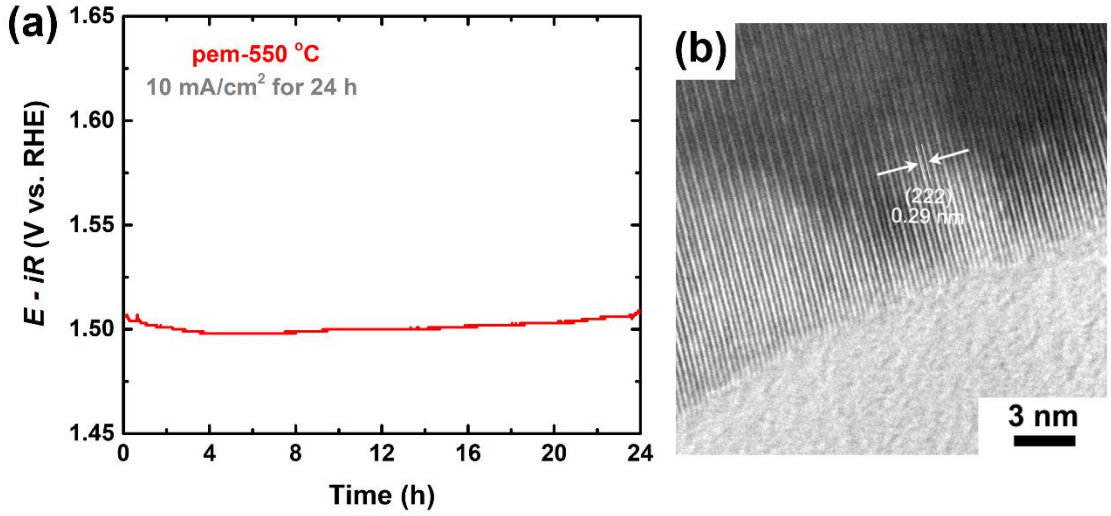

Figure 3.9 (a) OER durability test of pem-550 °C with constant 10 mA/cm^2 current density for 24 h. (b) TEM images of pem-550 °C after 24 h OER durability test. Clear lattice fringes of 0.29 nm, which represents the (222) plane, can be seen from the surface to the bulk throughout.

3.3.4 Electronic properties of pem-550 °C

EIS analysis was performed to understand the basic properties of the materials. **Figure 3.10** shows the Nyquist plots for pem-550 ºC and solgel-1000 ºC at (a) 0 V (no applied potential), (b) 1.42 V (at onset potential) and (c) 1.50 V, respectively. The equivalent electrical circuit is consisting of solution resistance (R_s), charge transfer resistance (R_{ct}) and double layer capacitance (C_{dl}). The charge transfer resistance can be used to examine the catalytic charge transfer rate and is estimated by the semi-circle diameters in Nyquist plot.[19,107] In **Figure 3.10a**, when no potential was applied, the charge transfer resistances are reflected to the intrinsic conductivity of the material.[19,108] It shows that pem-550 ºC electrode has a better conductivity than solgel-1000 ºC. It is hypothesized that the smaller sized particles of pem-550 ºC formed a more uniform and well-distributed film with the carbon conducting support, compare to solgel-1000 ºC. Because of the

semi-conducting to insulating nature of $Y_2Ru_2O_7$, carbon distribution plays an important role of electrode conductivity. In **Figure 3.10b** and **3.10c**, when potentials are applied and OER start to happen, pem-550 ºC electrode showed much smaller charge transfer resistance compare to solgel-1000 ºC, indicating that pem-550 ºC electrode has a faster OER kinetic rate than the solgel-1000 ºC electrode.

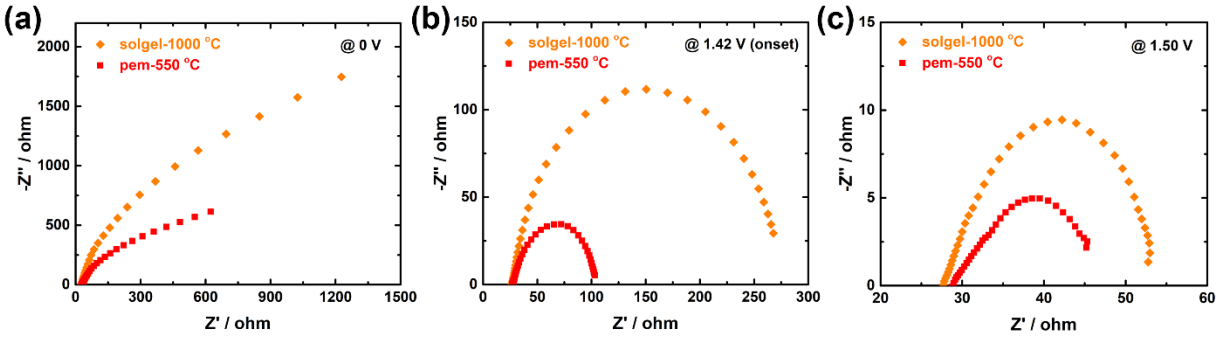

Figure 3.10 EIS analysis of pem-YRO 550 °C and solgel-YRO 1000 °C at (a) 0 V, (b) 1.42 V (onset) and (c) 1.50 V applied potentials, respectively.

To study the structural properties of pem-550 °C, we performed X-ray absorption spectroscopy (XAS) of the material with Ru foil and RuO_2 as references. **Figure 3.11a** shows the XANES of Ru K-edge spectra. The absorption edge energy (E_0) was measured to be 22129.9 eV for pem-550 °C, 22125.7 eV for Ru foil and 22132.3 eV for RuO_2, which are in good agreement with previously reported values.[99] The oxidation state of Ru in pem-550 °C is then calculated by a linear fit of absorption edge energy and valence state of Ru, where Ru foil preserves 0 oxidation state and RuO_2 preserves +4 oxidation state.[19,111] **Figure 3.11a** inset shows the relationship between edge energy and Ru oxidation state. The oxidation sate of Ru in pem-550 °C is determined

as +2.6. This result implies the pem-550 °C material possesses high concentration of oxygen defects, which is stated to be beneficial to OER activity in many reports.[27,28]

EXAFS analysis was performed to study the local Ru-O bonding structure and neighbor atoms' configuration. **Figure 3.11b** shows the k^2-weighted Fourier transform (FT) radial structure spectra of Ru K-edge in pem-550 °C. The peak at around 1.5 Å in radial distance is associated to the electron back scatterings and is corresponding to the first shell Ru-O_6. The bond distance of Ru-O was analyzed by simulating the $Y_2Ru_2O_7$ pyrochlore structure in 1 – 2 Å radial distance.[101] The Ru-O bonding distance pem-550 °C was determined as 1.99 Å, which aligns well with previously reported $Y_2Ru_2O_{7-\delta}$.[19]

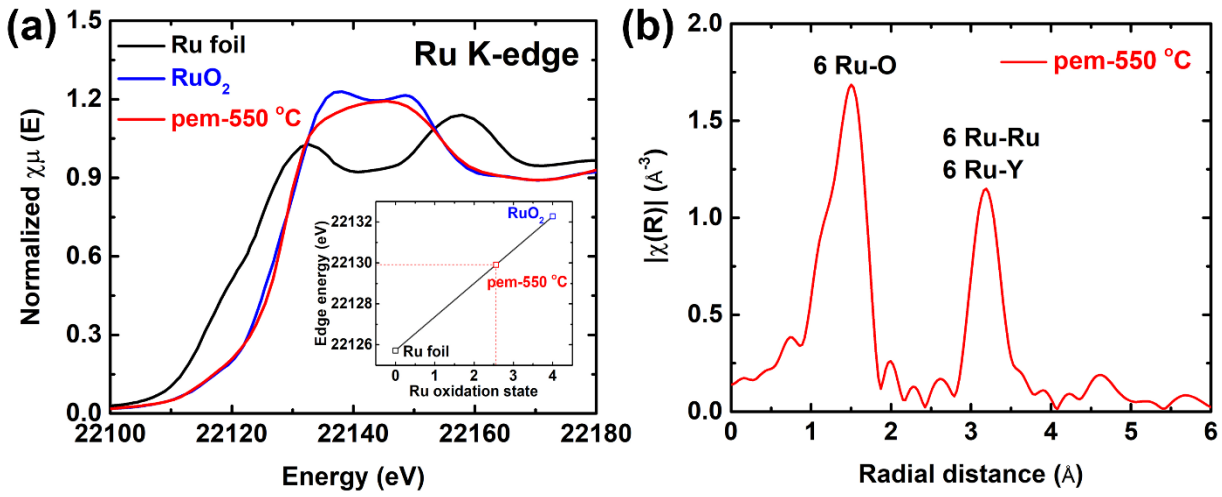

Figure 3.11 XAS analysis of pem-YRO 550 °C. (a) XANES spectra of pem-550 ºC with RuO_2 and Ru foil as reference sample. Inset shows the relationship between Ru K-edge energies and oxidation states of the materials. (b) Fourier transformed EXAFS spectra of Ru-edge for pem-550 ºC.

3.4 Conclusions

In summary, we successfully synthesized phase pure $Y_2Ru_2O_{7-\delta}$ pyrochlore with high surface area nanoparticles at low temperature (550 ºC) using polymeric entrapment synthesis. The material exhibited promising OER activity as well as stability in perchloric acid electrolyte solution. The high OER activity and stability are attributed to highly crystallized nanoparticles synthesized by PEM. The synthetic procedures can be easily adapted and broadened to synthesize other materials. This work provides a new strategy for synthesizing high surface area ceramic oxides, which have a high temperature stable phases, at low temperature and an advanced design of catalysts.

CHAPTER 4

PYROCHLORE-TYPE YTTRIUM IRIDATE ($Y_2Ir_2O_{7-\delta}$) OER CATALYSTS[3]

4.1 Introduction

For OER catalysts, RuO_2 and IrO_2 compounds are known as viable electrocatalysts in acid media, where IrO_2 is recognized as the catalyst with the best stability.[70] Ir-based catalysts have been studied widely recently because of their superior OER stability. Almost no exception when we look at recent publications of OER catalysts in acid, Ir is one of the components in the structure, such as multi-phase $IrO_x/SrIrO_3$ and $IrO_x/Y_2Ir_2O_7$ perovskite and pyrochlore materials. The scarceness of Ir, however, results in high cost for manufacturing of these catalysts and limits the wide range of implementations of water electrolysis devices. To advance the development, if Ir is inevitable component, we either want to reduce the percentage of Ir content or push the activity of OER catalysts to higher that we can effectively generate more values out of the catalysts. On the other hand, fundamental understanding of the activity origins is also important. It helps to a decision of catalyst selection and design. Although many theories of OER descriptors have been reported in the past decade (discussed in Chapter 1), it is vague whether those theories can be applied to more complex structures or there are other factors governing the OER activity.

In this chapter, we synthesized single-phase $Y_2Ir_2O_7$ pyrochlore electrocatalyst using a sol-gel method. The measured OER current density for this catalyst was about 3 times (0.86 $mA/cm^2_{catalyst}$) of that of a commercial IrO_2 (0.3 $mA/cm^2_{catalyst}$) at 1.55 V versus RHE under the acidic condition of pH 1. Therefore, $Y_2Ir_2O_7$ electrocatalyst may effectively reduce the amount

[3] Modified with permission, from Shih, P.-C.; Kim, J.; Sun, C.-J.; Yang, H. *ACS Appl. Energy Mater.* **2018**, *1*, 3992-3998.

used of Ir in water electrolysis when compared to IrO_2. The chronopotentiometry and X-ray photoelectron spectroscopy (XPS) analyses show the pyrochlore $Y_2Ir_2O_7$ electrocatalyst retains its activity at the constant current density of 10 mA/cm^2_{geo} without observable phase segregation over time. X-ray absorption spectroscopy (XAS) analysis further suggests that there exists a single electron filling in e'' orbital of its Ir 5d states due to the strong spin-orbit coupling.

4.2 Experimental procedures

4.2.1 Material synthesis

Stoichiometric amounts of yttrium nitrate ($Y(NO_3)_3 \cdot 6H_2O$, 99.9%, Alfa Aesar, 0.1915 g) and iridium chloride ($IrCl_3 \cdot xH_2O$, 99.8%, Alfa Aesar, 0.1493 g) were dissolved in 10 mL of deionized water (Barnstead E-Pure, Thermo-Scientific^{TM}) in a 50 mL beaker, followed by addition of citric acid (99%, Fisher Chemical, 0.4203 g). This solution was then heated at 80 °C for 5 h and a stir rate of 400 rpm on a hotplate/stirrer. The resulting solution was transferred to a vacuum oven and kept in the oven at 120 °C for 6 h to remove excess water. The solid was ground into a powder using a motor and pestle, placed in an alumina crucible, and transferred to a tube furnace (MTI GSL-1500X) for annealing in air. Temperature of the furnace was raised to 600 °C at a heating rate of 5 °C /min and maintained at this temperature for 6 h, and then to 1000 °C at 5 °C /min and maintained at this temperature for 12 h. The final product was cooled in the tube furnace to ambient temperature. The power samples were typically ground for about 15 min for the preparation of catalyst inks.

4.2.2 Material characterization

The crystal phase and structure analyses were performed by powder X-ray diffractometer (Rigaku MiniFlex 600) with the Cu X-ray source. The diffraction was taken in reflection mode with a scan range between 10° and 80° 2θ at a rate of 0.02° 2θ/s. The width of the incident and receiving Soller slits was set at 1.25°. The N_2 isotherm Brunauer-Emmett-Teller (BET) analysis was performed using a Micromeritics Gemini VII 2390 with 6-point measurement. Scanning electron microscopy (SEM) was conducted using a Hitachi S4700 microscope at the voltage of 10 kV. The catalyst powder was put on carbon tape on a SEM stub for imaging. The standard SEM mode was used, in which secondary electron emitted from a sample was detected. Transmission electron microscopy (TEM) was carried out using a JEOL 2100 Cryo microscope at an acceleration voltage of 200 kV. The TEM specimen was made by dispersing catalyst suspensions in ethanol and drop-casting onto carbon-coated copper grids. X-ray photoelectron spectroscopy (XPS) was performed on Kratos Axis ULTRA using an Al Kα X-ray source. The samples were loaded on fluorine-doped tin oxide (FTO) glass substrates and taped onto an XPS holder with copper tape for measurements. The CasaXPS software was used for processing the data and fitting the peaks.

X-ray absorption spectroscopy (XAS) was conducted with the Beamline 20-BM-B at the Advanced Photon Source (APS), Argonne National Laboratory, USA. The incident beam was monochromatized by using a Si (111) fixed-exit and a double-crystal monochromator. A harmonic rejection mirror was used to reject high-energy harmonics. Boron nitride powder was mixed with fine powders of $Y_2Ir_2O_7$, and IrO_2, respectively, and pelletized to an optimized sample thickness for measurement in transmission mode. The normalization of XAS spectra was performed using the Athena software. All spectra were calibrated with Pt foil. The extended X-ray absorption fine structure (EXAFS) data of $Y_2Ir_2O_7$ and IrO_2 were compared with iridium coordination

environment. The scattering paths between the Ir and neighboring atoms were calculated using the unit cell structures of $Y_2Ir_2O_7$ and IrO_2, respectively.

4.2.3 Determinations of electrocatalytic property

The OER activity was measured by rotating disk electrode (RDE) technique in a home-made three-compartment cell. The three-compartment cell includes one main jar, which contains a working electrode (e.g. RDE) and a gas bubbler, and two other compartments that contain counter and reference electrodes. Glass frit was used in the tube to connect the main jar and the counter-electrode compartment, while an inverted U-tube filled with the electrolyte was used to connect the main jar and the reference-electrode compartment. Pt wire (0.5 mm in diameter, Alfa Aesar) and hydrogen reference electrode (HydroFlex, Gaskatel) were used as the counter and reference electrodes, respectively. Perchloric acid (0.1 M) was used as the electrolyte solution. Ultrapure oxygen (99.999%, Air Gas) was introduced into the solution through a glass bubbler for at least 30 min before all measurements and continued during the experiment to ensure O_2 saturation. Thin film catalyst layer on glassy carbon electrode (0.196 cm^2) was prepared by drop-casting a pre-mixed catalyst ink solution, which was made of 1:1 wt% mixture of catalyst and Vulcan carbon (XC-72) suspended in tetrahydrofuran (THF) at the concentration of 2 mg/mL. After deposition of the catalyst ink, an additional layer of neutralized Nafion solution (pH~8, in THF) was dropped on top of the catalyst film.

Cyclic voltammetry (CV) was performed by a bipotentiostat (CHI760D, CH Instruments, Inc.) with a scan range from 1.1 to 1.6 V and at a rate of 10 mV/s. The rotation speed was set at 1600 rpm for all measurements. The obtained data were corrected by *iR* compensation after measurements. The resistance of the test cell was measured to be ~ 24 Ω. The transferred charge

versus scan rate data were collected using the same setup as those for the CV measurements at various scan rates (10 – 500 mV/s).

Chronopotentiometry measurement was carried out using conducting glass electrode. The electrode was prepared by drop-casting 40 μL of catalyst ink (described previously) in a 0.5 × 0.5 cm^2 area of fluorine-doped tin oxide glass substrate (FTO, MTI Corp). The area was defined by scratch tape and the catalyst loading was set at 0.16 mg/cm^2. The tape was removed after the catalyst ink was dried.

4.3 Result and Discussion

4.3.1 Structure analysis of $Y_2Ir_2O_7$ compound

Figure 4.1a shows the crystal phase analysis of as-made electrocatalysts by powder X-ray diffraction (PXRD) and Rietveld refinement. All PXRD peaks were in a good agreement with the cubic phase of pyrochlore-type $Y_2Ir_2O_7$ compound (*Fd-3m*, ICSD database code: 187534). The Rietveld refinement analysis shows good agreement between the experimentally measured data and simulated patterns (**Figure 4.1a**, **Table 4.1**). The inset illustrates the unit cell structure of pyrochlore $Y_2Ir_2O_7$ compound with IrO_6 subunits. **Figure 4.1b** shows the scanning electron microscope (SEM) image of as-synthesized $Y_2Ir_2O_7$ electrocatalyst, which had an average grain size of ~150 nm. The size of granular particles is much smaller than those made by the solid-state reaction route.[103] Transition electron microscope (TEM) image shows the $Y_2Ir_2O_7$ particles are highly crystalline throughout without any amorphous surface layer (**Figure 4.1c**).

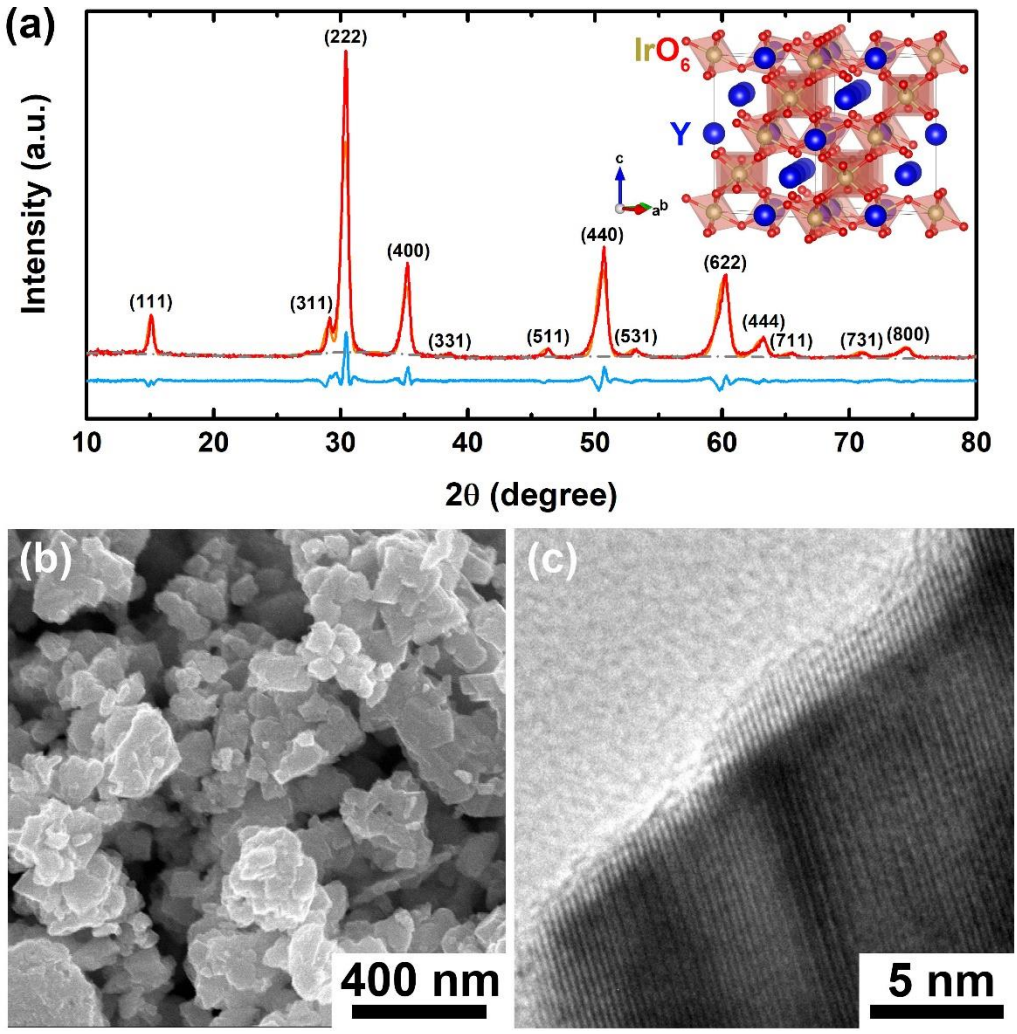

Figure 4.1 (a) PXRD and the corresponding Rietveld refinement with the residue plot, (b) SEM image, and (c) TEM micrograph of the as-made $Y_2Ir_2O_7$ electrocatalyst. Color code: red, experimentally determined diffraction pattern; orange, simulated pattern; blue: residue; and gray, baseline. Inset shows an illustration of the unit cell of the pyrochlore structure.

Table 4.1 Parameters for $Y_2Ir_2O_7$ Rietveld refinement

$Y_2Ir_2O_7$	u	v	w
Y	0.50000	0.50000	0.50000
Ir	0.00000	0.00000	0.00000
O1	0.33536	0.12500	0.12500
O2	0.37500	0.37500	0.37500
a = b = c = 10.10580 Å, α = β = γ = 90°, space group Fd-3m			
R_{wp} = 17.48%, R_p = 14.04%			

$$R_p = \frac{\sum y_i(obs) - y_i(calc)}{\sum y_i(obs)}, R_{wp} = \sqrt{\frac{\sum w_i\left(y_i(obs) - y_i(calc)\right)^2}{\sum w_i(y_i(obs))^2}}$$

Where $w_i = 1/y_i$, $y_i(obs)$ = observed intensity at step i, $y_i(calc)$ = calculated intensity at step i.

4.3.2 Catalytic performance of $Y_2Ir_2O_7$ electrocatalyst

Figure 4.2a shows the cyclic voltammetry (CV) curves for both $Y_2Ir_2O_7$ and IrO_2 electrocatalysts with the calculated current density at 1.55 V versus RHE, shown in the inset. The measured specific current density of the $Y_2Ir_2O_7$ electrocatalyst was 0.86 $mA/cm^2_{catalyst}$ at 1.55 V, which is about three times higher than that of IrO_2 reference catalyst (0.30 $mA/cm^2_{catalyst}$). The surface area of the electrocatalyst was experimentally determined to be 7.3 m^2/g for $Y_2Ir_2O_7$ and 28.4 m^2/g for IrO_2 reference based on the Brunauer-Emmett-Teller (BET) method using the nitrogen isotherm (**Figure 4.3**). **Figure 4.2b** shows the corresponding Tafel plots of $Y_2Ir_2O_7$ pyrochlore and IrO_2 reference electrocatalysts. Within the measured region of current density (0.02 – 2 $mA/cm^2_{catalyst}$), the $Y_2Ir_2O_7$ electrocatalyst had lower overpotentials than the IrO_2 reference. The determined Tafel slope values were 51.8 mV/dec for $Y_2Ir_2O_7$ electrocatalyst, and 49.3 mV/dec for IrO_2 electrocatalyst, which agrees with the value reported in previous studies.[70] Note that both

the OER current densities based off catalyst surface area and Ir-mass at 1.525 V of $Y_2Ir_2O_7$ catalyst in this study are higher than a reported study which had similar composition but multi-phases material $IrO_x/Y_2Ir_2O_7$.[67] The reported current densities were 0.08 $mA/cm^2_{catalyst}$ and 34.0 A/g_{Ir} for $IrO_x/Y_2Ir_2O_7$ while our data showed 0.33 $mA/cm^2_{catalyst}$ and 41.1 A/g_{Ir} for single phase $Y_2Ir_2O_7$. The difference of OER activity is suspected to result from higher synthesis temperature for $Y_2Ir_2O_7$ material in this study that formed better crystallized particles, therefore sustained its single phase composition and high activity during OER test.

To gain the insight of the relationship between intrinsic activity and reactive surface area of the catalysts, we calculated the transferred charge (q*) for the OER as a function of scan rate using the following equation:

$$q^* = \frac{\int I \times dE}{\upsilon} \qquad (4.1)$$

where I is the current density in mA/cm^2, E is the potential in V, and ν is the scan rate in V/s. **Figure 4.2c** shows the transferred charge (q*) as a function of scan rate, ν, in the CV measurement for these two catalysts. **Figure 4.4** shows the CV curves of $Y_2Ir_2O_7$ and IrO_2 at different scan rates. Within all measured scan rates (10 – 500 mV/s), $Y_2Ir_2O_7$ pyrochlore showed a higher transferred charge than the IrO_2 reference, indicating that more reaction sites were presented in the $Y_2Ir_2O_7$ electrocatalyst. At the infinite scan rate where $\nu^{-1/2}$ approaching zero (inset figure), the charge q^* represents the inner capacity of the electrode, which is related to the active sites.[61] The catalytic stability of $Y_2Ir_2O_7$ was analyzed by measuring chronopotentiometry on a fluorine-doped tin oxide (FTO) substrate at the constant current density of 10 mA/cm^2_{geo} for 24 h (**Figure 4.2d**). The potential curve kept essentially flat, thus, no obvious degradation of OER activity was detectable, indicating good catalytic stability of $Y_2Ir_2O_7$ pyrochlore electrocatalyst in acidic media and under

OER operating potential conditions. The intermittent discontinuity of the curve was due to the mechanical disturbance of the measurement vesicle to remove the generated oxygen bubbles.

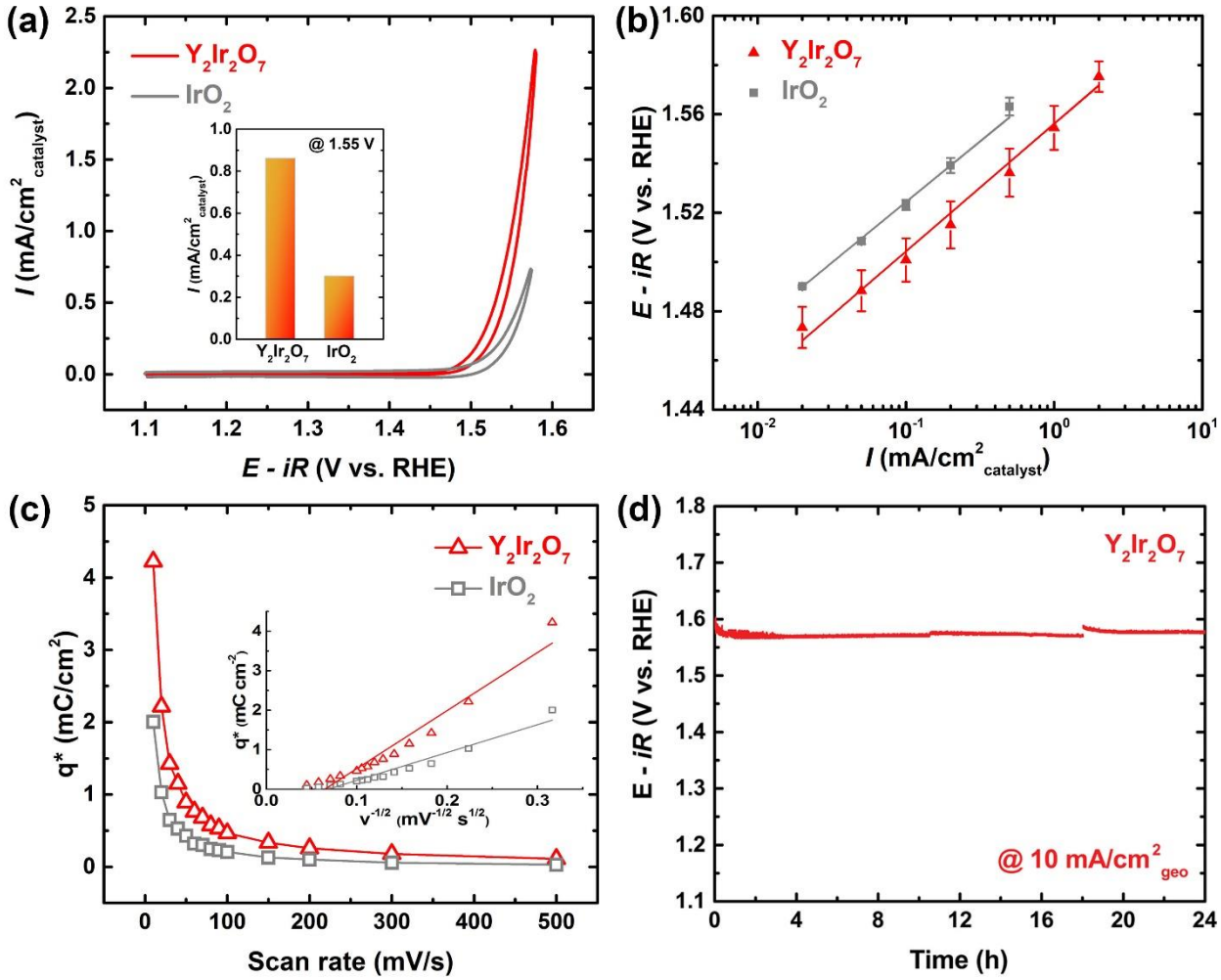

Figure 4.2 (a) OER current density analysis, (b) the corresponding Tafel plots, (c) voltammetry charge q* vs. scan rate curves of the $Y_2Ir_2O_7$ pyrochlore and IrO_2 reference electrocatalysts, and (d) OER stability analysis of $Y_2Ir_2O_7$ at 10 mA/cm$^2_{geo}$.The inset in (a) shows the comparison in specific current at 1.55 V between the two, and in (c) the plot of q* as a function of $v^{-1/2}$.

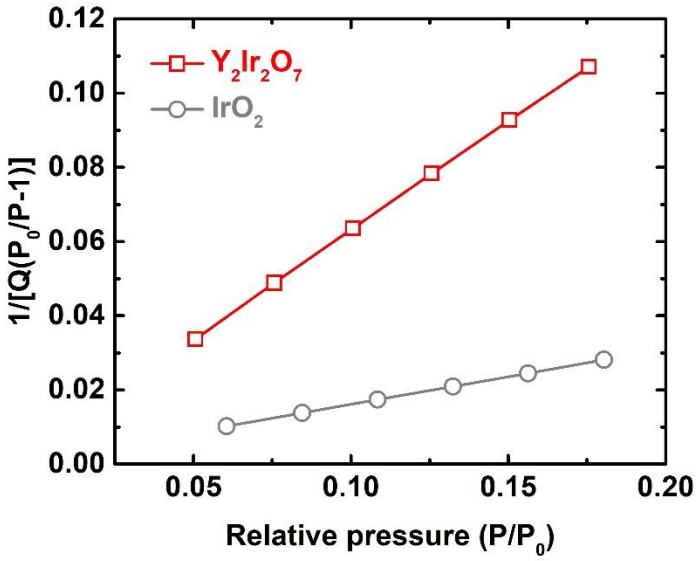

Figure 4.3 BET isotherms of $Y_2Ir_2O_7$ and IrO_2 electrocatalysts. Surface areas were determined based on the relative pressure P/P_0 in the range between 0.05 and 0.20.

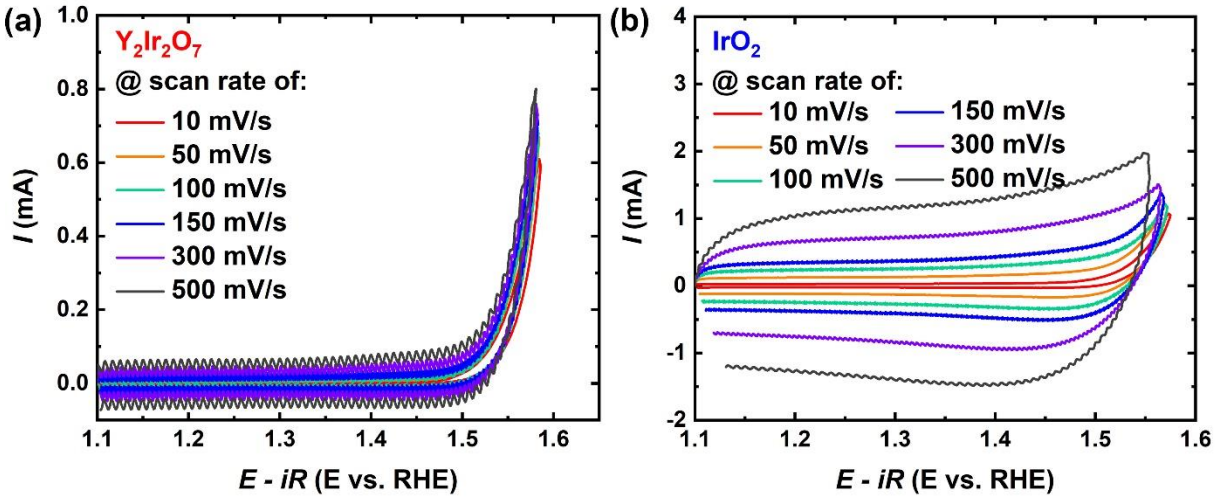

Figure 4.4 Representative CV curves of (a) $Y_2Ir_2O_7$ and (b) IrO_2 recorded at a scan rate between 10 and 500 mV/s.

X-ray photoelectron spectroscopy (XPS) was used to study the surface composition of $Y_2Ir_2O_7$ electrocatalyst before and after the OER measurements. **Figure 4.5a** and **4.5b** show the survey scans of the $Y_2Ir_2O_7$ electrocatalyst before and after OER stability test, respectively. The corresponding high-resolution XPS spectra of Ir 4f and Y 3d regions of this catalyst are shown in **Figure 4.5c** and **4.5d**, respectively. The ranges of binding energy (BE) are from 56 to 70 eV for Ir 4f peaks (top), and 150 to 160 eV for Y 3d peaks (bottom). The Ir 4f peaks fit with two sets of doublets with the primary peaks at 60.20 eV for Ir $4f_{7/2}$ and 63.18 eV for Ir $4f_{5/2}$, respectively. The secondary peaks are located at 62.00 and 64.98 eV. This observation is similar to those results previously reported,[66] where the two sets of doublet can be assigned to the screened and unscreened Ir^{4+} components.[123,124] Two sets of doublet were observed for Y 3d spectra. The primary peaks centered at 154.27 and 156.32 eV were assigned to $3d_{5/2}$ and $3d_{3/2}$ of Y^{3+}, respectively.[113] A secondary doublet centered at 155.62 and 157.67 eV was identified as well.[19] After the OER stability test, both spectra showed two sets of doublet with the primary peaks of Ir $4f_{7/2}$ and Y $3d_{5/2}$ components at 60.20 and 154.31 eV, respectively. No detectable binding energy, thus surface composition, changed for this pyrochlore catalyst before and after the OER tests.

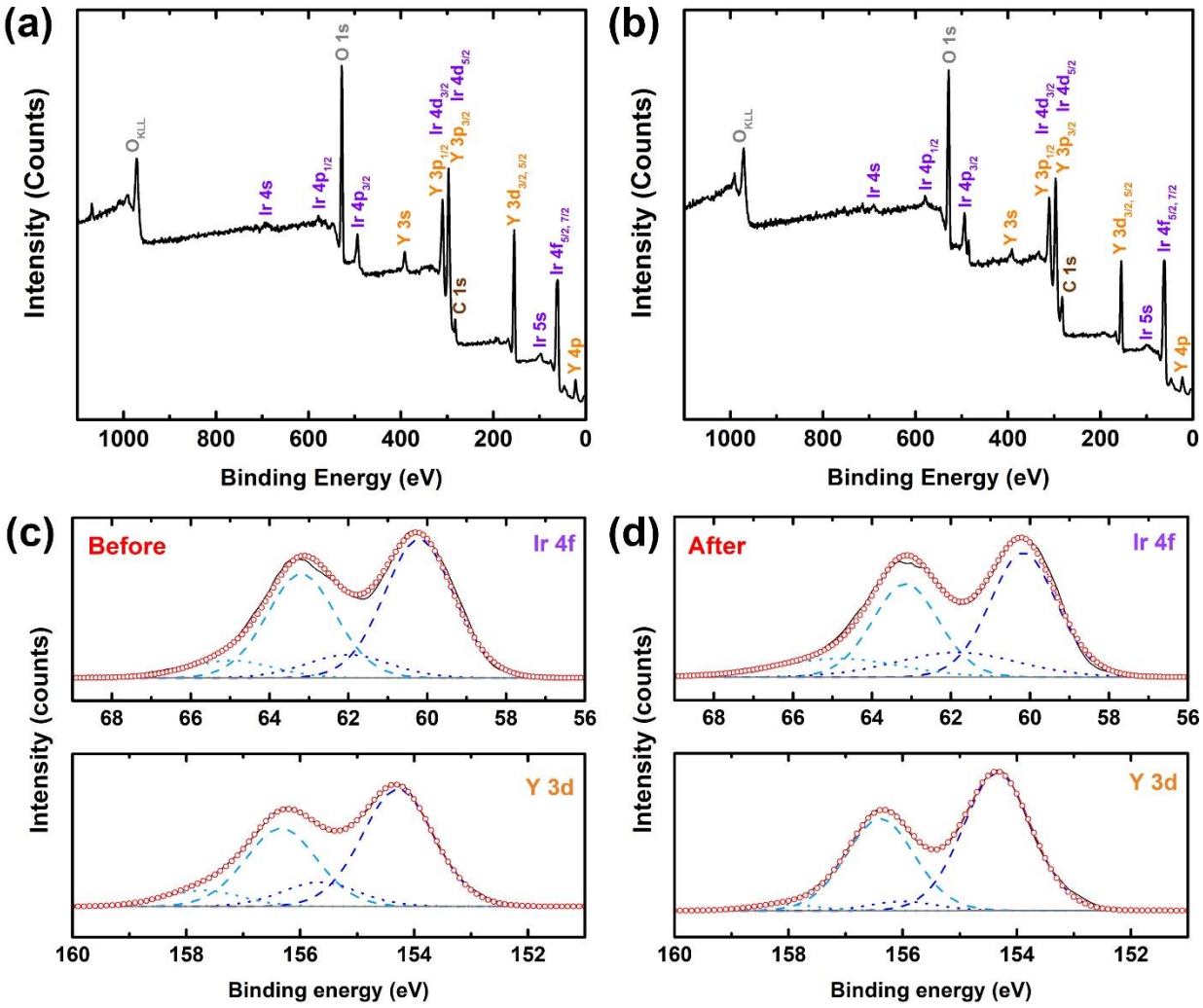

Figure 4.5 XPS analysis of $Y_2Ir_2O_7$ pyrochlore electrocatalysts. Survey scans of the (a) as-made sample, (b) after the OER stability test, and the Ir 4f and Y 3d regions (c) before, and (d) after the tests, respectively.

TEM was further employed to analyze the surface structure of the $Y_2Ir_2O_7$ electrocatalyst. **Figure 4.6** shows a representative TEM micrograph of a surface region of the catalyst after OER stability test. In comparison to the TEM image of as-made particles (**Figure 4.1c**), there was no obvious change on the surface region after the OER test. The lattice fringes are clearly visible from

the bulk to surface in both specimens, indicating no new layers were formed and the surface of the $Y_2Ir_2O_7$ electrocatalyst was stable. Both the XPS and TEM studies demonstrated that $Y_2Ir_2O_7$ electrocatalyst remained as a single-phase material before and after the OER stability test, showing its acid stability. Thus, the structures of high-temperature (1000 °C) prepared $Y_2Ir_2O_7$ pyrochlore electrocatalyst differed from those nanocrystalline catalysts made at the lower temperature (600 °C), showing good structural stability in acid.

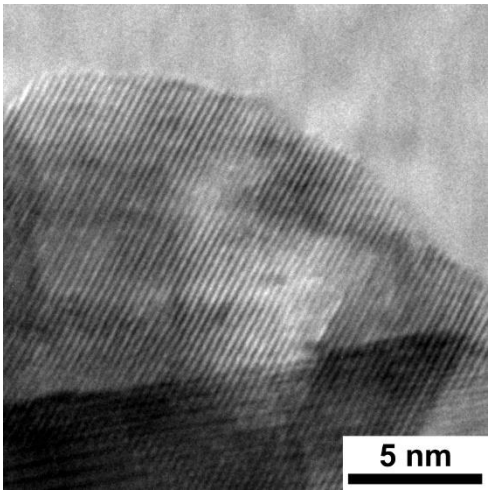

Figure 4.6 TEM micrograph of the $Y_2Ir_2O_7$ OER electrocatalyst after 10,000 CV cycles.

4.3.3 Electronic property study of $Y_2Ir_2O_7$

To understand the structural origin for the observed OER performance of $Y_2Ir_2O_7$, we characterized the electronic structure of pyrochlore $Y_2Ir_2O_7$ using X-ray absorption spectroscopy (XAS) and compared with the IrO_2 reference. **Figure 4.7a** and **4.7b** show the XAS spectra of Ir L_{III}-edge absorption energy (11215 eV) and Ir L_{II}-edge absorption energy (12827 eV), respectively, of $Y_2Ir_2O_7$ catalysts and IrO_2 reference. The Ir L_{III}-edge absorption, also known as the white line, is primarily attributed to the electron transition from Ir $2p_{3/2}$ to outer shell empty d orbitals. The Ir

L_{II}-edge absorption, on the other hand, is attributed to the electron transition from Ir $2p_{1/2}$ to outer shell empty orbitals. The absorption energy shifts and integrated intensities can be correlated to the Ir electronic structure in the oxides.[76,125]

Extended X-ray absorption fine structure (EXAFS) was performed to examine the Ir-O bond distance and the configuration of neighboring atoms. Fourier transform (FT) radial structure based on post-edge oscillation features of the XAS spectra was used in the EXAFS analysis. **Figure 4.7c** shows the k^2-weighted EXAFS data for $Y_2Ir_2O_7$ and IrO_2. The inset illustrates the center Ir cation, and the neighboring O and Y atoms at the first shell. The EXAFS peak intensity was mainly contributed by the electron back scatterings of the first shell atoms. The peaks at 1.60 Å are associated with the scattering between the Ir cation center and the six neighboring O anions. The peaks between 2.50 and 3.50 Å are attributed to Ir-Ir and Ir-Y back scattering for $Y_2Ir_2O_7$ and Ir-Ir for IrO_2, respectively. The Ir-O bond distance was found to be similar between the two catalysts, though $Y_2Ir_2O_7$ has slightly longer Ir-O bond distance than IrO_2.

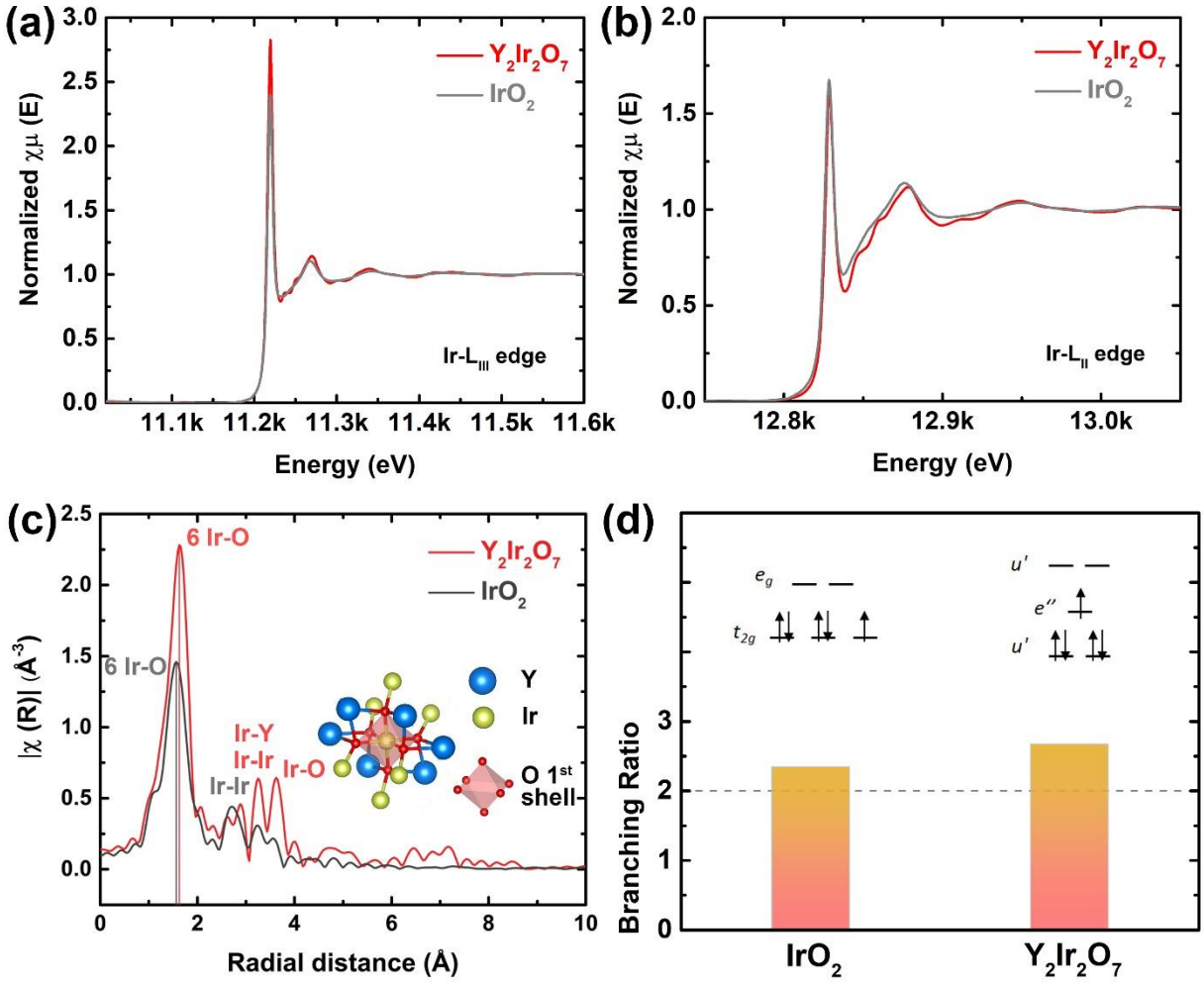

Figure 4.7 XAS spectra of normalized Ir (a) L_{III}- and (b) L_{II}- edges of $Y_2Ir_2O_7$ and IrO_2, respectively. (c) EXAFS of Ir L_{III}-edge of $Y_2Ir_2O_7$ and IrO_2. Inset illustrates the first shell oxygens in the unit cells. (d) Branching ratio (BR) analyses of $Y_2Ir_2O_7$ and IrO_2.

Figure 4.8a illustrates the deconvolution analysis of the integrated white line for $Y_2Ir_2O_7$ pyrochlore, using the peak fitting feature in the Athena software. An arctangent step function with defined unit height (green line) was used to model the absorption edge step, and a Lorentzian peak function (blue dashed line) was used for fitting the absorption edge. The sum of these two functions give the fitting curve (red line) which matches with the experimental data (dark grey lined scatters)

at the absorption edge. The same fitting method was applied in analyzing the IrO_2 Ir L_{III}-edge (**Figure 4.8b**) and Ir L_{II}-edge absorptions for $Y_2Ir_2O_7$ and IrO_2 (**Figure 4.9a** and **4.9b**). The white line integrated intensity (*i.e.*, absorption) was calculated by numerical integration of the shaded area, in which the experimental data was subtracted by the arctangent step function (*i.e.,* background). The ratio between integrated white line intensity of two edges, I_{L3}/I_{L2}, is known as the branching ratio (BR), which is used to analyze the spin-orbit coupling effect of Ir 5d states.[125-127] The ground-state expectation value of the spin-orbit operator $\langle L \cdot S \rangle$ can be interrelated with BR by the equation:

$$BR = \frac{2+r}{1-r} \quad where\ r = \langle L \cdot S \rangle / \langle n_h \rangle \qquad (4.2)$$

where n_h is the average number of holes. **Figure 4.7d** shows the BR and the corresponding orbitals of $Y_2Ir_2O_7$ and IrO_2. Using an average hole of 5, that is, $\langle n_h \rangle$ is equal to 5, the $\langle L \cdot S \rangle$ term was calculated to be 0.92 $\hbar^2$ for $Y_2Ir_2O_7$ and 0.52 $\hbar^2$ for IrO_2. **Table 4.2** summarizes the numbers of branching ratio analysis. The value of the spin-orbit coupling of $Y_2Ir_2O_7$ is close to two times that of IrO_2, suggesting that $Y_2Ir_2O_7$ more likely have an orbital splitting at the 5d ground state than IrO_2. The third-row transition metal ion, such as Ir^{4+}, are known to have electrons at the low-spin state.[127] This structure results in five electrons occupying t_{2g} orbitals, and no electron in e_g orbitals (**Figure 4.7d**, inset). For $Y_2Ir_2O_7$ electrocatalyst, the spin-orbit coupling results in the split of t_{2g} orbitals (j=5/2) into e'' and u' orbitals in its ligand field. With this configuration, four electrons should occupy the lower state u' orbital, leaving the single electron in the higher state e'' orbital (**Figure 4.7d**, inset). Such single state in upper most occupied orbital results in the high reactivity with absorbed oxygen, therefore the OER in the case of perovskite-type electrocatalysts, in which

the single electron occupies the e_g orbital.[11,17] Our OER performance data and XAS analysis strongly indicate the effect of single occupancy in the upper most occupied orbital on the OER activity should not be limited to perovskite and to e_g orbital only, that is, the single-unpaired electron state in e'' orbital of pyrochlore $Y_2Ir_2O_7$ electrocatalyst is also a favored configuration for a higher OER activity than that of IrO_2, as being observed in this study.

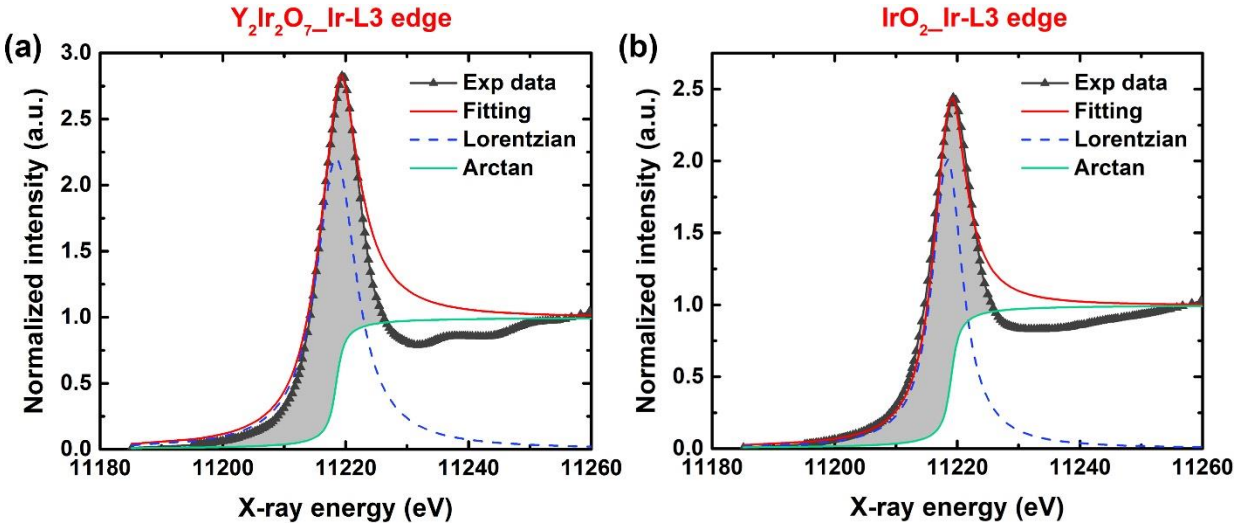

Figure 4.8 XANES curve fitting of Ir L_{III} edge in (a) $Y_2Ir_2O_7$ and (b) IrO_2, respectively, by using a set of arctangent step and Lorentzian peak functions in Athena software.

Table 4.2 Results of branching ratio analysis obtained for fitting the XANES data

	Integrated intensity		Branching ratio	$\langle L \cdot S \rangle$
	L3 edge	L2 edge	(BR)	($\hbar^2$)
$Y_2Ir_2O_7$	18.88	7.06	2.67	0.92
IrO_2	16.36	6.97	2.35	0.52

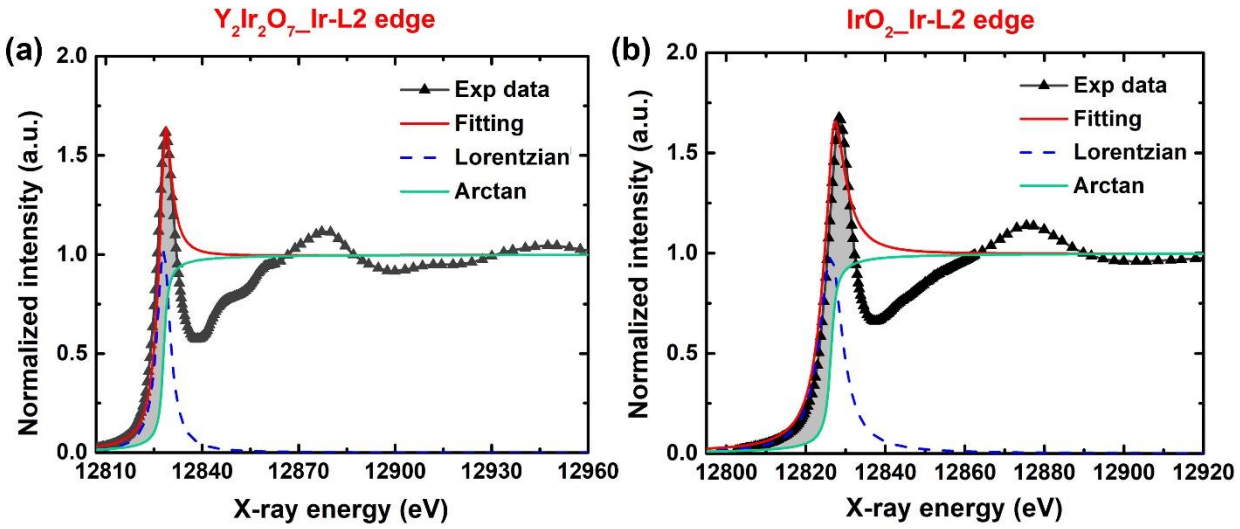

Figure 4.9 XANES curve fitting of Ir L_{II} edge in (a) $Y_2Ir_2O_7$ and (b) IrO_2, respectively, by using a set of arctangent step and Lorentzian peak functions in Athena software.

4.4 Conclusions

We synthesized the single-phase pyrochlore $Y_2Ir_2O_7$ electrocatalyst that is highly active towards OER under strongly acidic conditions. The intrinsic OER activity performed better than the IrO_2 reference electrocatalyst and did not alter surface layers after the tests. Based on XAS analysis, the pyrochlore $Y_2Ir_2O_7$ has the single electron in single orbital (SESO) structure. Both e'' orbital in $Y_2Ir_2O_7$ pyrochlore and e_g orbital in perovskite have such electronic configuration. Our findings provide insights to the favored structure for OER activity of an oxide electrocatalyst, and an approach to the structural optimization at the atomic and electronic levels through the control of spin-orbital coupling.

CHAPTER 5

STUDY OF THE STRUCTURAL DESCRIPTORS FOR OER CATALYSTS BASED ON $Ln_2Ir_2O_{7-\delta}$ PYROCHLORES

5.1 Introduction

Many researchers have studied the effects of energetic interactions between metal catalytic centers and adsorbed oxy-species on the OER kinetics. A moderate binding energy of metal and oxygen intermediates generally favors the high activity of OER catalysts.[7] Shao-Horn Yang *et al.* suggested based on a molecular-orbital approach, the e_g electron occupancy of perovskite oxide catalysts governed the OER activity.[11] A unity filling of this orbital resulted in optimal binding strength between metal and oxygen, thus higher OER activity. Although universal application of their theory is ambiguous, the method has offered important insights into the relationship between OER activity and electronic structures in perovskite.[17]

IrO_2 is considered state-of-the-art OER catalyst because of its excellent stability and reasonable activity towards OER in acid. However, it is not an ideal OER catalyst in terms of activity. Reports have shown that the binding between Ir and oxygen species of IrO_2 is too strong, likely limiting its activity.[9,40]

Within a crystal structure, bond distance often describes the information of the binding strength. If the bond distance is short, two atoms are closer to each other. Therefore, higher level of orbital overlapping and hybridization can happen, lead to a stronger binding. In a pyrochlore structure, it is possible to tune the structural and electronic properties by change of compositions.

Koo *et al.* showed that varying the A-site cationic radius in $A_2Ru_2O_7$ pyrochlores changes both the Ru-O bond distance and the Ru-O-Ru angle.[128]

In Chapter 4, the Ir-based $Y_2Ir_2O_{7-\delta}$ pyrochlore was presented which demonstrated outstanding OER activity while maintaining stability during OER testing. In this chapter, we investigate how structural features affect OER activity using a series of pyrochlore-type lanthanide iridate ($Ln_2Ir_2O_{7-\delta}$, Ln = Pr, Nd, Sm, Eu, Gd, Tb, Dy, Ho, Er, Tm, Yb and Lu). With a series of isoelectronic cations with similar crystal symmetries, this study unravels how structural features relate to OER activity.

5.2 Experimental procedures

5.2.1 Material synthesis

$Ln_2Ir_2O_{7-\delta}$ (Ln = Pr, Nd, Sm, Eu, Gd, Tb, Dy, Ho, Er, Tm, Yb, and Lu) pyrochlore oxides were synthesized following a sol-gel route. Stoichiometric amount of 0.5 mmol of each $Ln(NO_3)_3 \cdot xH_2O$ (99.9%, Sigma-Aldrich and Alfa Aesar) and $IrCl_3 \cdot xH_2O$ (Alfa Aesar) were mixed and dissolved in 10 mL of water, followed by addition of 2 mmol of citric acid (Alfa Aesar). The solution was transferred to an oil bath, heated to 80 ℃ for 5 h until gelation was observed. The solution was allowed for evaporation naturally and was transferred to a vaccum oven at 120 ℃ for 6 h to remove the water completely. The prepared solid was subjected to a sequential heat treatment at 600 ℃ for 6 h and 1,000 ℃ for 12 h at a ramping rate of 5 ℃/min.

5.2.2 Material characterization

X-ray diffraction (XRD) patterns were measured between 2θ = 10° and 80° (Rigaku Miniflex 600) in 0.02° steps and 1 sec/step rate using Cu Kα radiation (λ = 1.54056 Å). The cubic unit cell length (a) was calculated with following equation:

$$a^2 = d_{hkl}^2(h^2 + k^2 + l^2) \qquad (5.1)$$

where d_{hkl} is the interplanar spacings and Miller indices (hkl). The diffraction of (222) peaks were used after background subtraction made by the Sonnerveld & Visser method from the obtained XRD patterns.

SEM (Hitachi S4700) images were obtained at an acceleration voltage of 10 kV. The SEM specimen was prepared by depositing the powder catalysts on the carbon tape on a SEM stub. HRTEM (JEOL 2100 Cryo) images were acquired at 200 kV for surface structure characterization. Brunnauer-Emmett-Teller (BET, Micrometritics Gemini VII 2390) analysis was performed to calculate the suface area of the catalyst with 6-point measurement in the range P/P_0 = 0.06 – 0.18 under an N_2 adsorption environment.

X-ray absorption spectroscopy (XAS) was performed in transmission mode at beamline 20-BM-B at the Advanced Photon Source (APS), Argonne National Laboratory, USA. The obtained XAS spectra was analyzed by Artemis and Athena software. The extended X-ray absorption fine structure (EXAFS) spectra was Fourier-transformed with k^2 weight to obtain spectra plot in R-space (Å). The transformed EXAFS spectra were then fitted using the theoretical scattering paths with $Ln_2Ir_2O_7$ crystallographic information.

5.2.3 Geometry optimization of the unit cells

The theoretical calculation for the geometry optimization of the catalysts were performed using density functional theory (DFT). The generalized gradient approximation (GGA) with Perdew−Burke−Ernzerhof (PBE) functional was employed in CAmbridge Serial Total Energy Package (CASTEP) code. The $Y_2Ir_2O_7$ cubic pyrochlore unit cell was imported (ICSD code#: 187534). The A-site was substituted by the corresponding metal element in each $Ln_2Ir_2O_{7-\delta}$ using Material Studio 7.0 software. An optimal potential of U_{eff} = 4.0 eV was applied to Ir d-electrons. The energy cutoff for plane-wave basis set was set to 340.0 eV, where the sizes of the Monkhorst-Pack k-point grid and the FFT grid were set to 2 x 2 x 2 and 60 x 60 x 60, respectively.

5.2.4 Electrochemical measurement

Neutralized Nafion solution was prepared by adding 0.1 M NaOH solution to Nafion 117 aqueous solution (5%, Sigma-Aldrich) to adjust the pH to 8. A homogeneous catalyst ink solution was obtained by mixing 2 mg of pyrochlore oxide catalyst, 2 mg of carbon black (Vulcan XC-72), and 3 µL of previously prepared neutralized Nafion solution in 2 mL of tetrahydrofuran (THF). This solution was sonicated for 30 min. A rotating glassy-carbon disk electrode (RDE) was polished with 0.05 µm alumina slurry until a mirror surface was obtained. 5 µL of the prepared catalyst ink solution was drop-casted on the RDE. After the ink dried, 10 µL Nafion-THF solution (3 µL of neutralized Nafion solution in 2 mL of THF) was drop-casted to form a thin film electrode.

The electrochemical experiments were performed using a three-electrode system with a potentiostat (CHI 760D, CH instruments, Inc.). A platinum wire (diameter: 0.5 mm) connected with platinum foil (area: 1 cm^2) was used as a counter electrode. A hydrogen electrode (HydroFlex, Gaskatel) was used as a reference electrode and calibrated using H_2-saturated (S. J. Smith,

99,999%) 0.1 M $HClO_4$ (Veritas double distilled, 70%) electrolyte solution by cyclic voltammetry (CV) scans at a scan rate of 100 mV s^{-1} for 100 s. The average value of the two potentials at which the H_2 oxidation/evolution curves crossed zero current was taken to be the thermodynamic potential for the hydrogen reference electrode. OER measurements were performed three times after purging with O_2 (S. J. Smith, 99,999%) for at least 30 min. CV curves were collected at a scan rate of 10 mV s^{-1} in a potential range of 1.1-1.6 V versus RHE. The RDE rotating speed was fixed at 1,600 rpm. The resistance of the system was measured as ~24 Ω after the *iR* compensation test. The capacitance was corrected by taking the average value of anodic and cathodic scans to evaluate electrochemical performance.

5.3 Results and discussion

5.3.1 Structural analysis of $Ln_2Ir_2O_{7-\delta}$

Figure 5.1a shows the XRD patterns of as-synthesized 12 $Ln_2Ir_2O_{7-\delta}$ (Ln = Pr, Nd, Sm, Eu, Gd, Tb, Dy, Ho, Er, Tm, Yb and Lu) pyrochlores. All peaks can be indexed to a cubic pyrochlore structure (*Fd-3m*) without any noticeable impurities. When analyzed more closely, all the corresponding XRD peaks of $Ln_2Ir_2O_{7-\delta}$ shifted towards higher 2θ angles as the A-site change from Pr (bottom) to Lu (top). The gradual increase in lattice parameters as a function of the size of lanthanide cations followed the Bragg's rule. Magnified (222) and (622) planes are shown in **Figure 5.1a** (right). The (222) peaks shifted from 29.48° 2θ for $Pr_2Ir_2O_{7-\delta}$ to 30.59° 2θ for $Lu_2Ir_2O_{7-\delta}$. The (622) peaks shifted from 58.63° 2θ for $Pr_2Ir_2O_{7-\delta}$ to 60.47° 2θ for $Lu_2Ir_2O_{7-\delta}$. **Figure 5.1b** shows the unit cell structure of $Ln_2Ir_2O_7$ pyrochlore. The IrO_6 octahedra units are connected through corner-sharing oxygens, and the interstitial sites are occupied by A-site lanthanide cations. **Figure 5.1c** shows the cubic unit cell length (*a*) as a function of different A-sites. The unit cell

lengths were calculated by eq. 5.1 and using the (222) peaks. The unit cell length generally followed the trend of A-site lanthanide cation radius, with Pr being the largest and Lu being the smallest. The unit cell dimensions were further optimized by DFT calculation using the cell length calculated by (222) peaks (described in 5.2.3). In the geometry optimized cells, the Ir-O bond distance decreased monotonically based on the cell lengths, meaning that $Pr_2Ir_2O_{7-\delta}$ showed the longest Ir-O bond distance while $Lu_2Ir_2O_{7-\delta}$ showed the shortest.

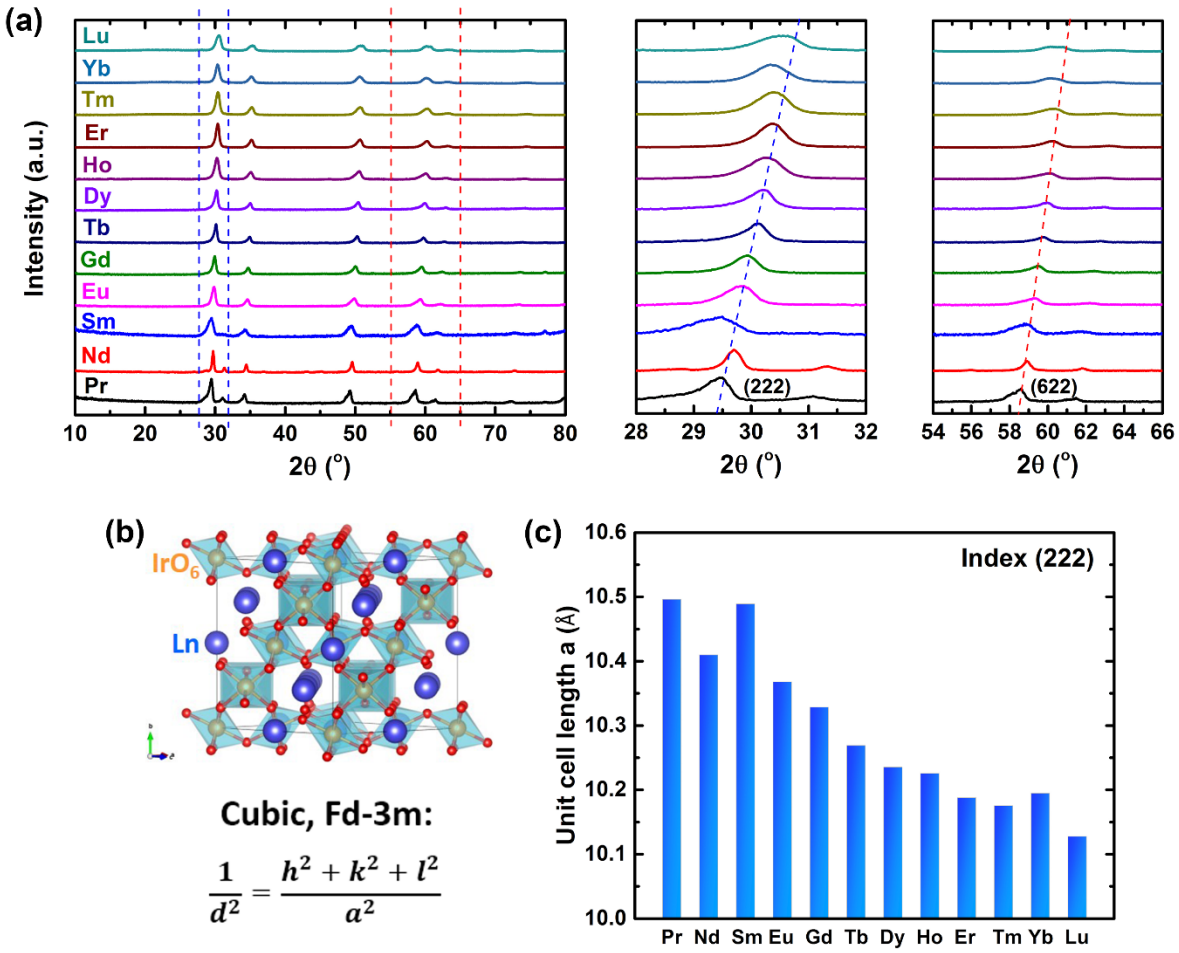

Figure 5.1 Structural analysis of $Ln_2Ir_2O_{7-\delta}$. (a) XRD of as-made pyrochlore materials. Full XRD patterns are shown in the left. Blue dashed lines indicate the 2θ range of cubic (222) peak, which are also shown in the middle magnified XRD patterns. Red dashed lines indicate the (622) peaks region and magnified patterns are shown in the right. The peaks shifted towards higher angle as the A-site cations go from Pr to Lu, indicating an increase of lattice distance. (b) Cubic unit cell structure of $Ln_2Ir_2O_7$ pyrochlore (Ln = Pr, Nd, Sm, Eu, Gd, Tb, Dy, Ho, Er, Tm, Yb and Lu). Corner-shared IrO_6 octahedral units are shown in polyhedral style. (c) Cubic unit cell length of $Ln_2Ir_2O_{7-\delta}$ calculated from d-spacing of (222) peaks.

5.3.2 OER activities of $Ln_2Ir_2O_7$ pyrochlores

OER catalytic performance of $Ln_2Ir_2O_7$ pyrochlores was measured using rotating disk (RDE) technique (details are described in 5.2.4). **Figure 5.2a** shows the solution resistance (*iR*) corrected CV curves of twelve $Ln_2Ir_2O_7$ pyrochlores (noted as LnIrO, Ln = Pr, Nd, Sm, Eu, Gd, Tb, Dy, Ho, Er, Tm, Yb and Lu). The current densities are normalized to BET surface area of all materials to evaluate the intrinsic OER activity regardless of particle sizes. Onset potentials of 270 ~ 300 mV are observed for $Ln_2Ir_2O_7$ catalysts. **Figure 5.2b** shows the Tafel plot corresponding to the CV curves. Of the twelve pyrochlore structures, $Pr_2Ir_2O_7$ and $Nd_2Ir_2O_7$ showed the highest OER activities. At higher potentials (right side), these two materials exhibit much higher current densities compared to the others. **Figure 5.3c** shows the overpotential comparison of the twelve catalysts at 0.45 mA cm^{-2} by increasing atomic number of the Ln metal cation. On the left side, $Pr_2Ir_2O_7$ had the lowest overpotential which increased moving to the right from Pr to Eu. For the metals right of Eu (Tb to Lu), the overpotentials are approximately constant (~350 mV or 1.58 V vs. RHE), and within a range of ~ 10 mV.

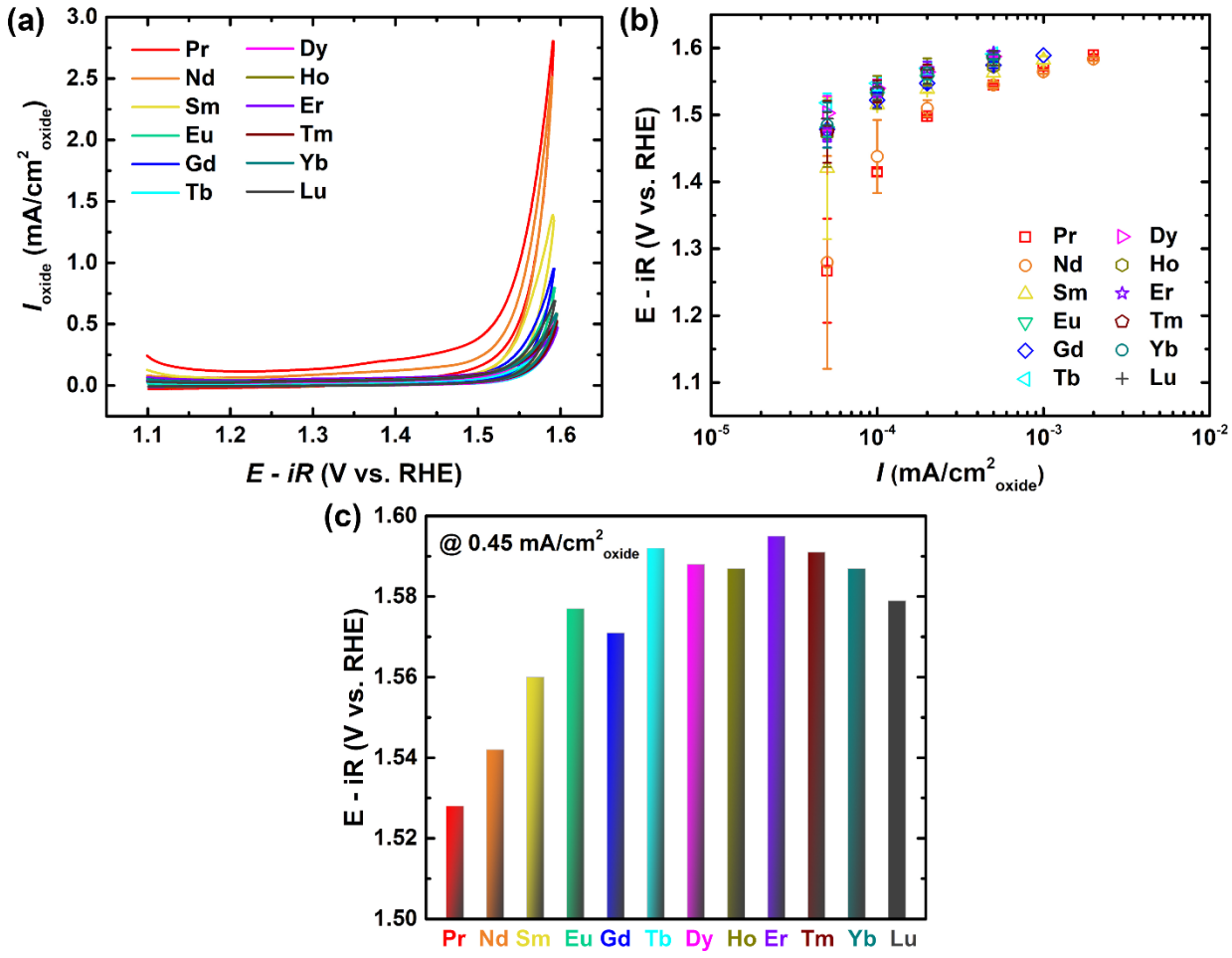

Figure 5.2 Electrochemical measurement on the OER activities of $Ln_2Ir_2O_{7-\delta}$. (a) CV curves and (b) Tafel plots of $Ln_2Ir_2O_{7-\delta}$ pyrochlores (Ln = Pr, Nd, Sm, Eu, Gd, Tb, Dy, Ho, Er, Tm, Yb and Lu). (c) Overpotentials for all materials at 0.45 mA cm^{-2}. All curves are from the average of three individual measurements and the error bars are shown in Tafel graph. The potentials are corrected with 100% *iR* solution resistance compensation.

5.3.3 Structural analysis of $Ln_2Ir_2O_{7-\delta}$ pyrochlores and correlation to OER activity

XAS was carried out for the $Ln_2Ir_2O_{7-\delta}$ (Ln = Pr, Nd, Sm, Eu, Gd, Tb, Dy, Er, Tm) pyrochlores to study the structural properties. **Figure 5.3a** shows the L_{III} and L_{II} edges of Ir for nine materials. The L_{III} edge XANES spectra was used for analyzing Ir oxidation states. **Figure 5.3b** shows the correlation of integrated WL intensities and Ir oxidation states (details of WL fitting and area integration are presented in Chapter 4) with IrO_2 and $IrCl_3$ as the references. The oxidation states of Ir in the $Ln_2Ir_2O_{7-\delta}$ pyrochlores are near 3.2, with PrIrO shows the highest Ir oxidation state with 12.90 integrated WL intensity and TmIrO shows the lowest Ir oxidation state with 12.48 integrated WL intensity. **Figure 5.3c** shows the branching ratios of those materials calculated by Ir L_{III} and L_{II} edges (details of fitting and calculation methods are described in Chapter 4). PrIrO shows the highest branching ratio at 1.83, and the number decreases as A-site goes from Pr to Tm (1.77). Note that there is a bigger decrease of branching ratio from EuIrO to GdIrO and from ErIrO to TmIrO.

EXAFS analysis was carried out to look at the local structure of IrO_6 and bond distance of Ir and O in the pyrochlore structure. **Figure 5.4a** shows the Fourier-transformed k^2-weighted EXAFS of Ir L_{III} edges. The peak near 1.5 Å in radial distance corresponds to the 6 Ir-O bond, associated with the electronic back-scatterings between Ir and the neighboring O atoms in the first shell of IrO_6. The peak near 3.5 Å is attributed to both the Ir-Ir and Ir-Ln bonds. The EXAFS data were fit with a simple first shell scattering to acquire the factor corrected Ir-O bond distance (see details in 5.2.2). **Figure 5.4b** shows the correlation of Ir-O bond distance and the atomic number of A-site. NdIrO shows the highest Ir-O distance with 2.10 Å and ErIrO with the lowest 2.01 Å. Note that he Ir-O bond distance obtained from this method does not follow the trend that is

observed in the geometry optimized unit cells, where the Ir-O bond distance increases monotonically when A-site cation radius increases (Pr > Nd > … > Tm > Yb > Lu).

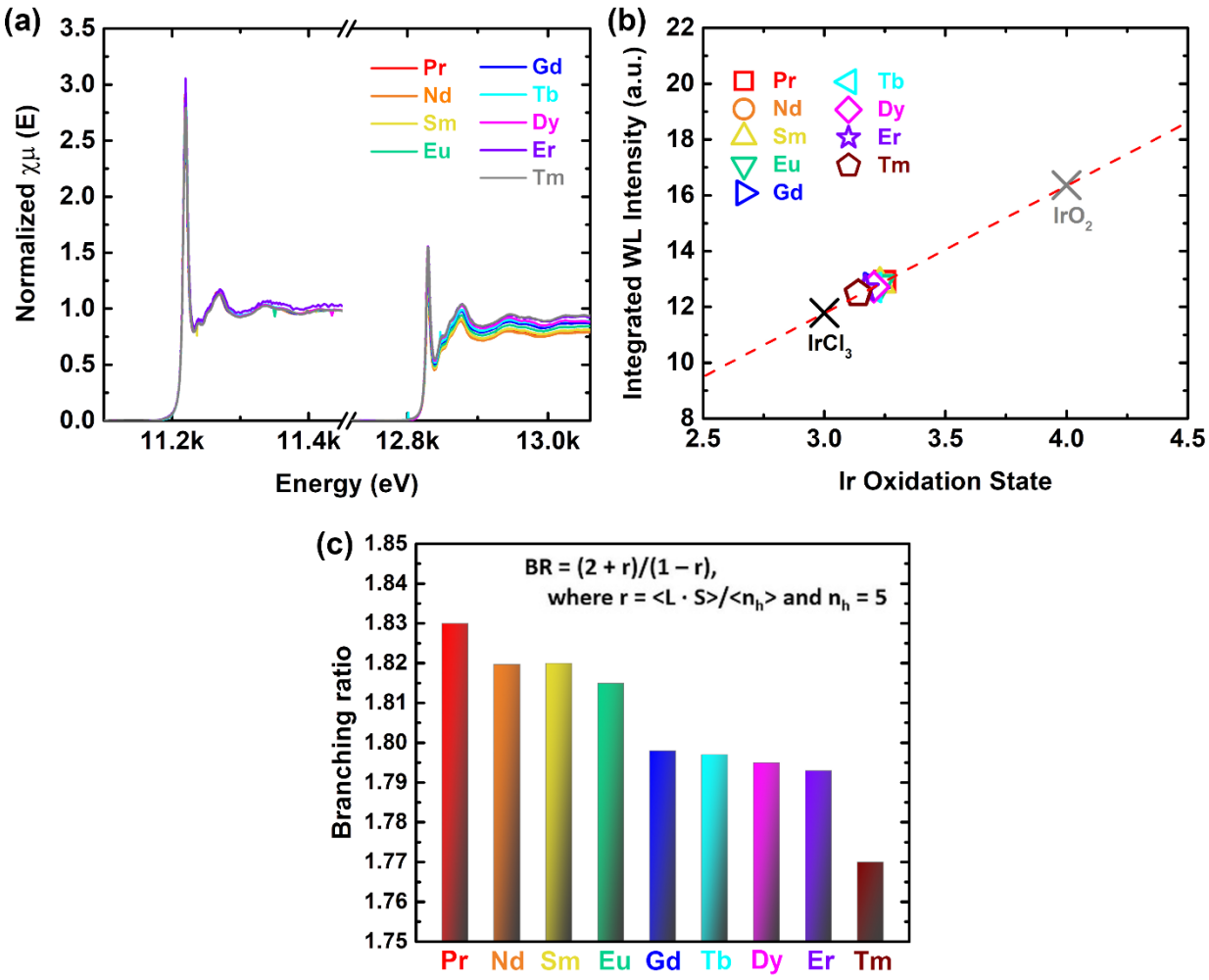

Figure 5.3 Electronic properties of $Ln_2Ir_2O_{7-\delta}$ pyrochlores. (a) XAS of L_{III} and L_{II} edges of Ir in the pyrochlores. (b) Ir oxidation states in various pyrochlores with IrO_2 and $IrCl_3$ as the references. The integrated WL intensities were calculated with Ir L_{III} edges using the fitting method described in Chapter 4. (c) branching ratio comparison of different pyrochlores. Detailed fitting and evaluation on the WL and branching ratio are following the method discussed in Chapter 4.

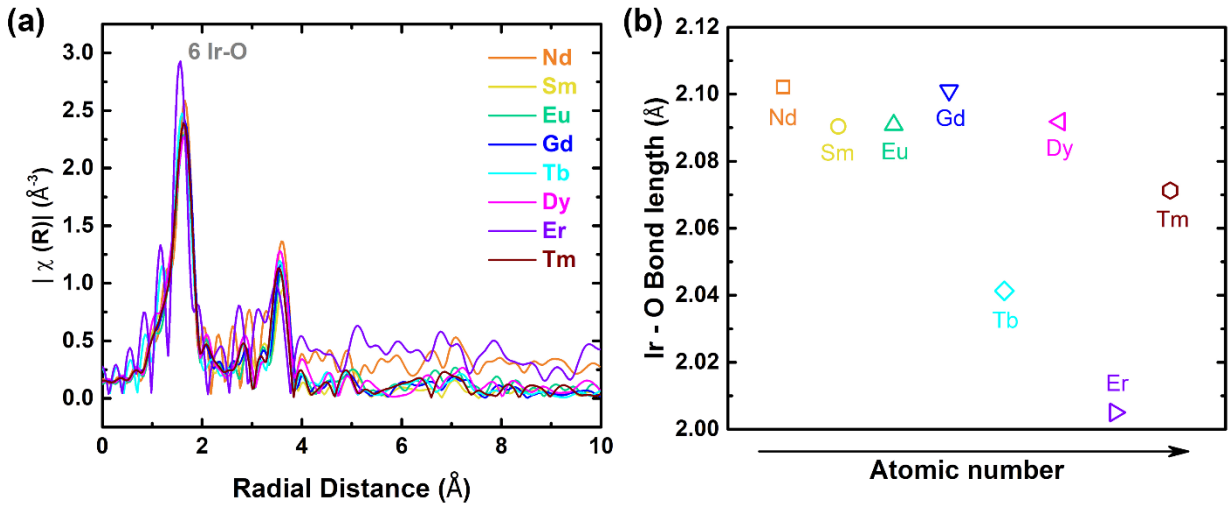

Figure 5.4 Radial distance of the Ir-O bonds analysis. (a) k^2-weighted Fourier transformed (FT) EXAFS oscillations with the scattering paths for the first shell of IrO_6 of $Ln_2Ir_2O_{7-\delta}$ pyrochlores. (b) Ir-O bond lengths in different A-site pyrochlores. The Ir-O bond lengths are calculated by first shell simulated factor correction for the radial distance of EXAFS spectra.

Figure 5.5 summarizes how the choice of metal cation affects the properties of $Ln_2Ir_2O_{7-\delta}$ pyrochlores: Ir oxidation state (from Ir L_{III} XANES spectra), branching ratios (from Ir L_{III} and L_{II} edges), Ir-O bond distance (from EXAFS data), and the experimental OER overpotential at 0.45 mA cm^{-2}. In a broad view, $Ln_2Ir_2O_{7-\delta}$ pyrochlores with early lanthanide A-sites show better OER activity while having higher Ir oxidation states and larger branching ratios. Although the Ir-O bond distance acquired from EXAFS data does not align with DFT calculated result and XRD data, a better fitting of the EXAFS data can be achieved by selecting reasonable radial distance range and precise crystallographic information.

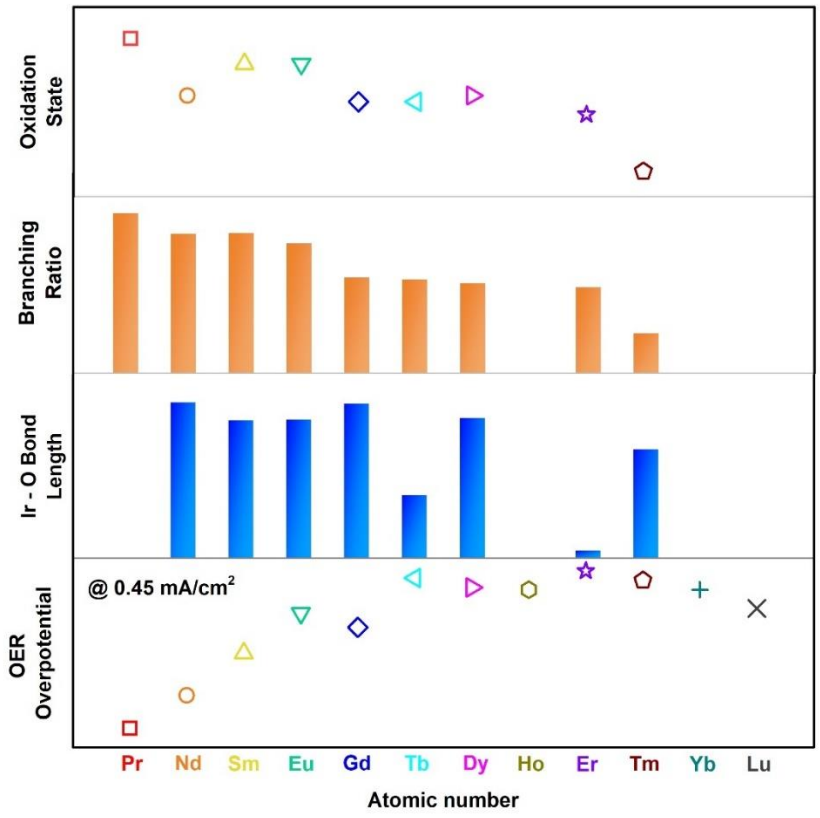

Figure 5.5 Summary of how $Ln_2Ir_2O_{7-\delta}$ pyrochlores change by choice of A-metal cation by the Ir oxidation state, branching ratio, Ir-O bond distance, and OER activities at 0.45 mA cm^{-2} (y-axis is the overpotential at 0.45 mA cm^{-2}).

5.4 Conclusions

In this chapter, the key structural attributes to the OER activity is systematically studied by twelve $Ln_2Ir_2O_{7-\delta}$ pyrochlores, where the crystal symmetry and catalytic center (Ir) are the same. A broad trend of higher OER activity is seen when larger A-site cation radii, higher oxidation states of Ir, larger branching ratios, and longer distance Ir-O bond lengths. Although other OER descriptor might be found, this study provides an insight for the selection and optimization of the atomic structures of OER catalysts.

CHAPTER 6

GENERAL CONCLUDING REMARKS AND FUTURE WORK

In this dissertation, the pyrochlore-type yttrium ruthenate catalysts were developed and studied. The $Y_2Ru_2O_{7-\delta}$ catalyst showed an enhanced OER activity and stability compare to the classic RuO_2 catalyst. XAS analysis indicated the enhanced OER activity was likely a result of the local Ru electronic structure change found in the pyrochlore structure. The Ru oxidation state of $Y_2Ru_2O_{7-\delta}$ was determined to be lower than the case of RuO_2. This relates to the binding between Ru and O which affects the kinetic pathway of OER. DFT calculations suggested that the local electron hybridization between Ru d-orbital and O p-orbital were more stable than the case of RuO_2. This property made $Y_2Ru_2O_{7-\delta}$ stable during OER operation.

Different synthetic approaches were developed to produce high surface area and porous pyrochlore materials. By applying polymeric entrapment synthesis, the synthetic temperature of making $Y_2Ru_2O_{7-\delta}$ had been largely reduced from 1000 °C to 550 °C. This synthesis approach decreases particle sintering that occurs more rapidly at high temperatures. Therefore, $Y_2Ru_2O_{7-\delta}$ pyrochlore synthesized by the PEM had higher surface area and enhanced OER activity while maintaining its acid stability. In related work, we modified our established sol-gel synthesis and introduced perchloric acid as a porogen to generate pores during the synthesis. Porous $Y_2[Ru_{1.6}Y_{0.4}]O_{7-\delta}$ was synthesized, showing large OER activity enhancement due to higher surface area and other structural factors.

A single-phase yttrium iridate pyrochlore was successfully made as a new acid-stable OER catalyst. The $Y_2Ir_2O_7$ pyrochlore catalyst showed largely enhanced OER activity compare to

classic IrO_2 catalyst and showed great stability for 24 h 10 mA cm^{-2} OER stability test. XPS analysis showed that the $Y_2Ir_2O_7$ single-phase structure was stable, likely due to the highly crystallized particles. XAS was applied to study and understand the activity origin and OER descriptors. XANES was used to characterize the local electronic structure of Ir and for branching ratio analysis. A more reactive orbital state was present in the $Y_2Ir_2O_7$ pyrochlore which led to the high OER activity. A systematic study of the lanthanide iridate $Ln_2Ir_2O_{7-\delta}$ pyrochlores indicated that the selection of A-site cation had a major effect on the OER activity. By our observation, selecting element with larger cationic radius (e.g. Pr, Nd in lanthanides) will result in higher OER activity in a $Ln_2Ir_2O_{7-\delta}$ pyrochlore structure.

Area major discovery of this work is that by adopting pyrochlore structures, Ru- and Ir-based catalysts will see large enhancement in both OER activity and stability. New pyrochlore structures can be developed to tune these properties. The Ru and Ir local structure play a critical role in OER activity, and we have provided a few examples of how this dependence. Additionally, we provide two synthetic approaches to generate high surface area pyrochlore materials. These findings offer a fresh view on the design principles for high-performance OER catalysts and a new venue for advancing the development of water electrolysis devices.

REFERENCES

(1) Lewis, N. S.; Nocera, D. G. Powering the planet: Chemical challenges in solar energy utilization. *Proc. Natl. Acad. Sci. U. S. A.* **2006**, *103*, 15729-15735.

(2) Lewis, N. S. Toward Cost-Effective Solar Energy Use. *Science* **2007**, *315*, 798-801.

(3) Graetzel, M. Artificial photosynthesis: water cleavage into hydrogen and oxygen by visible light. *Acc. Chem. Res.* **1981**, *14*, 376-384.

(4) Bard, A. J.; Fox, M. A. Artificial Photosynthesis: Solar Splitting of Water to Hydrogen and Oxygen. *Acc. Chem. Res.* **1995**, *28*, 141-145.

(5) Turner, J. A. Sustainable Hydrogen Production. *Science* **2004**, *305*, 972-974.

(6) Carmo, M.; Fritz, D. L.; Mergel, J.; Stolten, D. A comprehensive review on PEM water electrolysis. *Intl. J. Hydrogen Energy* **2013**, *38*, 4901-4934.

(7) Rossmeisl, J.; Qu, Z. W.; Zhu, H.; Kroes, G. J.; Nørskov, J. K. Electrolysis of water on oxide surfaces. *J. Electroanal. Chem.* **2007**, *607*, 83-89.

(8) Man, I. C.; Su, H.-Y.; Calle-Vallejo, F.; Hansen, H. A.; Martínez, J. I.; Inoglu, N. G.; Kitchin, J.; Jaramillo, T. F.; Nørskov, J. K.; Rossmeisl, J. Universality in Oxygen Evolution Electrocatalysis on Oxide Surfaces. *ChemCatChem* **2011**, *3*, 1159-1165.

(9) Seh, Z. W.; Kibsgaard, J.; Dickens, C. F.; Chorkendorff, I.; Nørskov, J. K.; Jaramillo, T. F. Combining theory and experiment in electrocatalysis: Insights into materials design. **2017**, *355*.

(10) Dau, H.; Limberg, C.; Reier, T.; Risch, M.; Roggan, S.; Strasser, P. The Mechanism of Water Oxidation: From Electrolysis via Homogeneous to Biological Catalysis. *ChemCatChem* **2010**, *2*, 724-761.

(11) Suntivich, J.; May, K. J.; Gasteiger, H. A.; Goodenough, J. B.; Shao-Horn, Y. A Perovskite Oxide Optimized for Oxygen Evolution Catalysis from Molecular Orbital Principles. *Science* **2011**, *334*, 3.

(12) Kim, H.; Park, J.; Park, I.; Jin, K.; Jerng, S. E.; Kim, S. H.; Nam, K. T.; Kang, K. Coordination tuning of cobalt phosphates towards efficient water oxidation catalyst. *Nat. Commun.* **2015**, *6*, 8253.

(13) Kim, J.; Chen, X.; Shih, P.-C.; Yang, H. Porous Perovskite-Type Lanthanum Cobaltite as Electrocatalysts toward Oxygen Evolution Reaction. *ACS Sustainable Chem. Eng.* **2017**, *5*, 10910-10917.

(14) Rossmeisl, J.; Logadottir, A.; Nørskov, J. K. Electrolysis of water on (oxidized) metal surfaces. *Chem. Phys.* **2005**, *319*, 7.

(15) Bockris, J. O. M.; Otagawa, T. Mechanism of Oxygen Evolution on Perovskites. *J. Phys. Chem.* **1983**, *87*, 12.

(16) Bockris, J. O. M.; Otagawa, T. The Electrocatalysis of Oxygen Evolution on Perovskites. **1984**, *131*.

(17) Hwang, J.; Rao, R. R.; Giordano, L.; Katayama, Y.; Yu, Y.; Shao-Horn, Y. Perovskites in catalysis and electrocatalysis. *Science* **2017**, *358*, 751-756.

(18) Modeshia, D. R.; Walton, R. I. Solvothermal synthesis of perovskites and pyrochlores: crystallisation of functional oxides under mild conditions. *Chem. Soc. Rev.* **2010**, *39*, 4303-4325.

(19) Kim, J.; Shih, P.-C.; Tsao, K.-C.; Pan, Y.-T.; Yin, X.; Sun, C.-J.; Yang, H. High-Performance Pyrochlore-Type Yttrium Ruthenate Electrocatalyst for Oxygen Evolution Reaction in Acidic Media. *J. Am. Chem. Soc.* **2017**, *139*, 12076-12083.

(20) Goodenough, J. B.; Manoharan, R.; Paranthaman, M. Surface protonation and electrochemical activity of oxides in aqueous solution. *J. Am. Chem. Soc.* **1990**, *112*, 2076-2082.

(21) Zhao, Q.; Yan, Z.; Chen, C.; Chen, J. Spinels: Controlled Preparation, Oxygen Reduction/Evolution Reaction Application, and Beyond. *Chem. Rev.* **2017**, *117*, 10121-10211.

(22) Cheng, F.; Shen, J.; Peng, B.; Pan, Y.; Tao, Z.; Chen, J. Rapid room-temperature synthesis of nanocrystalline spinels as oxygen reduction and evolution electrocatalysts. *Nat. Chem.* **2010**, *3*, 79.

(23) Chen, R.; Wang, H.-Y.; Miao, J.; Yang, H.; Liu, B. A flexible high-performance oxygen evolution electrode with three-dimensional $NiCo_2O_4$ core-shell nanowires. *Nano Energy* **2015**, *11*, 333-340.

(24) Liu, Y.; Wang, H.; Lin, D.; Liu, C.; Hsu, P.-C.; Liu, W.; Chen, W.; Cui, Y. Electrochemical tuning of olivine-type lithium transition-metal phosphates as efficient water oxidation catalysts. *Energy Environ. Sci.* **2015**, *8*, 1719-1724.

(25) Orikasa, Y.; Masese, T.; Koyama, Y.; Mori, T.; Hattori, M.; Yamamoto, K.; Okado, T.; Huang, Z.-D.; Minato, T.; Tassel, C.; Kim, J.; Kobayashi, Y.; Abe, T.; Kageyama, H.; Uchimoto, Y. High energy density rechargeable magnesium battery using earth-abundant and non-toxic elements. *Sci. Rep.* **2014**, *4*, 5622.

(26) Kim, J.; Yin, X.; Tsao, K.-C.; Fang, S.; Yang, H. $Ca_2Mn_2O_5$ as Oxygen-Deficient Perovskite Electrocatalyst for Oxygen Evolution Reaction. *J. Am. Chem. Soc.* **2014**, *136*, 14646-14649.

(27) Mefford, J. T.; Rong, X.; Abakumov, A. M.; Hardin, W. G.; Dai, S.; Kolpak, A. M.; Johnston, K. P.; Stevenson, K. J. Water electrolysis on $La_{1-x}Sr_xCoO_{3-\delta}$ perovskite electrocatalysts. *Nat. Commun.* **2016**, *7*, 11053.

(28) Kim, J.; Shih, P.-C.; Qin, Y.; Al-Bardan, Z.; Sun, C.-J.; Yang, H. A Porous Pyrochlore $Y_2[Ru_{1.6}Y_{0.4}]O_{7-\delta}$ Electrocatalyst for Enhanced Performance towards the Oxygen Evolution Reaction in Acidic Media. *Angew. Chem. Int. Ed.* **2018**, *57*, 13877-13881.

(29) De Chialvo, M. R. G.; Chialvo, A. C. Oxygen evolution reaction on $Ni_xCo_{(3-x)}O_4$ electrodes with spinel structure. *Electrochem. Acta* **1993**, *38*, 2247-2252.

(30) Nikolov, I.; Darkaoui, R.; Zhecheva, E.; Stoyanova, R.; Dimitrov, N.; Vitanov, T. Electrocatalytic activity of spinel related cobalties $M_xCo_{3-x}O_4$ (M = Li, Ni, Cu) in the oxygen evolution reaction. *J. Electroanal. Chem.* **1997**, *429*, 157-168.

(31) Jin, C.; Lu, F.; Cao, X.; Yang, Z.; Yang, R. Facile synthesis and excellent electrochemical properties of $NiCo_2O_4$ spinel nanowire arrays as a bifunctional catalyst for the oxygen reduction and evolution reaction. *J. Mater. Chem. A* **2013**, *1*, 12170-12177.

(32) Blakemore, J. D.; Gray, H. B.; Winkler, J. R.; Müller, A. M. Co_3O_4 Nanoparticle Water-Oxidation Catalysts Made by Pulsed-Laser Ablation in Liquids. *ACS Catalysis* **2013**, *3*, 2497-2500.

(33) Liang, Y.; Li, Y.; Wang, H.; Zhou, J.; Wang, J.; Regier, T.; Dai, H. Co_3O_4 nanocrystals on graphene as a synergistic catalyst for oxygen reduction reaction. *Nat. Mater.* **2011**, *10*, 780.

(34) Suntivich, J.; Gasteiger, H. A.; Yabuuchi, N.; Shao-Horn, Y. Electrocatalytic Measurement Methodology of Oxide Catalysts Using a Thin-Film Rotating Disk Electrode. *J. Electrochem. Soc.* **2010**, *157*, B1263-B1268.

(35) Stoerzinger, K. A.; Risch, M.; Suntivich, J.; Lü, W. M.; Zhou, J.; Biegalski, M. D.; Christen, H. M.; Ariando; Venkatesan, T.; Shao-Horn, Y. Oxygen electrocatalysis on (001)-oriented manganese perovskite films: Mn valency and charge transfer at the nanoscale. *Energy Environ. Sci.* **2013**, *6*, 1582-1588.

(36) Suntivich, J.; Gasteiger, H. A.; Yabuuchi, N.; Nakanishi, H.; Goodenough, J. B.; Shao-Horn, Y. Design principles for oxygen-reduction activity on perovskite oxide catalysts for fuel cells and metal-air batteries. *Nat. Chem.* **2011**, *3*, 5.

(37) Ponce, J.; Rehspringer, J. L.; Poillerat, G.; Gautier, J. L. Electrochemical study of nickel–aluminium–manganese spinel $Ni_xAl_{1-x}Mn_2O_4$. Electrocatalytical properties for the oxygen evolution reaction and oxygen reduction reaction in alkaline media. *Electrochim. Acta* **2001**, *46*, 3373-3380.

(38) Chi, B.; Li, J.; Yang, X.; Lin, H.; Wang, N. Electrophoretic deposition of $ZnCo_2O_4$ spinel and its electrocatalytic properties for oxygen evolution reaction. *Electrochim. Acta* **2005**, *50*, 2059-2064.

(39) Lee, S. W.; Carlton, C.; Risch, M.; Surendranath, Y.; Chen, S.; Furutsuki, S.; Yamada, A.; Nocera, D. G.; Shao-Horn, Y. The Nature of Lithium Battery Materials under Oxygen Evolution Reaction Conditions. *J. Am. Chem. Soc.* **2012**, *134*, 16959-16962.

(40) Grimaud, A.; May, K. J.; Carlton, C. E.; Lee, Y.-L.; Risch, M.; Hong, W. T.; Zhou, J.; Shao-Horn, Y. Double perovskites as a family of highly active catalysts for oxygen evolution in alkaline solution. *Nat. Commun.* **2013**, *4*.

(41) Frydendal, R.; Paoli, E. A.; Knudsen, B. P.; Wickman, B.; Malacrida, P.; Stephens, I. E. L.; Chorkendorff, I. Benchmarking the Stability of Oxygen Evolution Reaction Catalysts: The Importance of Monitoring Mass Losses. *ChemElectroChem* **2014**, *1*, 2075-2081.

(42) Singh, R. N.; Mishra, D.; Anindita; Sinha, A. S. K.; Singh, A. Novel electrocatalysts for generating oxygen from alkaline water electrolysis. *Electrochem. Commun.* **2007**, *9*, 1369-1373.

(43) Matsumoto, Y.; Kurimoto, J.; Sato, E. Oxygen evolution on $SrFeO_3$ electrode. *J. Electroanal. Chem.* **1979**, *102*, 77-83.

(44) Matsumoto, Y.; Manabe, H.; Sato, E. Oxygen Evolution on $La_{1-x}Sr_xCoO_3$ Electrodes in Alkaline Solutions. *J. Electrochem. Soc.* **1980**, *127*, 811-814.

(45) Wattiaux, A.; Grenier, J. C.; Pouchard, M.; Hagenmuller, P. Electrolytic Oxygen Evolution in Alkaline Medium on $La_{1-x}Sr_xFeO_{3-y}$ Perovskite-Related Ferrites: I . Electrochemical Study. *J. Electrochem. Soc.* **1987**, *134*, 1714-1718.

(46) Kim, T. W.; Woo, M. A.; Regis, M.; Choi, K.-S. Electrochemical Synthesis of Spinel Type $ZnCo_2O_4$ Electrodes for Use as Oxygen Evolution Reaction Catalysts. *J. Phys. Chem. Lett.* **2014**, *5*, 2370-2374.

(47) Maiyalagan, T.; Jarvis, K. A.; Therese, S.; Ferreira, P. J.; Manthiram, A. Spinel-type lithium cobalt oxide as a bifunctional electrocatalyst for the oxygen evolution and oxygen reduction reactions. **2014**, *5*.

(48) Chen, C.-F.; King, G.; Dickerson, R. M.; Papin, P. A.; Gupta, S.; Kellogg, W. R.; Wu, G. Oxygen-deficient $BaTiO_{3-x}$ perovskite as an efficient bifunctional oxygen electrocatalyst. *Nano Energy* **2015**, *13*, 423-432.

(49) Cheng, X.; Fabbri, E.; Nachtegaal, M.; Castelli, I. E.; El Kazzi, M.; Haumont, R.; Marzari, N.; Schmidt, T. J. Oxygen Evolution Reaction on $La_{1-x}Sr_xCoO_3$ Perovskites: A Combined Experimental and Theoretical Study of Their Structural, Electronic, and Electrochemical Properties. *Chem. Mater.* **2015**.

(50) Hu, H.; Guan, B.; Xia, B.; Lou, X. W. Designed Formation of Co_3O_4/$NiCo_2O_4$ Double-Shelled Nanocages with Enhanced Pseudocapacitive and Electrocatalytic Properties. *J. Am. Chem. Soc.* **2015**, *137*, 5590-5595.

(51) Wang, H.; Lee, H.-W.; Deng, Y.; Lu, Z.; Hsu, P.-C.; Liu, Y.; Lin, D.; Cui, Y. Bifunctional non-noble metal oxide nanoparticle electrocatalysts through lithium-induced conversion for overall water splitting. *Nat. Commun.* **2015**, *6*.

(52) Li, B.-Q.; Tang, C.; Wang, H.-F.; Zhu, X.-L.; Zhang, Q. An aqueous preoxidation method for monolithic perovskite electrocatalysts with enhanced water oxidation performance. *Sci. Adv.* **2016**, *2*.

(53) Kim, J.; Chen, X.; Pan, Y.-T.; Shih, P.-C.; Yang, H. W-Doped $CaMnO_{2.5}$ and $CaMnO_3$ Electrocatalysts for Enhanced Performance in Oxygen Evolution and Reduction Reactions. *J. Electrochem. Soc.* **2017**, *164*, F1074-F1080.

(54) Song, F.; Hu, X. Exfoliation of layered double hydroxides for enhanced oxygen evolution catalysis. *Nat. Commun.* **2014**, *5*.

(55) Song, F.; Hu, X. Ultrathin Cobalt–Manganese Layered Double Hydroxide Is an Efficient Oxygen Evolution Catalyst. *J. Am. Chem. Soc.* **2014**, *136*, 16481-16484.

(56) Oh, S. H.; Black, R.; Pomerantseva, E.; Lee, J.-H.; Nazar, L. F. Synthesis of a metallic mesoporous pyrochlore as a catalyst for lithium–O2 batteries. *Nat. Chem.* **2012**, *4*, 1004-1010.

(57) Oh, S. H.; Nazar, L. F. Oxide Catalysts for Rechargeable High-Capacity Li–O2 Batteries. **2012**, *2*, 903-910.

(58) McCrory, C. C. L.; Jung, S.; Peters, J. C.; Jaramillo, T. F. Benchmarking Heterogeneous Electrocatalysts for the Oxygen Evolution Reaction. *J. Am. Chem. Soc.* **2013**, *135*, 16977-16987.

(59) Parrondo, J.; George, M.; Capuano, C.; Ayers, K. E.; Ramani, V. Pyrochlore electrocatalysts for efficient alkaline water electrolysis. *J. Mater. Chem. A* **2015**, *3*, 10819-10828.

(60) Sardar, K.; Ball, S. C.; Sharman, J. D. B.; Thompsett, D.; Fisher, J. M.; Smith, R. A. P.; Biswas, P. K.; Lees, M. R.; Kashtiban, R. J.; Sloan, J.; Walton, R. I. Bismuth Iridium Oxide Oxygen Evolution Catalyst from Hydrothermal Synthesis. *Chem. Mater.* **2012**, *24*, 4192-4200.

(61) Sun, W.; Liu, J.-Y.; Gong, X.-Q.; Zaman, W.-Q.; Cao, L.-M.; Yang, J. OER activity manipulated by IrO_6 coordination geometry: an insight from pyrochlore iridates. *Sci. Rep.* **2016**, *6*, 38429.

(62) Sardar, K.; Petrucco, E.; Hiley, C. I.; Sharman, J. D. B.; Wells, P. P.; Russell, A. E.; Kashtiban, R. J.; Sloan, J.; Walton, R. I. Water-Splitting Electrocatalysis in Acid Conditions Using Ruthenate-Iridate Pyrochlores. *Angew. Chem. Int Ed.* **2014**, *53*, 10960-10964.

(63) Diaz-Morales, O.; Raaijman, S.; Kortlever, R.; Kooyman, P. J.; Wezendonk, T.; Gascon, J.; Fu, W. T.; Koper, M. T. M. Iridium-based double perovskites for efficient water oxidation in acid media. **2016**, *7*, 12363.

(64) Grimaud, A.; Demortiere, A.; Saubanere, M.; Dachraoui, W.; Duchamp, M.; Doublet, M.-L.; Tarascon, J.-M. Activation of surface oxygen sites on an iridium-based model catalyst for the oxygen evolution reaction. **2016**, *2*, 16189.

(65) Shih, P.-C.; Kim, J.; Sun, C.-J.; Yang, H. Single-Phase Pyrochlore $Y_2Ir_2O_7$ Electrocatalyst on the Activity of Oxygen Evolution Reaction. *ACS Appl. Energy Mater.* **2018**, *1*, 3992-3998.

(66) Seitz, L. C.; Dickens, C. F.; Nishio, K.; Hikita, Y.; Montoya, J.; Doyle, A.; Kirk, C.; Vojvodic, A.; Hwang, H. Y.; Norskov, J. K.; Jaramillo, T. F. A highly active and stable $IrO_x/SrIrO_3$ catalyst for the oxygen evolution reaction. *Science* **2016**, *353*, 1011-1014.

(67) Lebedev, D.; Povia, M.; Waltar, K.; Abdala, P. M.; Castelli, I. E.; Fabbri, E.; Blanco, M. V.; Fedorov, A.; Copéret, C.; Marzari, N.; Schmidt, T. J. Highly Active and Stable Iridium Pyrochlores for Oxygen Evolution Reaction. *Chem. Mater.* **2017**.

(68) Yang, L.; Yu, G.; Ai, X.; Yan, W.; Duan, H.; Chen, W.; Li, X.; Wang, T.; Zhang, C.; Huang, X.; Chen, J.-S.; Zou, X. Efficient oxygen evolution electrocatalysis in acid by a perovskite with face-sharing IrO_6 octahedral dimers. *Nat. Commun.* **2018**, *9*, 5236.

(69) McCrory, C. C. L.; Jung, S.; Ferrer, I. M.; Chatman, S. M.; Peters, J. C.; Jaramillo, T. F. Benchmarking Hydrogen Evolving Reaction and Oxygen Evolving Reaction Electrocatalysts for Solar Water Splitting Devices. *J. Am. Chem. Soc.* **2015**, *137*, 4347-4357.

(70) Lee, Y.; Suntivich, J.; May, K. J.; Perry, E. E.; Shao-Horn, Y. Synthesis and Activities of Rutile IrO_2 and RuO_2 Nanoparticles for Oxygen Evolution in Acid and Alkaline Solutions. *J. Phys. Chem. Lett.* **2012**, *3*, 399-404.

(71) Nong, H. N.; Oh, H.-S.; Reier, T.; Willinger, E.; Willinger, M.-G.; Petkov, V.; Teschner, D.; Strasser, P. Oxide-Supported $IrNiO_x$ Core–Shell Particles as Efficient, Cost-Effective, and Stable Catalysts for Electrochemical Water Splitting. *Angew. Chem. Int Ed.* **2015**, *54*, 2975-2979.

(72) Miara, L. J.; Richards, W. D.; Wang, Y. E.; Ceder, G. First-Principles Studies on Cation Dopants and Electrolyte|Cathode Interphases for Lithium Garnets. *Chem. Mater.* **2015**.

(73) Vojvodic, A.; Nørskov, J. K. Optimizing Perovskites for the Water-Splitting Reaction. *Science* **2011**, *334*, 1355-1356.

(74) García-Mota, M.; Bajdich, M.; Viswanathan, V.; Vojvodic, A.; Bell, A. T.; Nørskov, J. K. Importance of Correlation in Determining Electrocatalytic Oxygen Evolution Activity on Cobalt Oxides. **2012**, *116*, 21077-21082.

(75) Friebel, D.; Louie, M. W.; Bajdich, M.; Sanwald, K. E.; Cai, Y.; Wise, A. M.; Cheng, M.-J.; Sokaras, D.; Weng, T.-C.; Alonso-Mori, R.; Davis, R. C.; Bargar, J. R.; Nørskov, J. K.; Nilsson, A.; Bell, A. T. Identification of Highly Active Fe Sites in (Ni,Fe)OOH for Electrocatalytic Water Splitting. *J. Am. Chem. Soc.* **2015**, *137*, 1305-1313.

(76) Oh, H.-S.; Nong, H. N.; Reier, T.; Bergmann, A.; Gliech, M.; Ferreira de Araújo, J.; Willinger, E.; Schlögl, R.; Teschner, D.; Strasser, P. Electrochemical Catalyst–Support Effects and Their Stabilizing Role for IrO_x Nanoparticle Catalysts during the Oxygen Evolution Reaction. *J. Am. Chem. Soc.* **2016**.

(77) Spöri, C.; Kwan, J. T. H.; Bonakdarpour, A.; Wilkinson, D. P.; Strasser, P. The Stability Challenges of Oxygen Evolving Catalysts: Towards a Common Fundamental Understanding and Mitigation of Catalyst Degradation. *Angew. Chem. Int Ed.* **2017**, *56*, 5994-6021.

(78) Fabbri, E.; Schmidt, T. J. Oxygen Evolution Reaction—The Enigma in Water Electrolysis. *ACS Catalysis* **2018**, *8*, 9765-9774.

(79) Benck, J. D.; Hellstern, T. R.; Kibsgaard, J.; Chakthranont, P.; Jaramillo, T. F. Catalyzing the Hydrogen Evolution Reaction (HER) with Molybdenum Sulfide Nanomaterials. *ACS Catalysis* **2014**, *4*, 3957-3971.

(80) Zhang, J.; Zhao, Y.; Zhao, X.; Liu, Z.; Chen, W. Porous Perovskite $LaNiO_3$ Nanocubes as Cathode Catalysts for Li-O_2 Batteries with Low Charge Potential. *Sci. Rep.* **2014**, *4*, 6005.

(81) Yu, N.; Kuai, L.; Wang, Q.; Geng, B. Pt nanoparticles residing in the pores of porous $LaNiO_3$ nanocubes as high-efficiency electrocatalyst for direct methanol fuel cells. *Nanoscale* **2012**, *4*, 5386-5393.

(82) Zhang, W.; Ma, Z.; Du, L.; Li, H. Role of PEG4000 in sol-gel synthesis of $Sm_2Ti_2O_7$ photocatalyst for enhanced activity. *J. Alloy. Compd.* **2017**, *704*, 26-31.

(83) Wang, S.; Li, W.; Wang, S.; Jiang, J.; Chen, Z. Synthesis of well-defined hierarchical porous $La_2Zr_2O_7$ monoliths via non-alkoxide sol–gel process accompanied by phase separation. *Microporous Mesoporous Mater.* **2016**, *221*, 32-39.

(84) Taguchi, H. Electrical properties of $CaMnO_{3-\delta}$. *Phys. Status Solidi A* **1985**, *88*, K79-K82.

(85) Alfaruq, D. S.; Eilertsen, J.; Thiel, P.; Aguirre, M. H.; Otal, E.; Populoh, S.; Yoon, S.; Weidenkaff, A. High-temperature thermoelectric properties of W-substituted $CaMnO_3$. *MRS Proceedings* **2013**, *1490*, 3-8.

(86) Kruth, A.; R. West, A. Electrical properties of the oxygen-deficient perovskites, $Ca_2Mn_{2-x}Nb_xO_\gamma$: $0 \leq x \leq 1.2$, with Mn valence varying from +2.0 to +4.0. *J. Mater. Chem.* **2001**, *11*, 153-159.

(87) Yin, H.; Tang, Z. Ultrathin two-dimensional layered metal hydroxides: an emerging platform for advanced catalysis, energy conversion and storage. *Chem. Soc. Rev.* **2016**, *45*, 4873-4891.

(88) Zhang, B.; Zheng, X.; Voznyy, O.; Comin, R.; Bajdich, M.; García-Melchor, M.; Han, L.; Xu, J.; Liu, M.; Zheng, L.; García de Arquer, F. P.; Dinh, C. T.; Fan, F.; Yuan, M.; Yassitepe, E.; Chen, N.; Regier, T.; Liu, P.; Li, Y.; De Luna, P.; Janmohamed, A.; Xin, H. L.; Yang, H.; Vojvodic, A.; Sargent, E. H. Homogeneously dispersed multimetal oxygen-evolving catalysts. *Science* **2016**, *352*, 333-337.

(89) Okamura, M.; Kondo, M.; Kuga, R.; Kurashige, Y.; Yanai, T.; Hayami, S.; Praneeth, V. K. K.; Yoshida, M.; Yoneda, K.; Kawata, S.; Masaoka, S. A pentanuclear iron catalyst designed for water oxidation. *Nature* **2016**, *530*, 465.

(90) Han, Z.; Qiu, F.; Eisenberg, R.; Holland, P. L.; Krauss, T. D. Robust Photogeneration of H_2 in Water Using Semiconductor Nanocrystals and a Nickel Catalyst. *Science* **2012**, *338*, 1321-1324.

(91) Park, S.; Shao, Y.; Liu, J.; Wang, Y. Oxygen electrocatalysts for water electrolyzers and reversible fuel cells: status and perspective. *Energy Environ. Sci.* **2012**, *5*, 9331-9344.

(92) Hocking, R. K.; Brimblecombe, R.; Chang, L.-Y.; Singh, A.; Cheah, M. H.; Glover, C.; Casey, W. H.; Spiccia, L. Water-oxidation catalysis by manganese in a geochemical-like cycle. *Nat. Chem.* **2011**, *3*, 461.

(93) Walter, M. G.; Warren, E. L.; McKone, J. R.; Boettcher, S. W.; Mi, Q.; Santori, E. A.; Lewis, N. S. Solar Water Splitting Cells. *Chem. Rev.* **2010**, *110*, 6446-6473.

(94) Xia, B. Y.; Yan, Y.; Li, N.; Wu, H. B.; Lou, X. W.; Wang, X. A metal–organic framework-derived bifunctional oxygen electrocatalyst. *Nat. Energy* **2016**, *1*, 15006.

(95) Gao, M.-R.; Xu, Y.-F.; Jiang, J.; Zheng, Y.-R.; Yu, S.-H. Water Oxidation Electrocatalyzed by an Efficient Mn_3O_4/$CoSe_2$ Nanocomposite. *J. Am. Chem. Soc.* **2012**, *134*, 2930-2933.

(96) Zhao, S.; Wang, Y.; Dong, J.; He, C.-T.; Yin, H.; An, P.; Zhao, K.; Zhang, X.; Gao, C.; Zhang, L.; Lv, J.; Wang, J.; Zhang, J.; Khattak, A. M.; Khan, N. A.; Wei, Z.; Zhang, J.; Liu, S.; Zhao, H.; Tang, Z. Ultrathin metal–organic framework nanosheets for electrocatalytic oxygen evolution. *Nat. Energy* **2016**, *1*, 16184.

(97) Zhang, J.; Zhao, Z.; Xia, Z.; Dai, L. A metal-free bifunctional electrocatalyst for oxygen reduction and oxygen evolution reactions. *Nat. Nanotechnol.* **2015**, *10*, 444.

(98) Frydendal, R.; Paoli, E. A.; Chorkendorff, I.; Rossmeisl, J.; Stephens, I. E. L. Toward an Active and Stable Catalyst for Oxygen Evolution in Acidic Media: Ti-Stabilized MnO2. *Adv. Energy Mater.* **2015**, *5*, 1500991.

(99) Park, J.; Park, M.; Nam, G.; Kim, M. G.; Cho, J. Unveiling the Catalytic Origin of Nanocrystalline Yttrium Ruthenate Pyrochlore as a Bifunctional Electrocatalyst for Zn–Air Batteries. *Nano Lett.* **2017**, *17*, 3974-3981.

(100) Bevilacqua, M.; Bianchini, C.; Marchionni, A.; Filippi, J.; Lavacchi, A.; Miller, H.; Oberhauser, W.; Vizza, F.; Granozzi, G.; Artiglia, L.; Annen, S. P.; Krumeich, F.; Grützmacher, H. Improvement in the efficiency of an OrganoMetallic Fuel Cell by tuning the molecular architecture of the anode electrocatalyst and the nature of the carbon support. *Energy Environ. Sci.* **2012**, *5*, 8608-8620.

(101) Hu, Y.-Y.; Liu, Z.; Nam, K.-W.; Borkiewicz, O. J.; Cheng, J.; Hua, X.; Dunstan, M. T.; Yu, X.; Wiaderek, K. M.; Du, L.-S.; Chapman, K. W.; Chupas, P. J.; Yang, X.-Q.; Grey, C. P. Origin of additional capacities in metal oxide lithium-ion battery electrodes. *Nat. Mater.* **2013**, *12*, 1130.

(102) Moulder, J. F.; Chastain, J. *Handbook of X-ray Photoelectron Spectroscopy: A Reference Book of Standard Spectra for Identification and Interpretation of XPS Data*; Physical Electronics Division, Perkin-Elmer Corporation, 1992.

(103) Danks, A. E.; Hall, S. R.; Schnepp, Z. The evolution of 'sol–gel' chemistry as a technique for materials synthesis. *Mater. Horiz.* **2016**, *3*, 91-112.

(104) Subramanian, M. A.; Aravamudan, G.; Subba Rao, G. V. Oxide pyrochlores — A review. *Prog. Solid State Chem.* **1983**, *15*, 55-143.

(105) Meier, J. C.; Galeano, C.; Katsounaros, I.; Topalov, A. A.; Kostka, A.; Schüth, F.; Mayrhofer, K. J. J. Degradation Mechanisms of Pt/C Fuel Cell Catalysts under Simulated Start–Stop Conditions. *ACS Catalysis* **2012**, *2*, 832-843.

(106) Ng, J. W. D.; García-Melchor, M.; Bajdich, M.; Chakthranont, P.; Kirk, C.; Vojvodic, A.; Jaramillo, T. F. Gold-supported cerium-doped NiO_x catalysts for water oxidation. *Nat. Energy* **2016**, *1*, 16053.

(107) Audichon, T.; Napporn, T. W.; Canaff, C.; Morais, C.; Comminges, C.; Kokoh, K. B. IrO_2 Coated on RuO_2 as Efficient and Stable Electroactive Nanocatalysts for Electrochemical Water Splitting. *J. Phys. Chem. C* **2016**, *120*, 2562-2573.

(108) Hu, C.-C.; Chang, K.-H.; Lin, M.-C.; Wu, Y.-T. Design and Tailoring of the Nanotubular Arrayed Architecture of Hydrous RuO_2 for Next Generation Supercapacitors. *Nano Lett.* **2006**, *6*, 2690-2695.

(109) Cava, R. J. Schizophrenic electrons in ruthenium-based oxides. *Dalton Trans.* **2004**, 2979-2987.

(110) Chen, T.-Y.; Lee, G.-W.; Liu, Y.-T.; Liao, Y.-F.; Huang, C.-C.; Lin, D.-S.; Lin, T.-L. Heterojunction confinement on the atomic structure evolution of near monolayer core–

shell nanocatalysts in redox reactions of a direct methanol fuel cell. *J. Mater. Chem. A* **2015**, *3*, 1518-1529.

(111) Riegg, S.; Reller, A.; Loidl, A.; Ebbinghaus, S. G. Valence properties of Cu and Ru in titanium-substituted $LnCu_3Ru_4O_{12+\delta}$ (Ln = La, Pr, Nd) investigated by XANES and TGA. *Dalton Trans.* **2015**, *44*, 10852-10859.

(112) Danilovic, N.; Subbaraman, R.; Chang, K. C.; Chang, S. H.; Kang, Y.; Snyder, J.; Paulikas, A. P.; Strmcnik, D.; Kim, Y. T.; Myers, D.; Stamenkovic, V. R.; Markovic, N. M. Using Surface Segregation To Design Stable Ru-Ir Oxides for the Oxygen Evolution Reaction in Acidic Environments. *Angew. Chem. Int Ed.* **2014**, *53*, 14016-14021.

(113) Cox, P. A.; Egdell, R. G.; Goodenough, J. B.; Hamnett, A.; Naish, C. C. The metal-to-semiconductor transition in ternary ruthenium (IV) oxides: a study by electron spectroscopy. *J. Phys. C: Solid State Phys.* **1983**, *16*, 6221.

(114) Schmidt, M.; Cummins, T. R.; Bürk, M.; Lu, D. H.; Nücker, N.; Schuppler, S.; Lichtenberg, F. Nature of the electronic states in the layered perovskite noncuprate superconductor Sr_2RuO_4. *Phys. Rev. B* **1996**, *53*, R14761-R14764.

(115) Näslund, L.-Å.; Sánchez-Sánchez, C. M.; Ingason, Á. S.; Bäckström, J.; Herrero, E.; Rosen, J.; Holmin, S. The Role of TiO_2 Doping on RuO_2-Coated Electrodes for the Water Oxidation Reaction. *J. Phys. Chem. C* **2013**, *117*, 6126-6135.

(116) Hüfner, S. *Photoelectron Spectroscopy: Principles and Applications, 3rd ed.*; Springer-Verlag: Berlin, 2010.

(117) Stranick, M. A.; Moskwa, A. SnO_2 by XPS. *Surf. Sci. Spectra* **1993**, *2*, 50-54.

(118) Halcrow, M. A. Jahn–Teller distortions in transition metal compounds, and their importance in functional molecular and inorganic materials. *Chem. Soc. Rev.* **2013**, *42*, 1784-1795.

(119) Jain, A.; Shin, Y.; Persson, K. A. Computational predictions of energy materials using density functional theory. *Nat. Rev. Mater.* **2016**, *1*, 15004.

(120) Grimaud, A.; Diaz-Morales, O.; Han, B.; Hong, W. T.; Lee, Y.-L.; Giordano, L.; Stoerzinger, K. A.; Koper, M. T. M.; Shao-Horn, Y. Activating lattice oxygen redox reactions in metal oxides to catalyse oxygen evolution. *Nat. Chem.* **2017**, *9*, 457.

(121) Nguyen, M. H.; Lee, S.-J.; Kriven, W. M. Synthesis of oxide powders by way of a polymeric steric entrapment precursor route. *J. Mater. Res.* **2011**, *14*, 3417-3426.

(122) Ribero, D.; Kriven, W. M. Synthesis of $LiFePO_4$ powder by the organic–inorganic steric entrapment method. *J. Mater. Res.* **2015**, *30*, 2133-2143.

(123) Sanchez Casalongue, H. G.; Ng, M. L.; Kaya, S.; Friebel, D.; Ogasawara, H.; Nilsson, A. In Situ Observation of Surface Species on Iridium Oxide Nanoparticles during the Oxygen Evolution Reaction. *Angew. Chem.* **2014**, *126*, 7297-7300.

(124) Kahk, J. M.; Poll, C. G.; Oropeza, F. E.; Ablett, J. M.; Céolin, D.; Rueff, J. P.; Agrestini, S.; Utsumi, Y.; Tsuei, K. D.; Liao, Y. F.; Borgatti, F.; Panaccione, G.; Regoutz, A.; Egdell, R. G.; Morgan, B. J.; Scanlon, D. O.; Payne, D. J. Understanding the Electronic Structure of IrO_2 Using Hard-X-ray Photoelectron Spectroscopy and Density-Functional Theory. *Phys. Rev. Lett.* **2014**, *112*, 117601.

(125) Clancy, J. P.; Chen, N.; Kim, C. Y.; Chen, W. F.; Plumb, K. W.; Jeon, B. C.; Noh, T. W.; Kim, Y.-J. Spin-orbit coupling in iridium-based 5dcompounds probed by x-ray absorption spectroscopy. *Phys. Rev. B* **2012**, *86*.

(126) Laguna-Marco, M. A.; Haskel, D.; Souza-Neto, N.; Lang, J. C.; Krishnamurthy, V. V.; Chikara, S.; Cao, G.; van Veenendaal, M. Orbital magnetism and spin-orbit effects in the electronic structure of $BaIrO_3$. *Phys. Rev. Lett.* **2010**, *105*, 216407.

(127) Choy, J.-H.; Kim, D.-K.; Hwang, S.-H.; Demazeau, G.; Jung, D.-Y. XANES and EXAFS Studies on the Ir-O Bond Covalency in Ionic Iridium Perovskites. *J. Am. Chem. Soc.* **1995**, *117*, 8557-8566.

(128) Koo, H. J.; Whangbo, M. H.; Kennedy, B. J. Similarities and Differences in the Structural and Electronic Properties of Ruthenium and Iridium Pyrochlores $A_2M_2O_{7-y}$ (M=Ru, Ir). *J. Solid State Chem.* **1998**, *136*, 269-273.

APPENDIX A

Optimization of the Electrode Preparation for Oxygen Evolution Reaction Catalysts

In this appendix, the optimization of oxygen evolution reaction (OER) testing conditions are presented. We address features related to electrode preparation as well as measurement conditions and procedures. These optimizations are critical for both obtaining accurate, reproducible values and achieving the highest catalytic activity for the OER.

Under the conditions studied, we conclude that the following provides a standard protocol for the electrode preparation: a 1:1 catalyst-to-carbon ratio at a catalyst loading of 5 μg; and tetrahydrofuran (THF) as solvent for ink preparation. Due to carbon corrosion, minimum carbon loading is desired, as shown its impact on OER activity. However, lower catalyst loadings result in higher specific OER activity (normalized by catalyst surface area). THF as solvent for ink preparation gives slightly higher OER activity in addition to other advantages such as slower sedimentation of ink and faster solvent evaporation compare to other solvents that have been tested. Substrate properties have different effects on the activity of the $Y_2Ru_2O_{7-\delta}$ (YRO) and $Y_2Ir_2O_{7-\delta}$ (YIO) catalysts. Since YIO is more conductive than YRO, YIO showed minimal difference in OER activity in the absence of conducting carbon (no carbon support while using conducting glass current collector). In contrast, YRO shows a large deficit in OER activity when all carbon content is excluded. This result shows that depends on catalyst material properties, different electrode preparation may be used to obtain optimal OER activity.

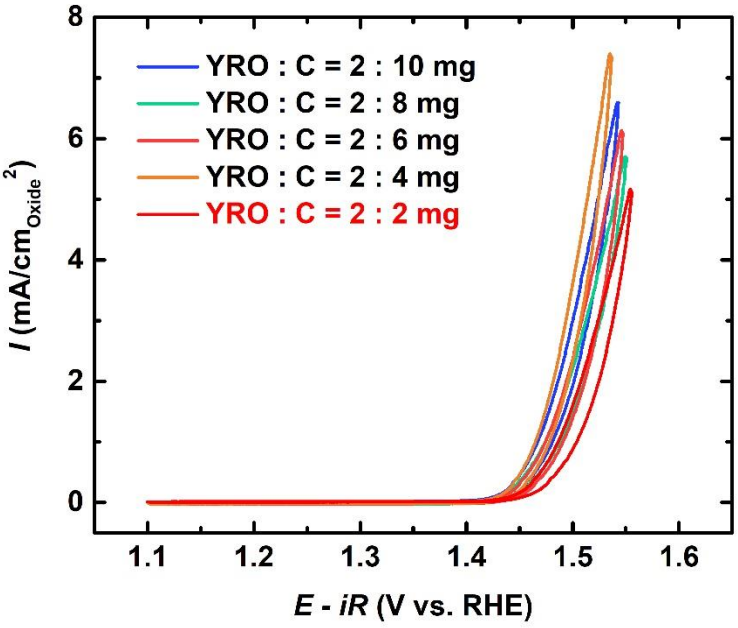

Figure A.1 CV curves of YRO catalyst prepared with different loadings of carbon (C, Vulcan XC-72). The amount of YRO loading was fixed at 2 mg. The OER activities were not scaled with addition of carbon.

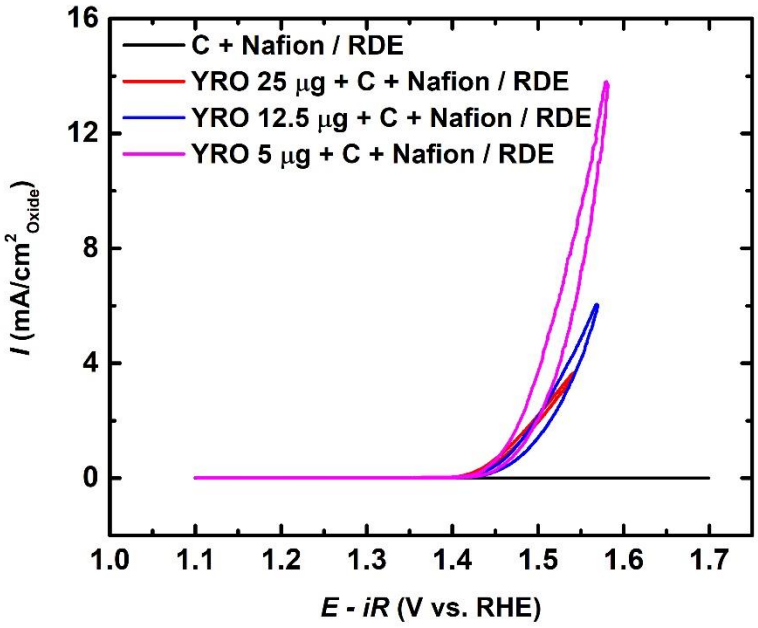

Figure A.2 CV curves with different YRO catalyst loadings, normalized by catalyst surface area. Low loading (5 μg) showed higher OER activity after normalization.

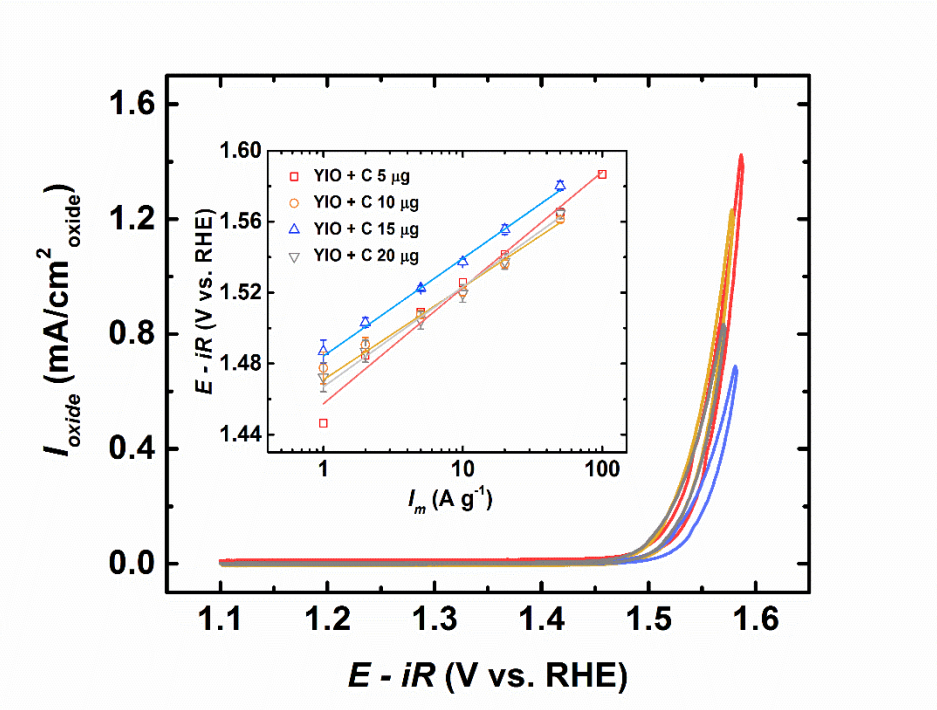

Figure A.3 CV curves for different YIO catalyst loadings. Inset shows the corresponding Tafel plot.

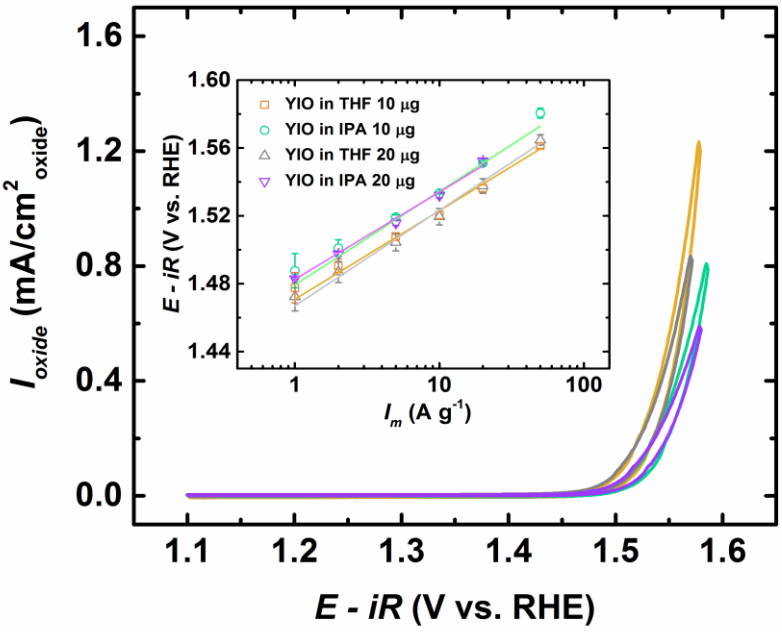

Figure A.4 CV curves of YIO catalysts with different solvents and loadings during ink preparation. Tetrahydrofuran (THF) was used without modification; isopropanol (IPA) was pre-mixed with de-ionized water (DIW, IPA:DIW = 4:1). Inset shows the corresponding Tafel plot.

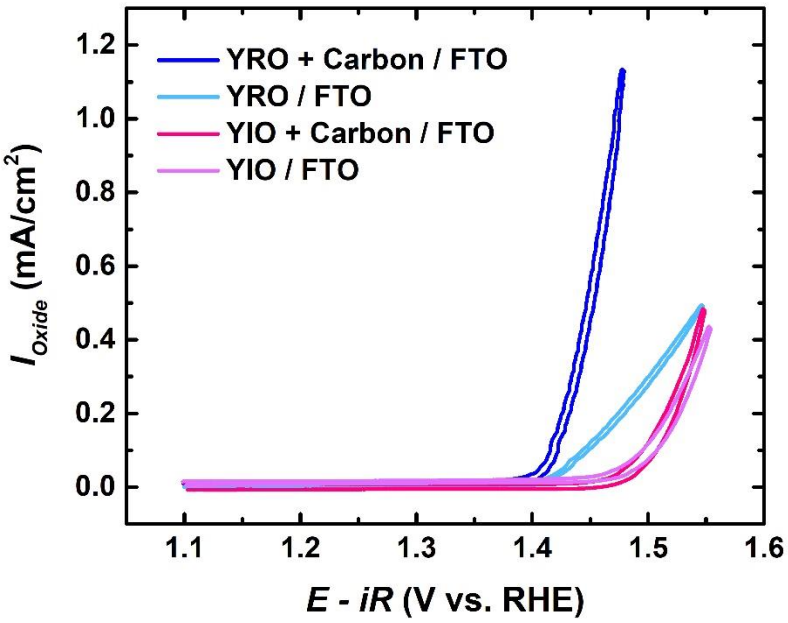

Figure A.5 CV curves of YRO and YIO catalysts with and without carbon as conducting supports on conducting glass current collector (FTO, fluorine-doped tin oxide). YRO showed large enhancement in OER activities with conductive carbon support while YIO showed minimum enhancement.

APPENDIX B

Preparation and Oxygen Evolution Reaction Activity of Other Types of $A_2Ru_2O_{7-\delta}$ (A = Bi and Tl) Pyrochlore Materials

Other types of Ru-based pyrochlore materials have been made, including $A_2Ru_2O_{7-\delta}$ (A = Bi, Tl and Pb). In this appendix, we show the characterization of these pyrochlore materials in addition to their comparison with $Y_2Ru_2O_{7-\delta}$ and RuO_2. The procedures for obtaining these materials is modified from the sol-gel synthesis described in Chapter 2. The precursors for the A-site were metal nitrates (bismuth nitrate pentahydrate, Thallium nitrate trihydrate and lead nitrate, Sigma-Aldrich). For each $A_2Ru_2O_{7-\delta}$, the precursor was added stoichiometrically in an aqueous solution containing ruthenium nitrosyl nitrate (Sigma-Aldrich). After drying, the samples were annealed: $Bi_2Ru_2O_{7-\delta}$ (900 ºC for 12 h), $Tl_2Ru_2O_{7-\delta}$ (500 ºC for 24 h), and $Pb_2Ru_2O_{7-\delta}$ (900 ºC for 12 h).

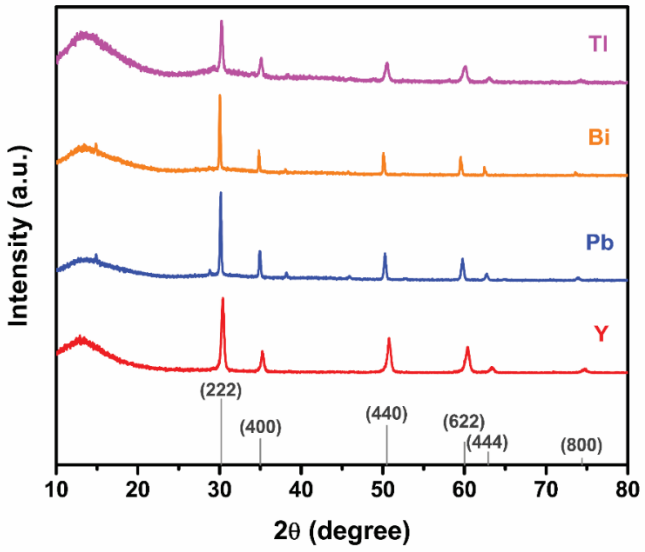

Figure B.1 XRD patterns of $A_2Ru_2O_{7-\delta}$ (A = Bi, Tl, Pb and Y). All materials are cubic phase pyrochlore (Fd-3m).

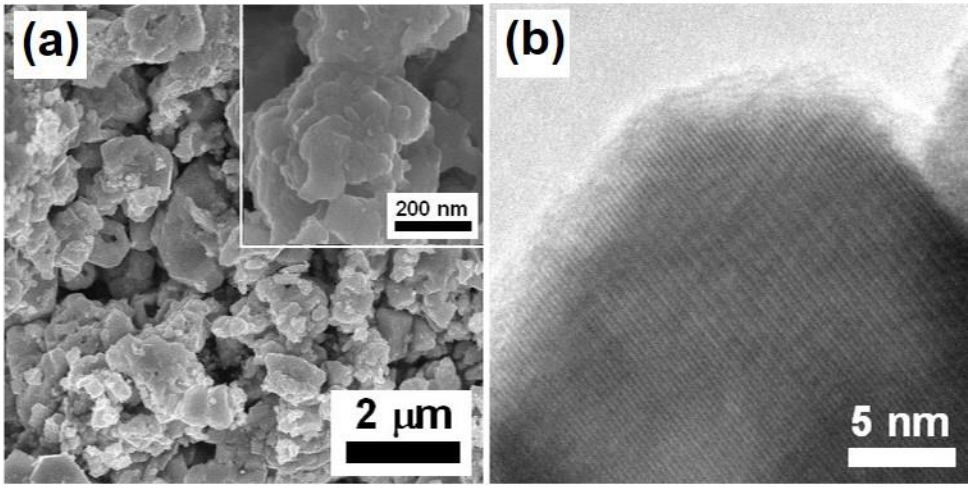

Figure B.2 (a) SEM and (b) TEM images of as-made $Tl_2Ru_2O_{7-\delta}$ pyrochlore.

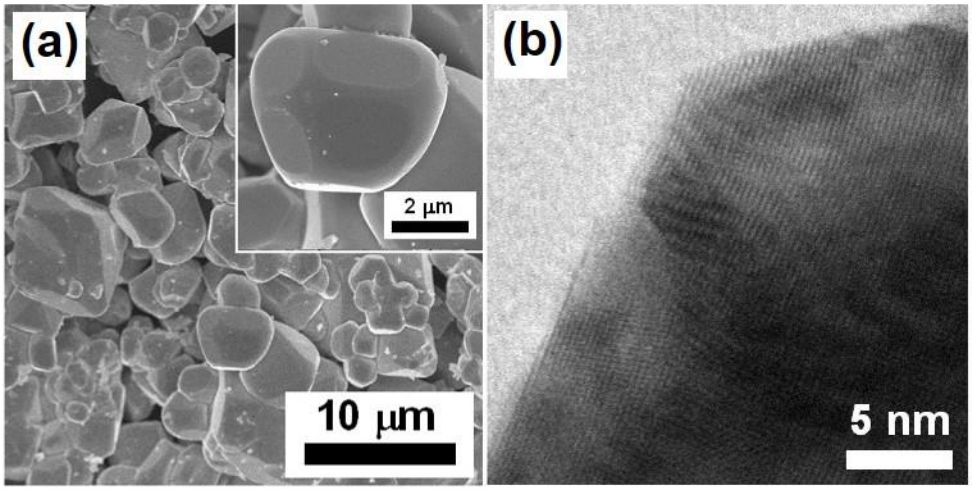

Figure B.3 (a) SEM and (b) TEM images of as-made $Bi_2Ru_2O_{7-\delta}$ pyrochlore.

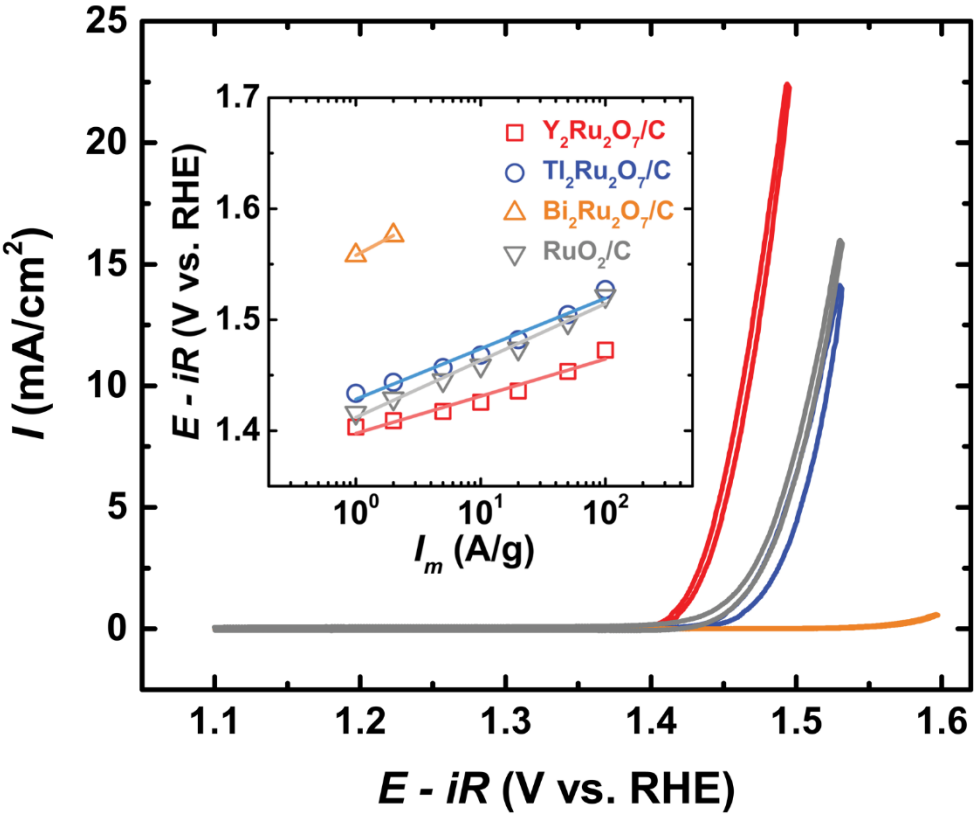

Figure B.4 CV curves of $A_2Ru_2O_{7-\delta}$ (A = Bi, Tl and Y) pyrochlores and commercial RuO_2 as reference. Inset shows the corresponding Tafel plot. Activity follows: $Y_2Ru_2O_{7-\delta}$ > RuO_2 > $Tl_2Ru_2O_{7-\delta}$ > $Bi_2Ru_2O_{7-\delta}$. The current densities are normalized to electrode surface area; catalyst particle size and surface area effects are not comprehended in this measurement.

APPENDIX C

Measurement and Data Analysis of X-ray Absorption Spectroscopy

All X-ray absorption spectroscopy (XAS) experiments were performed in transmission mode at Beamline 20-BM-B at the Advanced Photon Source (APS), Argonne National Laboratory, USA. Dry powder samples were mixed with minimum amount of boron nitride, pressed into pellets and sealed with Keton tape (see **Figure C.1**). X-ray absorption near-edge structure (XANES) analysis is performed with Athena program. Extended X-ray absorption fine structure (EXAFS) analysis is performed with Artemis program.

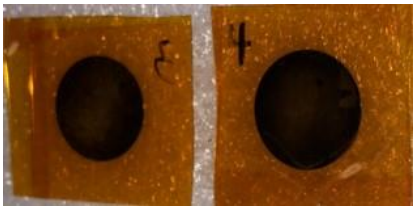

Figure C.1 $Y_2Ir_2O_{7-\delta}$ pellets sealed in Keton tape for XAS measurement.

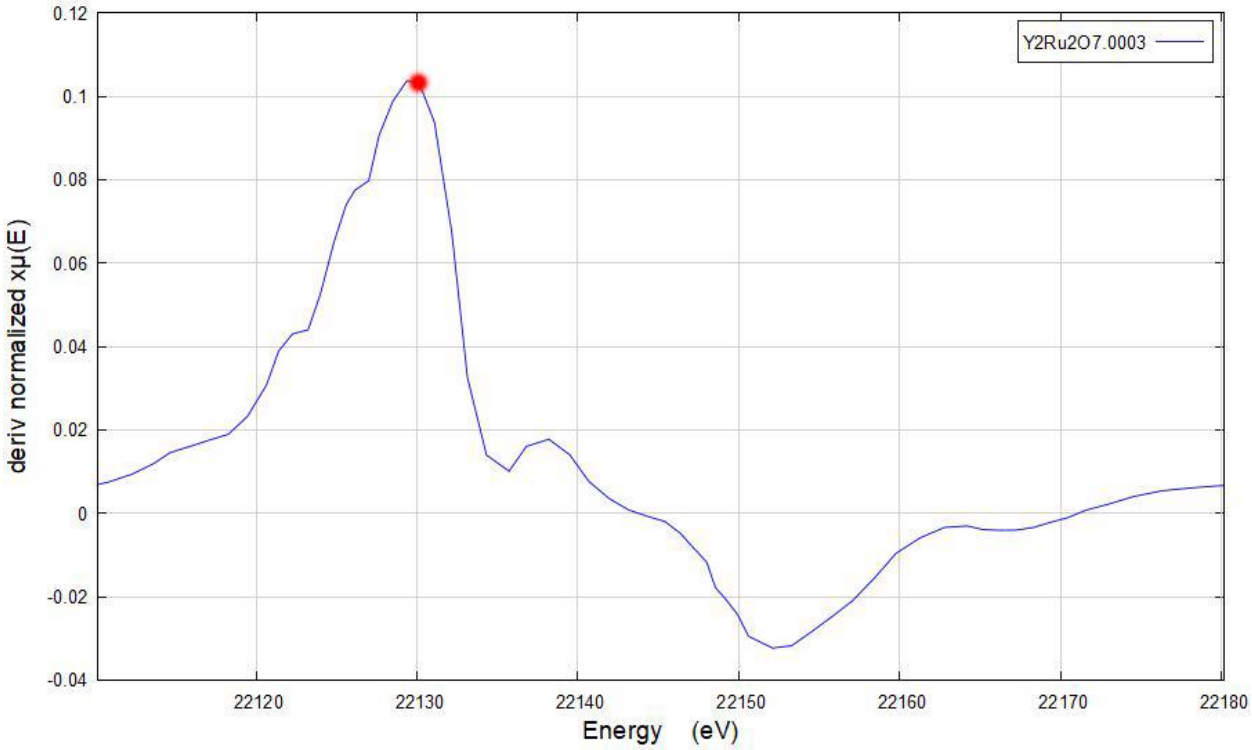

Figure C.2 The first-order derivative plot of the XAS data of Ru K-edge for the $Y_2Ru_2O_{7-\delta}$ catalyst. The absorption energy (E_0) is determined by the first maximum of the graph, marked by a red dot.

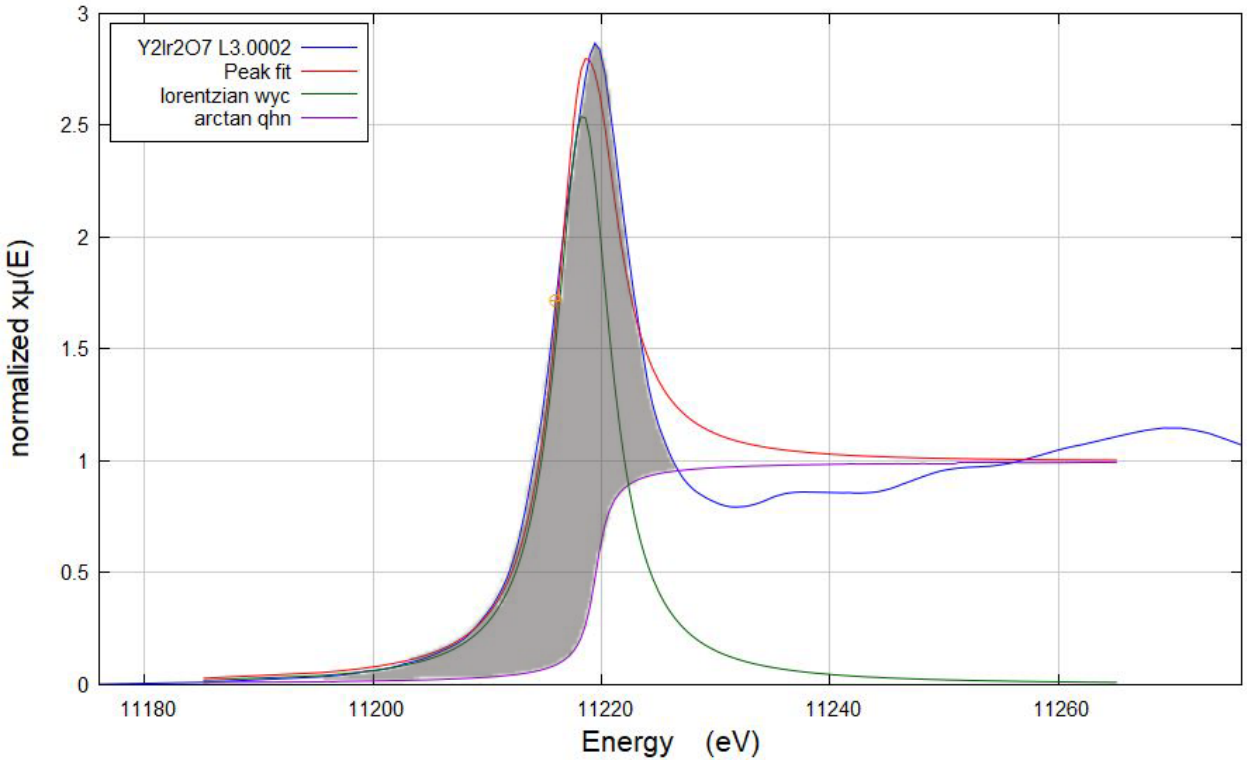

Figure C.3 XANES fitting of Ir L3-edge of $Y_2Ir_2O_{7-\delta}$. Blue, red, green and purple curves indicate the XANES data, fitting curve, Lorentzian function and arctangent step function, respectively. The grey shaded area indicates the white-line integrated intensity.

To study the oxidation state from XANES analysis, the absorption energy (E_0) of Ru K-edge and integrated white-line intensity of Ir L3-edge are examined. Additional materials for each of Ru and Ir were used as reference to correlate oxidation states. In the case of Ru, Ru foil and commercial RuO_2 powder were considered for Ru oxidation states of 0 and +4, respectively. For Ir, commercial $IrCl_3$ and IrO_2 powder were used and considered for Ir oxidation states of +3 and +4, respectively. After the correlation between E_0, integrated white-line intensities and oxidation states were set by reference materials, interpolation method was used to acquire the oxidation state of examined pyrochlore materials (**Figure 2.6b** and **Figure 3.11a**).

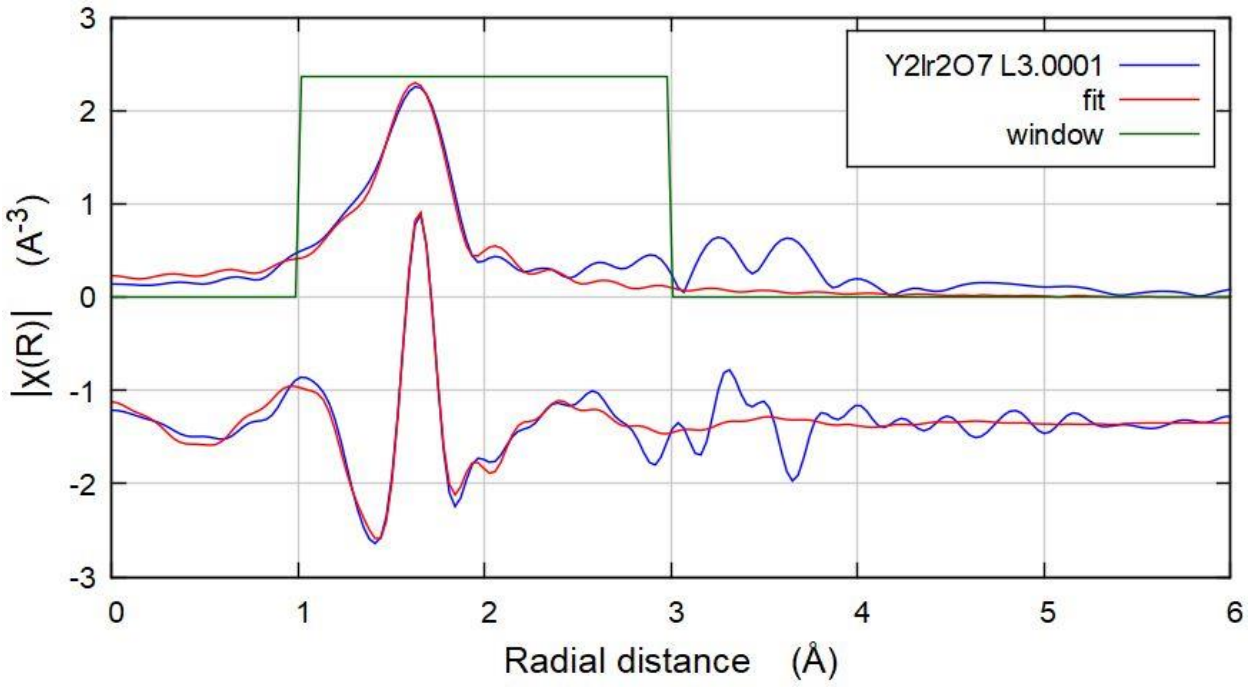

Figure C.4 Illustration of EXAFS analysis of $Y_2Ir_2O_{7-\delta}$. A first-shell Ir-O path was simulated and fit to experimental data in R-space range of 1-3 Å. Note: the Ir-O path was simulated from unit cell structure acquired from ICSD cystography database.

Table C.1 First-shell simulation results of $Y_2Ir_2O_{7-\delta}$.

Coordination	N	S_0^2	σ^2	E_0	ΔR	R_{eff}	R
Ir—O	6	0.802	0.00238	10.747	0.00722	1.98380	1.99102

EXAFS analysis and fitting were performed with Artemis program. Unit cell structures with the atoms information were acquired in ICSD database. After running the atom patch, a simple first-shell model was used. **Figure C.4** is an example of EXAFS fitting of the first-shell Ir-O and **Table C.1** summarizes the fitting parameters. The effective distance between Ir and neighboring O atoms is evaluated to be 1.98 Å.